UCGE Reports
Number 20298

Department of Geomatics Engineering

Optimal Smoothing Techniques in Aided Inertial Navigation and Surveying Systems

(URL: http://www.geomatics.ucalgary.ca/graduatetheses)

by

Hang (Terry) Liu

November 2009

UNIVERSITY OF CALGARY

Optimal Smoothing Techniques in Aided Inertial Navigation and Surveying Systems

by

Hang Liu

A THESIS

SUBMITTED TO THE FACULTY OF GRADUATE STUDIES

IN PARTIAL FULFILMENT OF THE REQUIREMENTS FOR THE

DEGREE OF MASTER OF SCIENCE

DEPARTMENT OF GEOMATICS ENGINEERING

CALGARY, ALBERTA

November 2009

Abstract

Tactical-grade, low-cost Inertial Navigation Systems (INSs) and Micro-Electro-Mechanical Systems (MEMS) inertial sensors have gained great interests in civilian and commercial fields during the last decade. The Global Positioning System (GPS) is recognized as the ideal complement to INS by offering absolute positioning information and consistent accuracy in open sky to overcome the problem of INS time-dependent error growth. However, GPS suffers from degraded signal acquisition or poor satellite geometry when a vehicle is traveling in urban, dense foliage or canyon areas. In addition, the GPS signals will be totally unavailable in the isolated environments such as tunnels, mines or indoor areas. Hence, alternative aiding instruments or techniques such as odometers, non-holonomic constraints, Zero-velocity Updates (ZUPTs) and Coordinate Updates (CUPTs) become essential to restrict the accumulated time-dependent errors of a stand-alone INS. While Kalman filter is widely employed as the real-time estimation method to fuse the multi-sensor information, optimal smoothing will be utilized as the post-processing methodology to provide better navigation solutions.

In this research, two different fixed-interval smoothing algorithms will be utilized and evaluated. The first algorithm is the Two Filter Smoother (TFS), while the second algorithm is the Rauch-Tung-Streibel Smoother (RTSS). The TFS is performed by combining the results of Forward Kalman Filtering (FKF) and Backward Kalman Filtering (BKF) through minimizing the smoother error covariance. The traditional TFS was not applicable for some INS-based multi-sensor systems because of the high

nonlinear characteristics in the INS navigation equations. Thus, the revised TFS algorithm will be derived in details. The performance of Kalman filtering as well as the optimal smoothing methodologies is evaluated in three application conditions: land-vehicle navigation, pipeline surveying, and horizontal/vertical indoor building navigation, surveying and mapping. The integration strategies of INS and the aiding techniques mentioned earlier are proved to be applicable and effective. The results of all investigated applications show that the TFS substantially improve the position estimation accuracy over the corresponding filtered solution. In addition, the estimation efficiency of the TFS is comparable to the commonly used RTSS.

Acknowledgements

First and foremost, I would like to express my sincere appreciation to my supervisor, Dr. Naser El-Sheimy. Thank you for providing me with the precious opportunity to pursue my master degree in Department of Geomatics Engineering. Your continuous guidance, encouragement, support and understanding helped me throughout my studying and research. Dr. Yang Gao, Dr. Aboelmagd Noureldin and Dr. Swavik Spiewak, members of my examination committee, are greatly acknowledged for your time and constructive comments to review and improve this thesis.

Dr. Sameh Nassar in the Mobile Multi-Sensor Systems (MMSS) Research Group is specially thanked for offering valuable comments and suggestions on my research, and proofreading my thesis; Dr. Xiaoji Niu is thanked for introducing me to this group; Yigiter Yuksel, Dr. Taher Hassan, Dr. Dongqing Gu, Dr. Yuanxin Wu, Xing (Bob) Zhao, Dr. Chris Goodall, and Dr. Yong Yang are thanked for your precious advice, help and encouragement on my courses, research and thesis; Dr. Eun-Hwan Shin is thanked for providing the MMSS Research Group software: Aided Inertial Navigation System (AINS™) Toolbox; members of ENGO 500 project on "GPS/INS Integration for indoor navigation applications", Ian Isackson, Ben Clipperton, Lucas Cairns and Pavlo Karbovnyk are thanked for providing the building surveying data.

I would like to give my thanks and gratefulness to the individuals with whom I am for more than two years:

- To my lovely wife, Linlin Duan. You mean everything to me.
- To my friends in Trailer-D, Ahmed El-Ghazouly, Yigiter Yuksel, Taher Hassan, Mohamed Youssef, Adel Moussa, Abdelrahman Ali, Feng Xu, Junbo Shi, Shuang Du, and Changsheng Cai. You are the reason I could ignore the malfunctioned air conditioner and keep working under the dark lamps.
- To my friends in this department, Xing Zhao, Zhan Zhang, Feng Tang, Wei Cao, Man Feng, Tao Lin, Wei Gu, Peng Xie, Da Wang, Tao Li and many others. You are the reason I could walk around the engineering building and practice my communication skills even if you thought I was not good at talking.
- To my sister Ning Liu, my brother-in-law Zhiyong Li, and my cute nephew Siyu Li, you are the reason I could enjoy regular family parties and remember the real flavor of Chinese food, in the western hemisphere.
- Finally, to my parents, you are the reason I am.

Table of Contents

List of Tables

List of Figures

List of Abbreviations and Nomenclature

Symbol	Definition
AGM	Above Ground Markers
AKF	Adaptive Kalman Filter
ARW	Angle Random Walk
BKF	Backward Kalman Filter
CUPT	Coordinate Update
DCM	Directional Cosine Matrix
DGPS	Differential GPS
DOD	Department of Defence
ECEF	Earth-Centered Earth-Fixed
EKF	Extended Kalman Filter
FKF	Forward Kalman Filter
FOG	Fiber Optical Gyros
GINS	Gimbaled Inertial Navigation Systems
GNSS	Global Navigation Satellite Systems
GPS	Global Positioning Systems
IMU	Inertial Navigation Units
INS	Inertial Navigation Systems
KF	Kalman Filter
MEMS	Micro-Electro-Mechanical Systems
NED	North-East-Down
ODOM	Odometers
OSA	One Sample After
OSB	One Sample Before
PDF	Probability Density Function
PIG	Pipeline Inspection Gauges
RLG	Ring Laser Gyros
RTSS	Rauch-Tung-Striebel Smoother
SINS	Strapdown Inertial Navigation Systems
STD	Standard Deviations
TFS	Two-filter Smoother
UTM	Universal Transverse Mercator
VRW	Velocity Random Walk
ZUPT	Zero-velocity Update

Chapter One: INTRODUCTION

1.1 Background

Inertial Navigation Systems (INSs) were widely applied as either the dominant or the associated equipments for navigations of long-range travelling vehicles, such as submarines, aerotransports, or commercial airliners. Since late 1970s, optical gyroscope-based INS was employed as the well-functioned complement in the integrated radio navigation systems in aviation applications (King, 1998). With the tremendous development of the Global Positioning Systems (GPS) and Micro-Electro-Mechanical Systems (MEMS) inertial sensors, tactical-grade and low-cost Inertial Measurement Units (IMUs) have gained great interests in both civilian and commercial fields in the last decade. It has been proved through research and implementation that the INS/GPS integration is the ideal technique for vehicular navigation. In the mean time, promising potentials using INS exist in civilian and commercial applications for unmanned vehicles, personal navigation, horizontal drilling, etc. (Kim and Sukkarieh, 2002; Syed, 2009; Noureldin, 2002; ElGizawy, 2009).

The Dead-Reckoning (DR) nature of the stand-alone INS results in the error accumulation of navigation parameters. Moreover, low-cost INS confronts the problem of large and unpredictable sensor errors and noises (Niu and El-Sheimy, 2005). Therefore, aiding navigation information becomes essential to overcome these inadequacies. GPS, a Radio-Frequency (RF) signal-based system, is capable of providing absolute positioning solutions with long-term accuracy under all weather conditions (Kaplan and Hegarty, 2006). However, this performance is usually interrupted by frequent signal outages, multipath, and poor satellite visibility in urban, dense foliage or canyon areas. The integration of INS and GPS takes advantage of the complementary attributes of both systems and outperforms either single system operated alone (Yang, 2008). Different integration strategies, i.e. loose-coupled, tightly-coupled, and deeply-coupled INS/GPS integrations, have been researched and developed since the last decade (Petovello, 2003).

Due to the dependency on Line-Of-Sight (LOS) measurements, the high-accuracy, continuous GPS positioning updates are not available in the isolated or signal-degraded environments such as tunnels, mines or indoor areas. Under these conditions, the information from alternate navigation-related techniques needs to be integrated with the stand-alone INS to limit the navigation error growth. Among them, the aiding performance of odometers, magnetometers, and non-holonomic constraints are most commonly used during GPS signal outages in land-vehicle navigation (Shin, 2001; Shin, 2005). Zero-Velocity Update (ZUPT) is another efficient method to improve the navigation accuracy by limiting the growing velocity errors with appropriately chosen time durations and intervals (El-Sheimy, 2007). Further, Coordinate Update (CUPT), occasionally available at certain predetermined surveying stations (i.e. control points), is capable of helping to improve the navigation performance and achieve high accuracy positioning measurements. The integration strategies with INS and the aiding techniques have been demonstrated to be feasible for pipeline surveys, pedestrian navigation, and vertical mine shaft surveys (Shin and El-Sheimy, 2005; Syed, 2009; Skaloud and Schwarz, 2000).

Kalman Filter (KF) is recognized as the classic real-time estimation method to integrate multi-sensor information from INS and aiding sources. In the KF context of integration systems, INS provides the predictions as well as the system knowledge, while the aiding sensors provide the measurement updates. Extended Kalman Filter (EKF) is utilized to resolve the nonlinearity problem in the INS navigation equations; it simply applies the Taylor series expansion on the nonlinear system along with observation equations, and takes terms to the first order, where the Probability Density Function (PDF) is approximated by a Gaussian distribution (Gordon et al, 1993). KF is a recursive algorithm that implements a series of prediction and measurement update steps to obtain the optimal estimates based on minimum variance criterion (Gelb, 1974). It will only work in prediction mode during measurement gaps where the navigation solution accuracy degrades rapidly with time. As a result, this performance cannot meet the accuracy requirements of several navigation and surveying applications. Hence, post-processing methods such as backward smoothing can be employed in this case to yield better navigation solutions.

Optimal smoothing is a post-mission estimator that provides the optimal estimates by utilizing all available past, current and future measurements (Gelb, 1974). The fixed-interval smoother has been used in most navigation applications compared to other types such as fixed-point and fixed-lag smoothing algorithms (Nassar et. al, 2005). In addition, fixed-interval smoothing has been used in most surveying applications, because surveying is typically amenable to post-processing where best position information is pursued for all measured points (Shin and El-Sheimy, 2002). The Rauch-Tung-Striebel Smoother (RTSS) (Rauch et al., 1965) has been widely applied in navigations due to its robustness and effectiveness. The RTSS does not require the process of the full-scale Backward Kalman Filter (BKF). By utilizing all the information stored in the Forward Kalman Filter (FKF), the RTSS recursively updates the smoothed estimate and its covariance in a backward sweep.

Fraser and Potter (1969) proposed that the fixed-interval smoother can be accomplished by a combination of two Kalman filters manipulated forward and backward, i.e. FKF and BKF, using a series of convenient discrete-time equations. It has been demonstrated that the aforementioned Two Filter Smoother (TFS) and the RTS smoother are mathematically equivalent in linear cases (Crassidis and Junkins, 2004). However, the traditional TFS was originally designed for linear systems. Therefore, it was not applicable for INS-based multi-sensor systems because of the high nonlinear characteristics in the INS navigation equations. The further attempt of applying the common EKF both forward and backward failed to accurately estimate the smoothing INS error states. This problem was resolved by a revised smoothing algorithm that was proposed specifically for pipeline surveys using inertial measurements units (Yu et al., 2005). The main idea in such modification was that the BKF nominal trajectory is assumed to track both the FKF prediction and update results rather than the predictions only (Liu et al., 2009). In this thesis, a special attention will be devoted to discussing and analyzing the TFS for all mentioned INS-based applications since very little research has been published before in this area.

1.2 Objectives

The overall objective of this thesis is to evaluate the performance of Kalman filtering as well as the optimal smoothing methodologies in different applications and conditions using INS-based integrated systems. Land-vehicle navigation will firstly be investigated to verify the feasibility of different smoothers where GPS updates are sufficiently and continuously provided except for periods of GPS signal outages. Further, the forward filter and the backward smoothing algorithms will be implemented and investigated in the non-GPS navigation applications, including the pipeline surveys and horizontal/vertical building surveys. CUPTs at Above Ground Markers (AGM) and odometer-based velocities will provide auxiliary navigation information in pipeline surveying systems. On the other hand, frequent ZUPTs and CUPTs at predetermined control points will be used as the aiding sources for horizontal/vertical building surveying application.

The above objective is accomplished through performing the following research tasks:

1. To employ and implement KFs for INS/GPS, INS/CUPT/ODOM, and INS/CUPT/ZUPT integration schemes.
2. To employ, develop and implement backward smoothing algorithms (TFS and RTSS) for INS/GPS, INS/CUPT/ODOM, and INS/CUPT/ZUPT integrations.

3. To demonstrate the estimation accuracy enhancement of both smoothers by analyzing and discussing the corresponding navigation results in different INS-based applications.

1.3 Thesis Outline

Chapter 2 presents the fundamentals of INS and the aiding techniques. The background of different reference frames and attitude parameterization will be introduced. Using the derived continuous-time INS navigation equations, INS mechanization formulas will be derived and discussed in discrete-time form. A 21-state INS error model and the corresponding measurement models of different aiding sources will be derived for the KF. Inertial sensor calibration and INS initial alignment will be reviewed and discussed.

Chapter 3 discusses the optimal estimation techniques for INS-based integrated systems. An overview of KF and EKF will be introduced as well as the FKF and BKF mathematical concepts. The two different fixed-interval smoothing algorithms, i.e. the TFS and RTSS, will be discussed and compared. A special emphasis will be directed towards presenting the details of the modification requirements of the developed TFS to overcome the nonlinearity problems. In this case, the rigorous mathematical derivations are given. In addition, the considerations related to smoothers will be investigated.

Chapter 4 evaluates the performance of Kalman Filter and smoothers for land-vehicle navigation using integrated INS/GPS systems. Two land-vehicle field tests are utilized.

The first dataset incorporates a tactical-grade IMU (Litton LN200) while the second one utilizes a custom-built MEMS IMU developed by the MMSS Research Group at UofC. The achieved results for both tests will be analyzed and discussed.

Chapter 5 evaluates the performance of the different developed estimation techniques for pipeline surveys using integrated INS/ODOM/CUPT systems including the KF, RTSS, and TFS algorithms. A 21-hour long pipeline surveying dataset using tactical-grade IMU (Litton LN200) will be used to demonstrate the positioning navigation accuracy improvement of the designed smoothing methodologies.

Chapter 6 investigates the feasibility and the performance of the integrated INS/CUPT/ZUPT systems for the horizontal/vertical building surveying application. The corresponding KF, RTSS, and TFS modules will be designed and implemented respectively. Two building surveying tests using the LN200 IMU are conducted to evaluate and compare the horizontal/vertical surveying performance of filters and smoothers. The first one is a horizontal surveying test along a fixed route inside and outside a campus building with predetermined CUPT points. The second test is a vertical test performed in a 7-floor campus elevator aided with the relative height of each floor measured by trigonometric levelling techniques (i.e. a total station).

Chapter 7 presents the summary and main conclusions of the thesis and discusses the recommendations for potential future work.

Chapter Two: INERTIAL NAVIGATION SYSTEMS AND AIDING TECHNIQUES

2.1 Overview of Aided Inertial Navigation Systems

The publication of Schuler Pendulum principle issued the theory reference for inertial navigation which was firstly applied by Germany in 1942 (King, 1998). The upcoming Gimbaled Inertial Navigation Systems (GINSs) that were successfully designed for aircrafts and submarines, however, relied on complex, sizable, expensive but precise gimbaled platforms and gyroscopes (Stevenson et al., 1970). The invention of light-weight digital computers permitted to remove the mechanical parts and triggered the appearance of Strapdown INSs (SINSs) (Savage, 2004). With the development of miniaturized optical and MEMS gyroscopes, SINS gained many advantages including smaller volume, less power requirement, lower cost and faster respond. After the Global Positioning System (GPS) Selective Availability (SA) error removal and the Galileo plan agreement (Kaplan and Hegarty, 2006), low-cost INS/GPS integration was widely researched and applied in civilian navigation fields during the last decade.

INS is built with inertial sensors: accelerometers sensing linear accelerations and gyroscopes (gyros) sensing angular rotation rates. Orthogonally mounted inertial sensor triads on a rigid body compose the Inertial Measurement Unit (IMU), the key component of a SINS. IMU computes navigation solutions by processing the inertial sensor measurements through the mechanization equations with respect to the predefined reference frame. With the IMU rigidly tied on the host, SINS is considered to be a self-contained Dead-Reckoning (DR) system as it is capable of providing the complete 3-D navigation parameters, namely positions, velocities and attitudes, without any external signal receiving or transmission (Jekeli, 2001).

Generally speaking, the IMU performance is dominated by the gyroscope accuracy (Abdel-Hamid, 2005). According to the sensor characteristics including biases and scale factors, gyroscopes are usually classified into several categories: strategic-grade, navigation-grade, tactical-grade and customer-grade gyroscopes (El-Sheimy, 2007). Another classification is based on the manufacture principles: mechanical gyros, suspended gyros, Ring Laser Gyros (RLG), Fiber Optical Gyros (FOG) and MEMS gyros. Considering the requirement of low-cost and miniaturization, SINS is based on the tactical-grade and customer-grade gyroscopes (Titterton and Weston, 2004). An investigation of gyroscope technology with respect to the sensor bias and scale factor is roughly described in Figure 2.1.

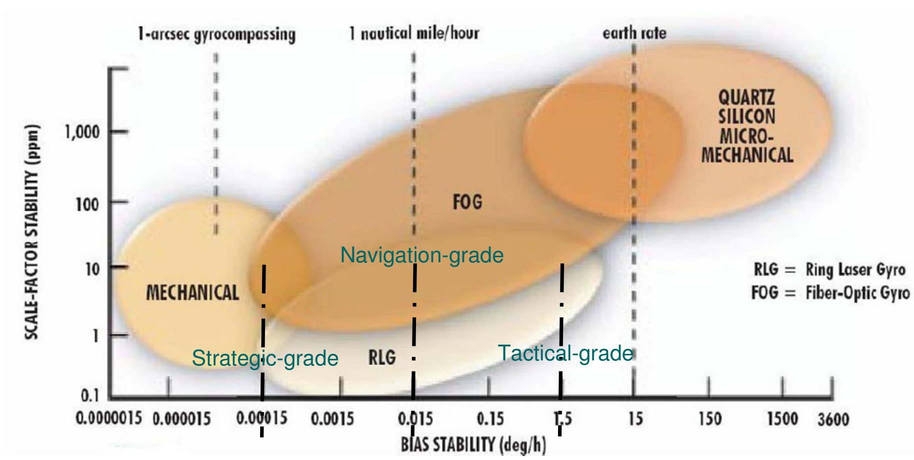

Figure 2.1 Investigation of Gyroscope Technology (After El-Sheimy, 2007)

Compared to the development of gyros, accelerometers are much more successfully designed and produced to achieve the miniaturization and inexpensiveness simultaneously. Performance of accelerometer technology is described with respect to the sensor bias and scale factor, as shown in Figure 2.2.

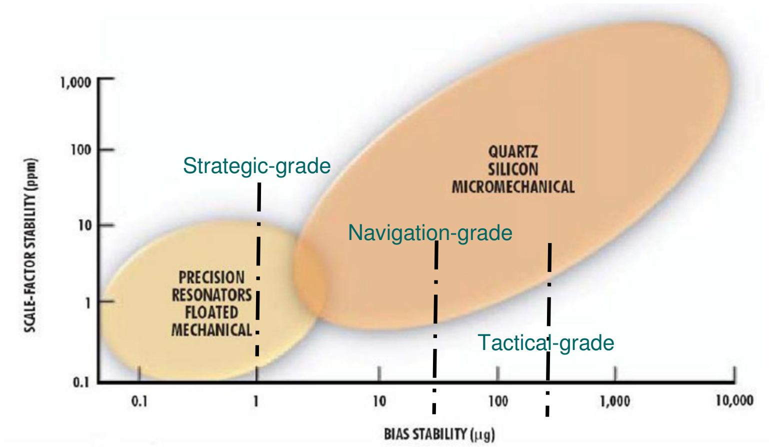

Figure 2.2 Investigation of Accelerometer Technology (After El-Sheimy, 2007)

Compared to the higher-grade systems, low-cost INS confronts the problems of large and unpredictable sensor errors and noises. This inadequacy leads to the fast navigation error accumulation over short time intervals (Nassar, 2003). The inertial sensor calibration techniques are essential to model the determinant errors and uncertainties. Another practical way to improve the accuracy is aiding the INS with other complementary sensors or navigation-related information (Shin, 2005). The augmentation navigation means in this thesis comprise: GPS, odometers, non-holonomic constraints, Zero Velocity Updates (ZUPTs), and Coordinate Updates (CUPTs).

2.2 Overview of Reference Frames and Attitude Parameterization

SINS algorithms require frequent transformations between different reference frames, in which the sensor measurements and navigation states are defined. On the other hand, background information about attitude representations and their conversions is an foundation for the reference frame transformations. The details related to the reference frames and attitude parameterization will be discussed in this section.

2.2.1 Reference Frame

Frequently used reference frames in SINS are listed as follows:

Inertial Frame (i-frame)

An inertial frame is idealized as a right-handed orthogonal, non-rotating and non-accelerating frame with respect to fixed stars. An operational i-frame is realized by defining its origin at the Earth center, its z-axis parallel to the Earth instantaneous spin axis, and its x-axis pointing towards the vernal equinox (Petovello, 2003).

Earth-Centered Earth-Fixed Frame (ECEF or e-frame)

ECEF is defined as a right-handed orthogonal frame which has its origin at the Earth center, its z-axis parallel to the Earth mean spin axis, and its x-axis pointing towards the mean meridian of Greenwich.

Navigation Frame (n-frame)

The navigation frame is a local geodetic frame. In this thesis, it is defined as the north-east-down (NED) right-handed frame.

Body Frame (b-frame) and Host Frame (h-frame)

The body frame is the same as the IMU orthogonal body axis in which the accelerations and angular rotation rates by inertial sensors are resolved (Scherzinger, 1996). The host frame is defined as the forward-right-down axis set aligned with the roll, pitch and heading axes of the host. In SINS, the b-frame and h-frame are assumed to be overlapped for convenience.

Computer Frame (c-frame) and Platform Frame (p-frame)

The computer frame is the assumed navigation frame by the SINS computer. The platform frame is the assumed inertial stabilized platform axis set in which the measurements from the hypothesized inertial sensors are resolved (Scherzinger, 1996). P-frame is actually the b-frame counterpart in Gimbaled INSs.

2.2.2 Attitude Representations

Frequently used attitude representation methods in SINS are listed as follows:

Angular Rotation Vector and Angular Velocity

The transformation of a frame from its initial orientation to its final destination, or the transformation between two different frames is preferred to be represented with a single rotation operation around its direction axis. Angular rotation vector describes the magnitude and the direction of this rotation in a 3×1 vector $\mu = \begin{bmatrix} \mu_x & \mu_y & \mu_z \end{bmatrix}^T$.

Angular velocity describes the rotation speed and the instantaneous axis direction about which the rotation occurs. It is usually represented by a vector of three components as,

$$\omega_{\alpha\beta}^{\gamma} = \begin{bmatrix} \omega_x \\ \omega_y \\ \omega_z \end{bmatrix} \tag{2.1}$$

where the superscript γ denotes the coordinate frame in which the angular velocity components are projected (it is normally set as the frame β); the subscript $\alpha\beta$ denotes that the coordinate frame β rotates with respect to frame α.

An alternative expression of angular velocity is the skew-symmetric matrix form as (El-Sheimy, 2007),

$$\Omega_{\alpha\beta}^{\beta} = (\omega_{\alpha\beta}^{\beta}\times) = \begin{bmatrix} 0 & -\omega_z & \omega_y \\ \omega_z & 0 & -\omega_x \\ -\omega_y & \omega_x & 0 \end{bmatrix} \tag{2.2}$$

The relationship between angular rotation vector and angular velocity is described as (Bortz, 1971),

$$\dot{\mu} = d\mu/dt \approx \omega_{\alpha\beta}^{\beta} + \frac{1}{2}\mu \times \omega_{\alpha\beta}^{\beta} + \frac{1}{12}\mu \times (\mu \times \omega_{\alpha\beta}^{\beta}) \tag{2.3}$$

Euler Angles and Directional Cosine Matrix (DCM)

An Euler angle is the rotation angle about one coordinate frame axis. The relative orientation between two frames can be decomposed as a sequence of three rotations expressed by Euler angles. Mathematically, it can be explained as a product of three elementary rotation matrix obtained by Euler angles (Savage, 2004). This product is defined as Directional Cosine Matrix (DCM) as one of the main methods for attitude parameterization.

The Euler angle elementary matrix and the corresponding DCM are formulated as,

$$\begin{aligned} C_{\alpha}^{\beta} &= R_x(\theta_x)R_y(\theta_y)R_z(\theta_z) \\ &= \begin{bmatrix} 1 & 0 & 0 \\ 0 & \cos\theta_x & \sin\theta_x \\ 0 & -\sin\theta_x & \cos\theta_x \end{bmatrix} \begin{bmatrix} \cos\theta_y & 0 & -\sin\theta_y \\ 0 & 1 & 0 \\ \sin\theta_y & 0 & \cos\theta_y \end{bmatrix} \begin{bmatrix} \cos\theta_z & \sin\theta_z & 0 \\ -\sin\theta_z & \cos\theta_z & 0 \\ 0 & 0 & 1 \end{bmatrix} \end{aligned} \tag{2.4}$$

where,

θ denotes the Euler angle;

C_{α}^{β} denotes the DCM from α frame to β frame;

R denotes an elementary rotation matrix, and its subscript denotes the instantaneous axis about which the Euler angle is rotated.

Attitude Quaternion

Quaternion implementation is preferred in updating the attitude in INS as the linearity of quaternion differential equations, the lack of trigonometric functions, and the small number of parameters allow efficient algorithm (Farrell and Barth, 1998). Similar to the angular rotation vector, quaternion defines the frame transformation using a single rotation about its direction axis. It is represented in a 4×1 parameter vector by the rotation vector as (Savage, 2004),

$$q_\beta^\alpha = \begin{bmatrix} \dfrac{\sin\|0.5\mu\|}{\|\mu\|}\mu \\ \cos\|0.5\mu\| \end{bmatrix} = \begin{bmatrix} \dfrac{\sin\|0.5\mu\|}{\|\mu\|}\mu_x \\ \dfrac{\sin\|0.5\mu\|}{\|\mu\|}\mu_y \\ \dfrac{\sin\|0.5\mu\|}{\|\mu\|}\mu_z \\ \cos\|0.5\mu\| \end{bmatrix} \tag{2.5}$$

where,

q_β^α denotes the quaternion, which signifies the rotation from α frame to β frame;

$\|\mu\|$ denotes the Euclidean norm of the rotation vector, which is the rotation magnitude as,

$$\|\mu\| = \sqrt{\mu_x^2 + \mu_y^2 + \mu_z^2} \tag{2.6}$$

The product of quaternion vectors represents a series of continuous rotations as,

$$q_\beta^\alpha = q_\gamma^\alpha \bullet q_\beta^\gamma = \begin{bmatrix} V_1 \\ s_1 \end{bmatrix} \bullet \begin{bmatrix} V_2 \\ s_2 \end{bmatrix} = \begin{bmatrix} s_1V_2 + s_2V_1 + V_1 \times V_2 \\ s_1s_2 - V_1^TV_2 \end{bmatrix} \tag{2.7}$$

where,

$\bullet$ denotes the quaternion product; $\times$ denotes the vector cross product;

V denotes the vector part of a quaternion, which is composed of first three components;

s denotes the scalar part of a quaternion, which is the last component.

The conjugate quaternion is described as,

$$(q_{\beta}^{\alpha})^{-1} = q_{\alpha}^{\beta} = \begin{bmatrix} -\dfrac{\sin\|0.5\mu\|}{\|\mu\|}\mu \\ \cos\|0.5\mu\| \end{bmatrix} \tag{2.8}$$

where $(q_{\beta}^{\alpha})^{-1}$ denotes the conjugate quaternion of q_{β}^{α}.

2.2.3 Reference Frame Transformations

Frequently used reference frame transformations in SINS are discussed below.

Transformations between i-frame, e-frame and n-frame

The relationship between i-frame, e-frame and n-frame are depicted in Figure 2.3. The DCM from n-frame to e-frame is expressed in terms of the geodetic latitude φ and longitude λ as,

$$C_e^n = R_y(-\varphi - \pi/2)R_z(\lambda)$$
$$= \begin{bmatrix} -\sin\varphi\cos\lambda & -\sin\varphi\sin\lambda & \cos\varphi \\ -\sin\lambda & \cos\lambda & 0 \\ -\cos\varphi\cos\lambda & -\cos\varphi\sin\lambda & -\sin\varphi \end{bmatrix} \tag{2.9}$$

The corresponding quaternion is,

$$q_n^e = \begin{bmatrix} -\sin(-\pi/4-\varphi/2)\sin(\lambda/2) \\ \sin(-\pi/4-\varphi/2)\cos(\lambda/2) \\ \cos(-\pi/4-\varphi/2)\sin(\lambda/2) \\ \cos(-\pi/4-\varphi/2)\cos(\lambda/2) \end{bmatrix} \tag{2.10}$$

The angular velocities frequently used are listed as (Titterton and Weston, 2004; El-Sheimy, 2007),

$$\omega_{ie}^e = [0 \quad 0 \quad \omega_e]^T; \omega_e = 7.2921158 rad/s \tag{2.11}$$

$$\omega_{ie}^n = C_e^n \omega_{ie}^e = [\omega_e \cos\varphi \quad 0 \quad -\omega_e \sin\varphi]^T \tag{2.12}$$

$$\omega_{en}^n = [\dot\lambda\cos\varphi \quad -\dot\varphi \quad -\dot\lambda\sin\varphi]^T$$
$$= [v_E/(N+h) \quad -v_N/(M+h) \quad -v_E\tan\varphi/(N+h)]^T \tag{2.13}$$

where,

v_E, v_N are the east and north velocities;

N, M are the meridian and prime vertical radii of curvature;

h is the ellipsoidal height;

$$\dot\lambda = v_E/(N+h)/\cos\varphi; \dot\varphi = v_N/(M+h) \tag{2.14}$$

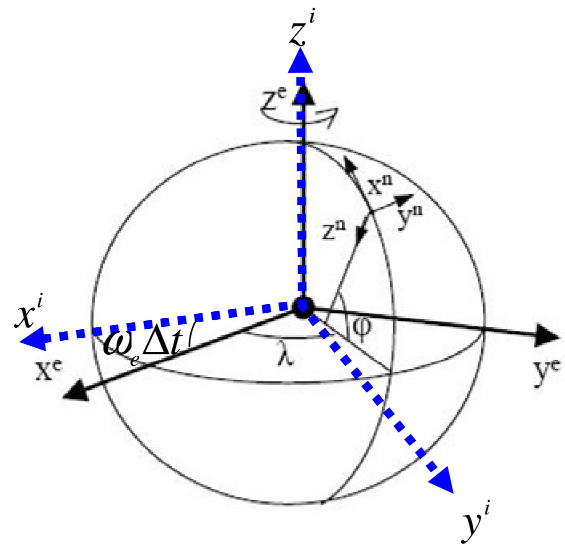

Figure 2.3 i-frame, e-frame and n-frame (After Shin, 2005)

Transformations between b-frame and n-frame

The DCM from b-frame to n-frame is given as (Shin, 2001):

$$
\begin{aligned}
C_b^n &= R_z(-A)R_y(-p)R_x(-r) \\
&= \begin{bmatrix} \cos A & -\sin A & 0 \\ \sin A & \cos A & 0 \\ 0 & 0 & 1 \end{bmatrix} \begin{bmatrix} \cos p & 0 & \sin p \\ 0 & 1 & 0 \\ -\sin p & 0 & \cos p \end{bmatrix} \begin{bmatrix} 1 & 0 & 0 \\ 0 & \cos r & -\sin r \\ 0 & \sin r & \cos r \end{bmatrix} \\
&= \begin{bmatrix} \cos p \cos A & -\cos r \sin A + \sin r \sin p \cos A & \sin r \sin A + \cos r \sin p \cos A \\ \cos p \sin A & \cos r \cos A + \sin r \sin p \sin A & -\sin r \cos A + \cos r \sin p \sin A \\ -\sin p & \sin r \cos p & \cos r \cos p \end{bmatrix}
\end{aligned}
\tag{2.15}
$$

where r, p, A are the roll, pitch and heading angles, which are the three components of Euler angles.

The conversion from DCM to the Euler angles is shown as (Farrell and Barth, 1998):

$$p = -\tan^{-1}\left(\frac{c_{31}}{\sqrt{1-c_{31}^2}}\right)$$
$$r = \tan^{-1}(c_{32}/c_{33}) \tag{2.16}$$
$$A = \tan^{-1}(c_{21}/c_{11})$$

where c_{ij} is the (i, j) element in DCM C_b^n.

The conversions between quaternion and DCM are shown as (Shin, 2001):

$$C_b^n = \begin{bmatrix} q_1^2 - q_2^2 - q_3^2 + q_4^2 & 2(q_1q_2 - q_3q_4) & 2(q_1q_3 - q_2q_4) \\ 2(q_1q_2 + q_3q_4) & q_1^2 - q_2^2 - q_3^2 + q_4^2 & 2(q_2q_3 - q_1q_4) \\ 2(q_1q_3 - q_2q_4) & 2(q_2q_3 + q_1q_4) & q_1^2 - q_2^2 - q_3^2 + q_4^2 \end{bmatrix} \tag{2.17}$$

and,

$$q_n^b = \begin{bmatrix} q_1 \\ q_2 \\ q_3 \\ q_4 \end{bmatrix} = \begin{bmatrix} 0.25(c_{32} - c_{23})/0.5/\sqrt{1 + c_{11} + c_{22} + c_{33}} \\ 0.25(c_{13} - c_{31})/0.5/\sqrt{1 + c_{11} + c_{22} + c_{33}} \\ 0.25(c_{21} - c_{12})/0.5/\sqrt{1 + c_{11} + c_{22} + c_{33}} \\ 0.5\sqrt{1 + c_{11} + c_{22} + c_{33}} \end{bmatrix} \tag{2.18}$$

Transformations between n-frame, c-frame and p-frame

The relationship between n-frame, c-frame and p-frame is illustrated in Figure 2.4, where the perturbation angle from n-frame to c-frame is defined as $\delta\theta$, the perturbation angle from n-frame to p-frame is defined as ϕ, and the perturbation angle from c-frame to p-frame is defined as ψ. Since all these misalignments are small angles, the following equations are yielded as (Scherzinger, 1996; Shin, 2005),

$$\begin{aligned}\delta\theta &= \begin{bmatrix}\delta\lambda\cos\varphi & -\delta\varphi & -\delta\lambda\sin\varphi\end{bmatrix}^T \\ &= [\delta v_E/(N+h) \quad -\delta v_N/(M+h) \quad -\delta v_E \tan\varphi/(N+h)]^T\end{aligned} \tag{2.19}$$

$$C_n^c = I - (\delta\theta\times); C_c^p = I - (\psi\times); C_n^p = I - (\phi\times) \tag{2.20}$$

$$\phi = \psi + \delta\theta \tag{2.21}$$

where,

$\delta\lambda, \delta\varphi$ denote the latitude and longitude errors;

$\delta v_N, \delta v_E$ denote the north and east velocity errors;

$(\times)$ denotes the skew symmetric matrix of a three element vector.

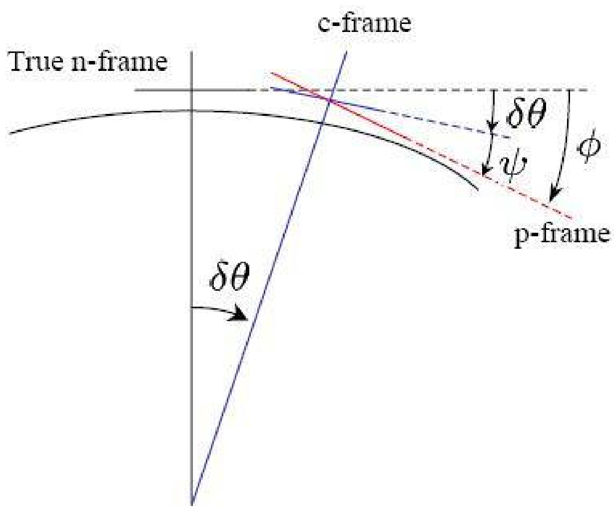

Figure 2.4 n-frame, c-frame and p-frame (After Shin, 2005)

2.3 Inertial Navigation System (INS) Fundamentals

2.3.1 INS Navigation Equations

Without a detailed derivation, the INS navigation equations in the n-frame which define the dynamics model of the navigation states in continuous-time domain can be described as (Schwarz and Wei, 1999; Savage, 2004),

$$\begin{bmatrix} \dot{r}^n \\ \dot{v}^n \\ \dot{C}_b^n \end{bmatrix} = \begin{bmatrix} D^{-1} v^n \\ C_b^n f^b - (2\omega_{ie}^n + \omega_{en}^n) \times v^n + g^n \\ C_b^n (\omega_{ib}^b \times) - (\omega_{in}^n \times) C_b^n \end{bmatrix} \tag{2.22}$$

where,

$r^n = [\varphi \quad \lambda \quad h]^T$ is defined as the position vector, which is essentially the polar coordinate expression in e-frame; its Cartesian coordinate counterpart is

$$\begin{aligned} r^e &= [r_x \quad r_y \quad r_z]^T \\ &= [(N+h)\cos\varphi\cos\lambda \quad (N+h)\cos\varphi\sin\lambda \quad (N(1-e^2)+h)\sin\varphi]^T \end{aligned} \tag{2.23}$$

with e is the first eccentricity of reference ellipsoid;

f^b, ω_{ib}^b are the specific force and angular rate measurements from inertial sensors projected in b-frame, which are the time-varying parameters in navigation equations;

g^n denotes the gravity vector in n-frame;

$$D^{-1} = \begin{bmatrix} 1/(M+h) & 0 & 0 \\ 0 & 1/(M+h)/\cos\varphi & 0 \\ 0 & 0 & -1 \end{bmatrix} \tag{2.24}$$

2.3.2 Inertial Sensor Calibration and Measurement Error Compensation

Generally, the raw outputs of inertial sensors are corrupted by biases, scale factors, non-orthogonalities and noises, shown as in Eq. (2.25)-(2.26).

$$\tilde{\omega}_k = \begin{bmatrix} \tilde{\omega}_k^x \\ \tilde{\omega}_k^y \\ \tilde{\omega}_k^z \end{bmatrix} = b_{g0} + b_{gk} + (I + L_{g0} + L_{gk})\omega_k + w_{gk} \qquad \textbf{(2.25)}$$

$$\tilde{f}_k = \begin{bmatrix} \tilde{f}_k^x \\ \tilde{f}_k^y \\ \tilde{f}_k^z \end{bmatrix} = b_{acc0} + b_{acck} + (I + L_{acc0} + L_{acck}) f_k + w_{acck} \qquad \textbf{(2.26)}$$

where,

the superscripts x, y, z denote the sensor triad axes;

the subscripts 0 denote the determinant sensor error; the subscripts k denote the random sensor error at time epoch t_k ;

the subscripts g denote the gyroscope; the subscripts acc denote the accelerometer;

$\tilde{f}$, f denote the vectors of the raw accelerometer outputs and the true specific force;

$\tilde{\omega}$, ω denote the vectors of the raw gyro outputs and the true angular rate;

b denotes the bias vector; w denotes the random noise;

L denotes the linear sensor error matrix with scale factor SF and non-orthogonality r as,

$$L_{g0}=\begin{bmatrix} SF_{g0}^{x} & r_{g0}^{xy} & r_{g0}^{xz} \\ r_{g0}^{yx} & SF_{g0}^{y} & r_{g0}^{yz} \\ r_{g0}^{zx} & r_{g0}^{zy} & SF_{g0}^{z} \end{bmatrix}; L_{g,k}=\begin{bmatrix} SF_{gk}^{x} & r_{gk}^{xy} & r_{gk}^{xz} \\ r_{gk}^{yx} & SF_{gk}^{y} & r_{gk}^{yz} \\ r_{gk}^{zx} & r_{gk}^{zy} & SF_{gk}^{z} \end{bmatrix}$$

$$L_{acc0}=\begin{bmatrix} SF_{acc0}^{x} & r_{acc0}^{xy} & r_{acc0}^{xz} \\ r_{acc0}^{yx} & SF_{acc0}^{y} & r_{acc0}^{yz} \\ r_{acc0}^{zx} & r_{acc0}^{zy} & SF_{acc0}^{z} \end{bmatrix}; L_{acck}\begin{bmatrix} SF_{acck}^{x} & r_{acck}^{xy} & r_{acck}^{xz} \\ r_{acck}^{yx} & SF_{acck}^{y} & r_{acck}^{yz} \\ r_{acck}^{zx} & r_{acck}^{zy} & SF_{acck}^{z} \end{bmatrix} \quad \textbf{(2.27)}$$

The process to calculate or estimate these determinant or random sensor error parameters, i.e. biases, scale factors, and non-orthogonalities, is known as sensor calibration. Determinant sensor errors are preferred to be calibrated beforehand in laboratory. Normal SINS laboratory calibration technologies are following the idea to compare the IMU outputs with the reference information including gravity and earth rotation rate (Niu et al., 2006). The random errors are always mathematically modeled as stochastic processes (Nassar, 2003). Allan Variance method is utilized as part of the lab work to determine the model types and estimate the model parameters for the random noise (Hou, 2004). Random sensor error parameters can be calibrated in field tests or be estimated on-line in the integrated navigation systems. The effect of random errors will be suppressed using optimal estimation methods with aiding sources, as discussed in the succeeding chapters.

With calibrated parameters, sensor errors can be compensated from raw outputs as,

$$\omega_k = (I + L_{g0} + L_{gk})^{-1}(\tilde{\omega}_k - b_{g0} - b_{gk}) \quad \textbf{(2.28)}$$

$$f_k = (I + L_{acc0} + L_{acck})^{-1}(\tilde{f}_k - b_{acc0} - b_{acck}) \quad \textbf{(2.29)}$$

Instead of specific forces and angular rates, incremental velocities and angles are the outputs in most of the high-grade IMUs. Integration procedures to relate the two types of IMU outputs are introduced as follows (Savage, 2004),

$$\Delta\theta_k = \int_{t_{k-1}}^{t_k} \omega dt \approx \omega_k \Delta t_k \tag{2.30}$$

$$\Delta v_k = \int_{t_{k-1}}^{t_k} f dt \approx f_k \Delta t_k \tag{2.31}$$

where

$\Delta\theta, \Delta v$ denote the incremental angles and velocities;

$\Delta t = t_k - t_{k-1}$ is the time increment.

2.3.3 INS Mechanization

SINS mechanization is defined as the integration process to calculate the navigation states, i.e. positions, velocities and attitudes, with raw inertial sensor measurements. Therefore, the mechanization algorithm can be regarded as the discrete-time form of the INS navigation equations. Several approximation methods were applied to solve the quaternion differential equations in attitude integration. Further, a single-speed mechanization algorithm considering midway navigation states and applying quaternion algebras was developed by Savage (2004). Forward SINS mechanization is the integration process to determine the navigation states from the previous time epoch t_{k-1} to the current time epoch t_k using compensated IMU outputs. Its simplification by Shin (2005) will be summarized in this thesis.

Velocity Integration

The discrete-time form of the second component in Eq. (2.22) can be written as,

$$v_k^n = v_{k-1}^n + \Delta v_{fk}^n + \Delta v_{ek}^n \quad \textbf{(2.32)}$$

$$\Delta v_{fk}^n = [I - (0.5\varsigma_k \times)] C_{bk-1}^{nk-1} \Delta v_{fk}^{bk-1} \quad \textbf{(2.33)}$$

$$\varsigma_k = [\omega_{ie}^n + \omega_{en}^n]_{k-1/2} \Delta t_k \quad \textbf{(2.34)}$$

$$\Delta v_{fk}^{bk-1} = \Delta v_{fk}^b + \frac{1}{2}\Delta\theta_k \times \Delta v_{fk}^b + \frac{1}{12}(\Delta\theta_{k-1} \times \Delta v_{fk}^b + \Delta v_{fk-1}^b \times \Delta\theta_k) \quad \textbf{(2.35)}$$

$$\Delta v_{ek}^n = [g^n - (2\omega_{ie}^n + \omega_{en}^n) \times v^n]_{k-1/2} \Delta t_k \quad \textbf{(2.36)}$$

where,

the subscripts $k-1, k-1/2, k$ denote the previous, midway and current time epochs $t_{k-1}, t_{k-1/2}, t_k$ respectively;

the subscripts bk denote the corresponding variable is projected to the b-frame at t_k;

Δv_{ek}^n is the increment induced by gravity and Coriolis force;

Δv_{fk}^n is the increment induced by specific force;

ς_k is the n-frame rotation vector from $(n, k-1)$ to (n, k);

the second and third terms at the right of Eq. (2.35) are the rotational and sculling motion.

Positions at midway are required to be extrapolated from the previous time navigation states as,

$$h_{k-1/2} = h_{k-1} - \frac{v_{Dk-1}\Delta t_k}{2} \quad \textbf{(2.37)}$$

$$\delta\varphi_{k-1/2} = v_{Nk-1} /(M + h_{k-1/2})/2 \quad \textbf{(2.38)}$$

$$\delta\lambda_{k-1/2} = v_{Ek-1} /(N + h_{k-1/2})/\cos(\varphi_{k-1})/2 \quad \textbf{(2.39)}$$

$$\delta\theta_{k-1/2} = [\delta\lambda_{k-1/2}\cos\varphi_{k-1} \quad -\delta\varphi_{k-1/2} \quad -\delta\lambda_{k-1/2}\sin\varphi_{k-1}]^T \quad \textbf{(2.40)}$$

$$q_{\delta\theta_{k-1/2}} = \begin{bmatrix} \frac{\sin\|0.5\delta\theta_{k-1/2}\|}{\|\delta\theta_{k-1/2}\|}\delta\theta_{k-1/2} \\ \cos\|0.5\delta\theta_{k-1/2}\| \end{bmatrix} \quad \textbf{(2.41)}$$

$$q_{nk-1/2}^{ek-1/2} = q_{nk-1}^{ek-1} \bullet q_{\delta\theta_{k-1/2}} \quad \textbf{(2.42)}$$

where the midway latitude and longitude can be extracted from quaternion $q_{nk-1/2}^{ek-1/2}$.

Velocity at midway are extrapolated as,

$$v_{k-1/2}^n = v_{k-1}^n + \frac{\Delta v_{k-1}^n}{2} = v_{k-1}^n + \frac{\Delta v_{fk-1}^n + \Delta v_{ek-1}^n}{2} \quad \textbf{(2.43)}$$

where Δv_{k-1}^n is the second and third velocity increments at the right of Eq. (2.32) stored in the previous epoch.

Position Integration

The midway velocity can be updated by interpolation as,

$$v_{k-1/2}^n = \frac{v_{k-1}^n + v_k^n}{2} \quad \textbf{(2.44)}$$

The height can be updated by the midway downside velocity as,

$$h_k = h_{k-1} - v_{Dk-1/2}\Delta t_k \tag{2.45}$$

The current time quaternion q_{nk}^{ek} containing position information can be updated by the products of e-frame and n-frame rotations as,

$$q_{nk}^{ek-1} = q_{nk-1}^{ek-1} \bullet q_{nk}^{nk-1} \tag{2.46}$$

$$q_{nk}^{ek} = q_{ek-1}^{ek} \bullet q_{nk}^{ek-1} \tag{2.47}$$

$$q_{nk}^{nk-1} = \begin{bmatrix} \dfrac{\sin\|0.5\varsigma_k\|}{\|\varsigma_k\|}\varsigma_k \\ \cos\|0.5\varsigma_k\| \end{bmatrix} \tag{2.48}$$

$$q_{ek-1}^{ek} = \begin{bmatrix} -\dfrac{\sin\|0.5\xi_k\|}{\|\xi_k\|}\xi_k \\ \cos\|0.5\xi_k\| \end{bmatrix} \tag{2.49}$$

$$\xi_k = \omega_{ie}^{e}\Delta t_k \tag{2.50}$$

where,

ς_k is recalculated with the renewed midway velocity using Eq. (2.34);

ξ_k denotes the e-frame rotation vector from $(e, k-1)$ to (e, k);;

$q_{nk}^{nk-1}, q_{ek-1}^{ek}$ denote the quaternion vectors corresponding to the rotation vectors above.

Attitude Integration

The midway positions can be renewed by interpolation as,

$$\varphi_{k-1/2} = \frac{\varphi_{k-1} + \varphi_k}{2} \tag{2.51}$$

$$\lambda_{k-1/2} = \frac{\lambda_{k-1} + \lambda_k}{2} \tag{2.52}$$

$$h_{k-1/2} = \frac{h_{k-1} + h_k}{2} \tag{2.53}$$

The quaternion q_b^n containing attitude information can be updated by the products of n-frame and e-frame rotations as:

$$q_{bk}^{nk-1} = q_{bk-1}^{nk-1} \bullet q_{bk}^{bk-1} \tag{2.54}$$

$$q_{bk}^{nk} = q_{nk-1}^{nk} \bullet q_{bk}^{nk-1} \tag{2.55}$$

$$q_{bk}^{bk-1} = \begin{bmatrix} \dfrac{\sin\|0.5\phi_k\|}{\|\phi_k\|}\phi_k \\ \cos\|0.5\phi_k\| \end{bmatrix} \tag{2.56}$$

$$q_{nk-1}^{n} = \begin{bmatrix} -\dfrac{\sin\|0.5\varsigma_k\|}{\|\varsigma_k\|}\varsigma_k \\ \cos\|0.5\varsigma_k\| \end{bmatrix} \tag{2.57}$$

$$\phi_k \approx \Delta\theta_k + \frac{1}{12}\Delta\theta_{k-1} \times \Delta\theta_k \tag{2.58}$$

where,

ϕ_k is the b-frame rotation vector from $(b, k-1)$ to (b, k);

the second term at the right of Eq. (2.58) denotes the second-order coning correction.

2.3.4 INS Error Model

SINS navigation equations are the non-linear models to describe the dynamics of the navigation states. The linearized equations can be derived by perturbation analysis (Britting, 1971), which are transferred as the models of the navigation error states, i.e. position errors, velocity errors, and attitude angle errors. For convenience, the ψ -angle error model, which indicates the perturbation is conducted with respect to the computer frame, will be utilized in this thesis. In addition, the random sensor error parameters including residual bias and scales factor are modeled as first-order Gauss-Markov processes, of which the model parameters could be determined by auto-correlation analysis or Allan Variance technique. Materials (Nassar, 2003; Shin, 2005; Weinred and Bar-Itzhack, 1978; Scherzinger, 1996) for detailed deductions of the above algorithm models are recommended to readers with interest.

The continuous-time ψ angle error model for navigation states and sensor error states are shown as:

$$\begin{aligned}
\delta\dot{r}^c &= -\omega_{ec}^c \times \delta r^c + \delta v^c \\
\delta\dot{v}^c &= f^c \times \psi - (2\omega_{ie}^c + \omega_{ec}^c) \times \delta v^c + \delta g^c + C_b^n \delta f^b \\
\dot{\psi} &= -(\omega_{ie}^c + \omega_{ec}^c) \times \psi - C_b^n \delta\omega_{ib}^b
\end{aligned} \qquad \textbf{(2.59)}$$

where,

the position error vector is $\delta r^c = [\delta r_N \quad \delta r_E \quad \delta r_D]^T$;

the superscript c denotes the computer frame;

the sensor measurement errors are written as,

$$\delta f^b = b_{acc} + SF_{acc} f^b + w_{acc} \tag{2.60}$$

$$\delta \omega_{ib}^b = b_g + SF_g \omega_{ib}^b + w_g \tag{2.61}$$

the gravity perturbation is,

$$\delta g^c = D_g \delta r^c = diag([\frac{-g}{M+h} \quad \frac{-g}{N+h} \quad \frac{-g}{\sqrt{MN}+h}])\delta r^c \tag{2.62}$$

where the $diag(\bullet)$ denote the diagonal matrix form of a vector.

The stochastic models for the sensor random bias and scale factor are given as first order Gauss-Markov models (Godha, 2006):

$$\dot{b}_{acc}^i = -\alpha_{accb}^i b_{acc}^i + \eta_{accb}^i \tag{2.63}$$

$$\dot{b}_g^i = -\alpha_{gb}^i b_g^i + \eta_{gb}^i \tag{2.64}$$

$$\dot{SF}_{acc}^i = -\alpha_{accSF}^i SF_{acc}^i + \eta_{accSF}^i \tag{2.65}$$

$$\dot{SF}_g^i = -\alpha_{gSF}^i SF_g^i + \eta_{gSF}^i \tag{2.66}$$

where,

the superscript i denotes sensor triad axis of the IMU;

α is the correlation time reciprocal;

the spectral density of the driving noise η is achieved using correlation time reciprocal and the process variance σ^2 as,

$$q = \sqrt{2\alpha\sigma^2} \tag{2.67}$$

The combination of Eq. (2.59) and Eq. (2.63)-(2.66) yields the forward linear dynamics process model with both the navigation error parameters and the sensor error parameters defined as the system states. The discrete-time form of this process model can be given by (Grewal and Andrew, 2001; Brown and Hwang, 1997),

$$\begin{aligned}
\delta x_k &= F_{k-1}\delta x_{k-1} + w_{k-1} = (I + \begin{bmatrix} (F_1)_{9\times 9} & (F_2)_{9\times 12} \\ 0_{12\times 9} & (F_3)_{12\times 12} \end{bmatrix}_{k-1} \Delta t_{k-1})\delta x_{k-1} + w_{k-1} \\
&= \begin{bmatrix} (I + F_1\Delta t_{k-1})_{9\times 9} & (F_2\Delta t_{k-1})_{9\times 12} \\ 0_{12\times 9} & (I + F_3\Delta t_{k-1})_{12\times 12} \end{bmatrix}_{k-1} \delta x_{k-1} + w_{k-1} \\
&= \begin{bmatrix} (F_1')_{9\times 9} & (F_2')_{9\times 12} \\ 0_{12\times 9} & (F_3')_{12\times 12} \end{bmatrix}_{k-1} \delta x_{k-1} + w_{k-1}
\end{aligned} \tag{2.68}$$

where,

the 21 system state vector is,

$$\delta x_k = \begin{bmatrix} (\delta r^c)^T & (\delta v^c)^T & (\psi)^T & (\delta b_g)^T & (\delta b_{acc})^T & (\delta SF_g)^T & (\delta SF_{acc})^T \end{bmatrix}_k^T \tag{2.69}$$

F_{k-1} is the state transition matrix, obtained from the numerical approximation of the continuous-time dynamics matrix $F(t)$, which is composed of the following matrix,

$$F_1 = \begin{bmatrix} -(\omega_{ec}^c \times)_{3\times3} & I_{3\times3} & 0_{3\times3} \\ (D_g)_{3\times3} & [-(2\omega_{ie}^c + \omega_{ec}^c)\times]_{3\times3} & (f^c \times)_{3\times3} \\ 0_{3\times3} & 0_{3\times3} & [-(\omega_{ie}^c + \omega_{ec}^c)\times]_{3\times3} \end{bmatrix} \quad \textbf{(2.70)}$$

$$F_2 = \begin{bmatrix} 0_{3\times3} & 0_{3\times3} & 0_{3\times3} & 0_{3\times3} \\ 0_{3\times3} & C_b^n 0_{3\times3} & 0_{3\times3}{}^b & C_b^n f \\ -C_b^n & 0_{3\times3} & -C_b^n \omega_{ib}^b & 0_{3\times3} \end{bmatrix} \quad \textbf{(2.71)}$$

$$F_3 = -diag(\lfloor(\alpha_{gb})_{1\times3} \quad (\alpha_{accb})_{1\times3} \quad (\alpha_{gSF})_{1\times3} \quad (\alpha_{accSF})_{1\times3}\rfloor) \quad \textbf{(2.72)}$$

the spectral density matrix for the driving noise w in continuous-time domain is,

$$Q = diag(\lfloor 0_{1\times3} \quad (q_{VRW})_{1\times3} \quad (q_{ARW})_{1\times3} \quad (q_{gb})_{1\times3} \quad (q_{accb})_{1\times3} \quad (q_{gSF})_{1\times3} \quad (q_{accSF})_{1\times3}\rfloor) \quad \textbf{(2.73)}$$

where,

q_{VRW}, q_{ARW} are the Velocity Random Walk (VRW) and Attitude Random Walk (ARW) variances;

the spectral density for the Gauss-Markov models of the sensor error parameters in discrete-time domain is,

$$q_k = \sigma^2(1 - e^{2\Delta t_{k-1}\alpha}) \approx \sqrt{2\alpha\sigma^2}\Delta t_{k-1} \quad \textbf{(2.74)}$$

2.3.5 Initial Alignment

INS initial alignment is defined as the process to determine the initial values of the navigation parameters. Dependable position and velocity information can be provided by high-accuracy GPS solutions. Since the accuracy of the initial attitudes predominantly governs the navigation error accumulation, initial alignment is narrowly considered as the procedure to initialize the attitude information, contained in the DCM C_b^n (Britting, 1971). For IMUs whose gyro bias and noise levels are smaller than the values of the Earth rotation rate, such as navigation-grade or high-end tactical-grade IMUs, a coarse alignment followed by a fine alignment can be applied to estimate the initial attitude parameters. The coarse alignment is an analytic method providing the averaged solutions. It can be decomposed as the levelling step, determining the initial roll and pitch, and the gyrocompassing step, determining the heading angle (Titterton and Weston, 2004). With the established DCM from the b-frame to the n-frame, the fine alignment is an optimal estimation method by an INS-only KF using horizontal specific force and east-channel gyro error measurements. Both of the two alignment methods are processed in stationary mode and implemented on the basis of the reference information including gravity and Earth rotation rate (Farrell and Barth, 1998).

For low-cost IMUs, the poor gyroscope characteristics result in the failing of initial heading alignment (Godha, 2006). On the other hand, stationary alignment cannot meet the real-time consideration in civilian and commercial applications, such as vehicle navigation (Shin, 2001). Aiding sources including magnetometers, GPS multi-antenna systems and/or GPS-derived velocity information are indispensable to the in-motion alignment techniques. Besides, kinematic alignment is researched from the system observability point of view in aircraft applications (Bar-Itzhack and Porat, 1980).

2.4 Measurement Models for Aiding Sources

Since the EKF is commonly applied to resolve the non-linearity in system model, it is the measurement misclosure, or the difference between the INS mechanization outputs and the observations from aiding sources that is concerned in the INS-based integration systems,

$$\delta \tilde{z}_k = \tilde{z}_{INS} - \tilde{z}_{aiding} \tag{2.75}$$

where $\tilde{z}_{INS}$ is the INS mechanization solution; $\tilde{z}_{aiding}$ is the aiding sensor observation.

2.4.1 Global Positioning System (GPS)

The GPS is a Global Navigation Satellite System (GNSS) developed by the United States Department of Defence (DOD), which provides absolute positioning information and long-term accuracy under all weather conditions (Kaplan and Hegarty, 2006). Due to its dependency on radio signal transmission and line-of-sight (LOS) measurements, GPS suffers from various error sources and poor satellites geometry. To eliminate or mitigate the common errors between receivers, epochs, satellites or stations, the Differential GPS (DGPS) technique is implemented to improve the positioning accuracy to centimeter level. Several strategies were performed to integrate the GPS and INS data to overcome their individual disadvantages and reach superior performance. In this thesis, loosely-coupled integration is introduced which utilizes position or position/velocity measurements from GPS-only filter to aid INS solutions.

The measurement model using GPS position solutions considering the lever arm effect can be written as (Shin, 2005):

$$\delta z_k = \delta r_k^c + (C_b^n l_{GPS}^b \times)\psi_k + v_k \tag{2.76}$$

where,

l_{GPS}^b denotes the lever-arm effect between the GPS antenna and IMU mass center projected in the b-frame;

v_k is the GPS position measurement noise, with the spectral density matrix obtained from statistic and/or kinematic GPS data processing as,

$$R_k = diag([\sigma_\varphi^2 \quad \sigma_\lambda^2 \quad \sigma_h^2]); \tag{2.77}$$

the measurement vector is,

$$\delta \tilde{z}_k = D(\tilde{r}_{INSk}^n - \tilde{r}_{GPSk}^n) + \tilde{C}_b^n l_{GPS}^b; \tag{2.78}$$

$$D = \begin{bmatrix} (M+h) & 0 & 0 \\ 0 & (M+h)\cos\varphi & 0 \\ 0 & 0 & -1 \end{bmatrix} \tag{2.79}$$

where $\tilde{r}_{INSk}^n, \tilde{r}_{GPSk}^n$ denote the position vectors achieved by INS and GPS.

The measurement model using GPS velocity solutions considering the lever arm effect can be written as,

$$\delta z_k = \delta v_k^c - (\omega_{in}^n \times) C_b^n (l_{GPS}^b \times)\psi_k - C_b^n (l_{GPS}^b \times \omega_{ib}^b) \times \psi_k + C_b^n (l_{GPS}^b \times)\delta\omega_{ib}^b + v_k \tag{2.80}$$

where,

v_k is the GPS velocity measurement noise, with the spectral density matrix obtained from statistic and/or kinematic GPS data processing as,

$$R_k = diag([\sigma_{v_N}^2 \quad \sigma_{v_E}^2 \quad \sigma_{v_D}^2]); \tag{2.81}$$

the measurement vector is,

$$\delta z_k = \tilde{v}_{INSk}^n - (\tilde{\omega}_{in}^n \times)\tilde{C}_b^n l_{GPS}^b - \tilde{C}_b^n (l_{GPS}^b \times)\tilde{\omega}_{ib}^b - \tilde{v}_{GPSk}^n; \tag{2.82}$$

where subscripts $\tilde{v}_{INSk}^n, \tilde{v}_{GPSk}^n$ denote the velocity vectors achieved by INS and GPS.

2.4.2 Odometer and Non-Holonomic Constraints

Odometers, or milometers, are applied in land-vehicle navigation and pipeline surveys to provide augmented host velocity observations. The measurement model using odometer velocity measurements considering the misalignment between h-frame and b-frame can be written as (Shin and El-Sheimy, 2005),

$$\delta z_k = C_b^h C_n^b \delta v_k^c - C_b^h C_n^b (v_{INS}^n \times)\psi_k - C_b^h (l_{odometer}^b \times)\delta\omega_{ib}^b + v_k \tag{2.83}$$

where,

C_b^h denotes the DCM from b-frame to h-frame;

$l_{odometer}^b$ denotes the lever arm effect between the odometer and IMU mass center projected in b-frame;

v_{INS}^n is the velocity vector achieved by INS mechanization;

v_k is the odometer measurement noise, with the spectral density matrix evaluated by the priori knowledge on sensor characteristics;

the measurement vector is,

$$\begin{aligned} \delta\tilde{z}_k &= \tilde{C}_b^h \tilde{C}_n^b \tilde{v}_{INSk}^n + \tilde{C}_b^h (\tilde{\omega}_{nb}^b \times) l_{odometer}^b - v_{odometerk}^h \\ &= \tilde{C}_b^h \tilde{C}_n^b \tilde{v}_{INSk}^n + \tilde{C}_b^h (\tilde{\omega}_{nb}^b \times) l_{odometer}^b - [v_{odometerk}^x \quad 0 \quad 0]^T \end{aligned} \quad \textbf{(2.84)}$$

where,

$v_{odometer}^h$ denotes the velocity vector observed by odometer projected to host-frame;

$v_{odometer}^x$ denotes the odometer observation along the forward direction in h-frame.

Non-holonomic constraints is defined as the fact that unless the vehicle jumps off the ground or slides on the ground, the velocity of the vehicle in the plane perpendicular to the forward direction is almost zero, as in Eq. (2.85) (Sukkarieh, 2000; Nassar et al., 2006; Godha, 2006). This is illustrated as in Figure 2.5.

$$\delta\tilde{v}_k^y \approx 0; \delta\tilde{v}_k^z \approx 0 \quad \textbf{(2.85)}$$

where the superscripts y, z denote the transversal and down directions in h-frame.

Simplified from Eq. (2.83), the measurement model using non-holonomic constraints can be written as,

$$\delta z_k = \begin{bmatrix} \delta z_k^y \\ \delta z_k^z \end{bmatrix} = (C_b^h C_n^b)_{2:3,3:3} \delta v_k^c - [C_b^h C_n^b (v_{INS}^n \times)]_{2:3,3:3} \psi_k + v_k \quad \textbf{(2.86)}$$

where,

the subscript $2:3,3:3$ denotes the last two rows' elements of a 3×3 matrix;

v_k is the assumed non-holonomic constraints noise;

the measurement vector is,

$$\delta z_k = (\tilde{C}_b^h \tilde{C}_n^b)_{2:3,3::3} \begin{bmatrix} v_{INS}^y \\ v_{INS}^z \end{bmatrix} \tag{2.87}$$

where v_{INS}^y, v_{INS}^z are the velocities achieved by INS in east and down directions.

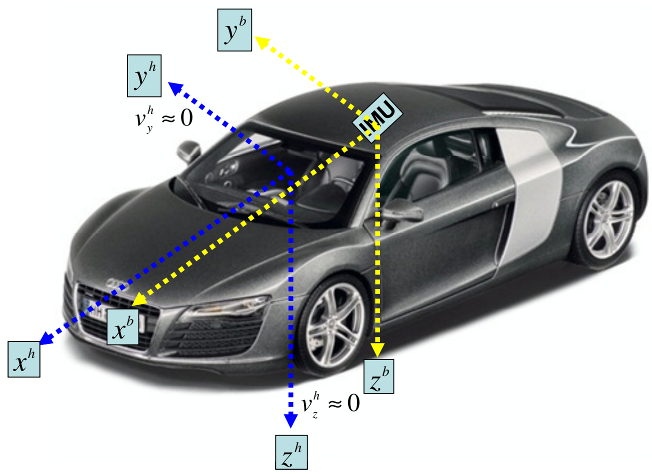

Figure 2.5 Non-holonomic Constraints

2.4.3 Zero-Velocity Updates (ZUPTs) and Coordinate Updates (CUPTs)

ZUPTs are applied at time intervals when the host vehicle is stopped occasionally or intentionally to restrict the position error accumulation rate and the roll, pitch errors (El-Sheimy, 2007). The simplified ZUPT measurement model can be built as,

$$\delta z_k = \delta v_k^c + v_k \tag{2.88}$$

where,

v_k is the assumed ZUPT noise;

the measurement vector is,

$$\delta\tilde{z}_k = \tilde{v}^n_{INS} \tag{2.89}$$

CUPTs are applied when the host vehicle reaches the control stations where the local geodetic coordinates are obtained in advance using high accuracy surveying tools, e.g. DGPS (El-Sheimy, 2007). The simplified CUPT measurement model can be built as,

$$\delta\tilde{z}_k = \delta r^c_k + v_k \tag{2.90}$$

where,

v_k is the assumed CUPT noise;

the measurement vector is,

$$\delta\tilde{z}_i = D(\tilde{r}^n_{INSi} - \tilde{r}^n_{CUPTi}) \tag{2.91}$$

where $\tilde{r}^n_{INSi}, \tilde{r}^n_{CUPTi}$ denote the position vectors achieved by INS and CUPT at the $i-th$ station.

Chapter Three: OPTIMAL ESTIMATION TECHNIQUES IN NAVIGATION

3.1 Overview of Filtering and Smoothing

Estimation is a data processing technique that applies the predefined statistical criterion to extract the desired information from the available resources (Gelb, 1974). Generally speaking, the objective of optimal estimation in navigation systems is to obtain the “best” estimates of the system states, including navigation parameters, inertial sensor errors, and other related parameters in the augmentation sensors. The “best” in this case means the Minimum Mean-Square Error (MMSE), which is the commonly used mathematical criterion in statistical sense (Brown and Hwang, 1997). To achieve the best performance, the navigation estimator utilizes all the available information: the sensor measurement data, the knowledge of system dynamics and measurement mechanizations, the noise statistics, and the initial conditions (Gao, 2007).

Based on the desired estimation time (t) and the availability of measurements, estimation problems could be divided into three categories (El-Sheimy, 2007):
Prediction, when (t) occurs after the last available measurement point;
Filtering, when (t) coincides with the last available measurement point;
Smoothing, when (t) falls within the span of available measurement data.
The three types of estimation problems are depicted in Figure 3.1.

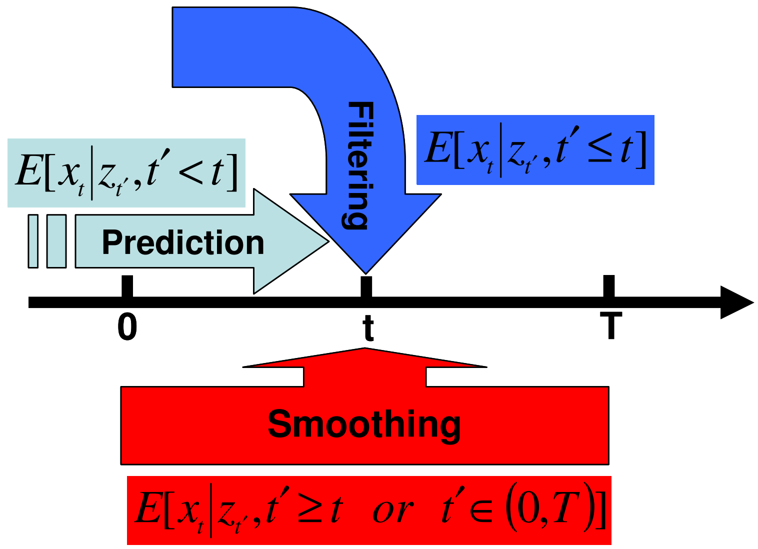

Figure 3.1 Prediction, Filtering and Smoothing

Literally understanding, the function of a filter is to separate the desired signal from the raw data with random noise and deterministic interference. This usually refers to passing signals in a specified frequency range and rejecting those outside that range in the applications of communications, controls, and electrics. This concept had not been challenged until Wiener proposed several meaningful assumptions: suppose the desired signal is not a deterministic process but a stochastic process similar to the characteristic of noise; suppose both the signal and noise share a significant overlap in frequency domain (Brown and Hwang, 1997). The Wiener Filter (Wiener, 1949) was published and researched afterwards to solve these problems by applying the MMSE criterion with the known spectral properties of the original signal and noise. However, it was limited to statistically stationary processes and provided estimation only in steady-state regime (Gelb, 1974); on the other hand, the filter must be physically realizable. The limitations of Wiener Filter restricted its propagation in engineering fields regardless of its success in image processing (Acharya and Ray, 2005).

In 1960, R.E.Kalman offered an alternative explanation of Wiener Filter with state-space and time domain formulations. Beginning with the trajectory estimation problem introduced by Schmidt (Grewal and Andrew, 2001), Kalman Filter (KF) was unexpectedly applied in a wide variety of researching and industrial areas. KF is recognized as the classical estimation tool in the applications of control, navigation, and multi-sensor fusion. Further, it is credited as one of the most suitable estimators to be implemented by modern digital techniques.

Although the research of smoothing actually predated the KF, it was the KF that made smoothing algorithms applicable in navigation field. Smoothing problems were classified into three categories by Meditch (1969): fixed-point, fixed-interval, and fixed-lag smoothers. As depicted in Figure 3.2, suppose t_0, t_T are the initial and final points in a time interval; t is the desired estimate time; Δ is the length of a sliding time window. In fix-point smoothing, the optimal estimate $\hat{x}_t$ is obtained by using all the future measurements after the fixed estimation time t as t_T increases; in fix-interval smoothing, $\hat{x}_t$ is obtained by using all the past, current and future measurements in the fixed time interval $[t_0, t_T]$ as t varies between t_0 and t_T; in fix-lag smoothing, $\hat{x}_t$ is obtained by all the future measurements in the fixed time window Δ as t_T increases (t equals to $t_T - \Delta$). While fixed-point and fixed-lag smoothing could be regarded as near real time estimation methods, fixed-interval smoothing can only be implemented in post missions. Fixed-interval smoothing has been used in most surveying applications, because surveying is typically amenable to post-processing where best position information is pursued for all measured points (Shin and El-Sheimy, 2002). The details about fixed-point and fixed-lag smoothing are introduced in Nassar (2003), Gelb (1974), and Crassidis and Junkins (2004). Due to the nature of the analyzed INS-based applications in this thesis, only fixed-interval smoothing algorithms will be discussed in details.

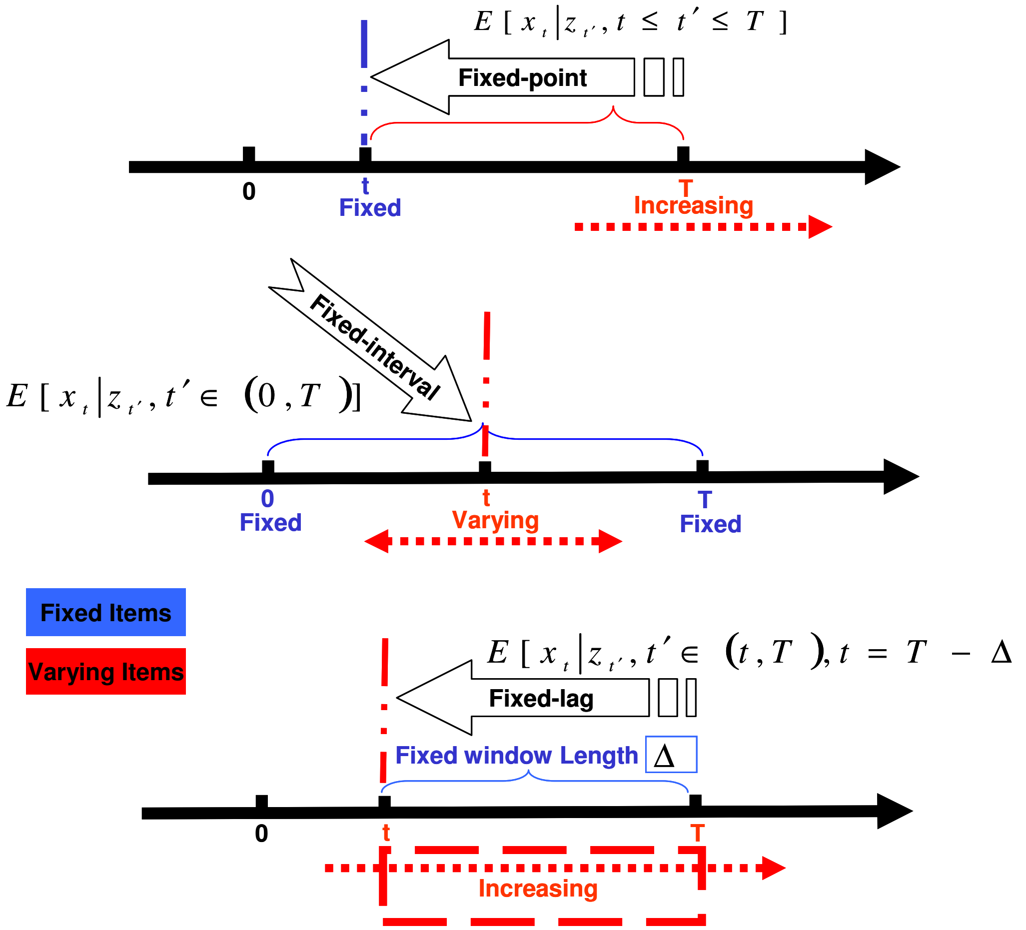

Figure 3.2 Fixed-point, Fixed-lag and Fixed-interval Smoothing

3.2 Kalman Filter (KF)

KFs are based on the linear dynamics systems in time domain. A typical state-space representation of the linear system requires building the system dynamics model, and the observation relationship between the measurement quantities and the system states. This requirement can be described as the continuous-time system equation and the discrete-time measurement equation, as shown in Eq. (3.1) and (3.2) respectively.

$$\dot{x}(t) = F(t)x(t) + G(t)w(t) \tag{3.1}$$

$$z_k = H_k x_k + v_k \tag{3.2}$$

where,

t indicates the continuous time; the subscript k represents the discrete time epoch t_k ;

x is the system state vector; z is the measurement vector;

w is the system noise vector, assumed to be a Gaussian white noise with the covariance matrix, $E[w(t)w(\tau)^T] = Q(t)\delta(t-\tau)$, where the operator $\delta(\cdot)$ denotes the Dirac delta function and Q is called the spectral density matrix (Gelb, 1974);

v is the measurement white noise vector;

F is the system dynamics matrix; G is the system noise shaping matrix;

H is the observation design matrix.

Eq. (3.1) is preferred to be transformed to a discrete-time form for digital implementation:

$$x_k = \Phi_{k,k-1} x_{k-1} + w_{k-1} \tag{3.3}$$

where,

$w_{k-1} = \int_{k-1}^{k} \Phi_{k,\tau} G(\tau) w(\tau) d\tau$ is the driven response at t_k due to the presence of the input white noise during the time interval (t_{k-1}, t_k) (Brown and Hwang, 1997);

$\Phi_{k,k-1}$ is the system transition matrix from epoch t_{k-1} to t_k;

the subscript $k-1$ represents the time epoch t_{k-1}.

For most system models in reality, the dynamics matrix $F(t)$ is considered to be time invariant during the small time interval $\Delta t = t_k - t_{k-1}$. Thus, the transition matrix can be obtained from the dynamics matrix by simple numerical approximation as (Gao, 2007),

$$\Phi_{k,k-1} = \mathscr{L}^{-1}[(sI - F)^{-1}] = e^{F\Delta t} \approx I + F\Delta t \quad \textbf{(3.4)}$$

Because a white sequence is a sequence of zero-mean random variable that is uncorrelated timewise, the covariance matrix associated with w_k and v_k is given by (Brown and Hwang, 1997),

$$E[w_k w_i^T] = \begin{cases} Q_k, & i = k \\ 0, & i \neq k \end{cases} \quad \textbf{(3.5)}$$

$$E[v_k v_i^T] = \begin{cases} R_k, & i = k \\ 0, & i \neq k \end{cases} \quad \textbf{(3.6)}$$

$$E[w_k v_i^T] = 0 \quad \forall i, k \quad \textbf{(3.7)}$$

where the process noise matrix is derived as,

$$
\begin{aligned}
Q_k &= E[w_k w_k{}^T] = E\left\{\left[\int_k^{k+1} \Phi_{k+1,\xi} G(\xi) w(\xi) d\xi\right]\left[\int_k^{k+1} \Phi_{k+1,\eta} G(\eta) w(\eta) d\eta\right]^T\right\} \\
&= \int_k^{k+1}\int_k^{k+1} \Phi_{k+1,\xi} G(\xi) E[w(\xi) w^T(\eta)] G^T(\eta) \Phi^T{}_{k+1,\eta} d\xi d\eta \\
&\approx \frac{1}{2}[\Phi_k G(t_k) Q(t_k) G^T(t_k) \Phi_k^T + G(t_{k+1}) Q(t_{k+1}) G^T(t_{k+1})] \Delta t_{k+1}
\end{aligned} \tag{3.8}
$$

The determination of the initial state estimate $\hat{x}_0$ and its covariance $P_0 = E\left[\hat{x}_0 \hat{x}_0^T\right]$ is the first step of the KF. With a priori information of both the noise characteristics and the initial conditions, the KF algorithm can be implemented recursively using a series of prediction and measurement update steps (Gelb, 1974).

The KF prediction stage is built on the system model as,

$$\hat{x}_k^- = \Phi_{k,k-1} \hat{x}_{k-1}^+ \tag{3.9}$$

$$P_k^- = \Phi_{k,k-1} P_k^+ \Phi_{k,k-1} + Q_{k-1} \tag{3.10}$$

where,

$\hat{x}^-$ denotes the prediction state estimate; $\hat{x}^+$ denotes the update state estimate;

P^- denotes the prediction covariance matrix; P^+ denotes the update covariance matrix.

In the measurement update stage, the optimal state estimate and its covariance are updated with the predictions and the observations. This group of equations is listed as follows,

$$K_k = P_k^- H_k^T (H_k P_k^- H_k^T + R_k)^{-1} \tag{3.11}$$

$$v_k = z_k - H_k \hat{x}_k^- \quad \textbf{(3.12)}$$

$$\hat{x}_k^+ = \hat{x}_k^- + K_k v_k \quad \textbf{(3.13)}$$

$$P_k^+ = (I - K_k H_k) P_k^- \quad \textbf{(3.14)}$$

where,

v_k is the innovation sequence, which denotes the difference between the observation and the prediction.

K_k is the KF gain, or the weighting matrix, which decides how much of the new information contained in the innovations should be accepted by the system (Petovello, 2003). The derivation of the gain matrix is based on the minimum variance criterion.

The KF algorithm is summarized in Figure 3.3.

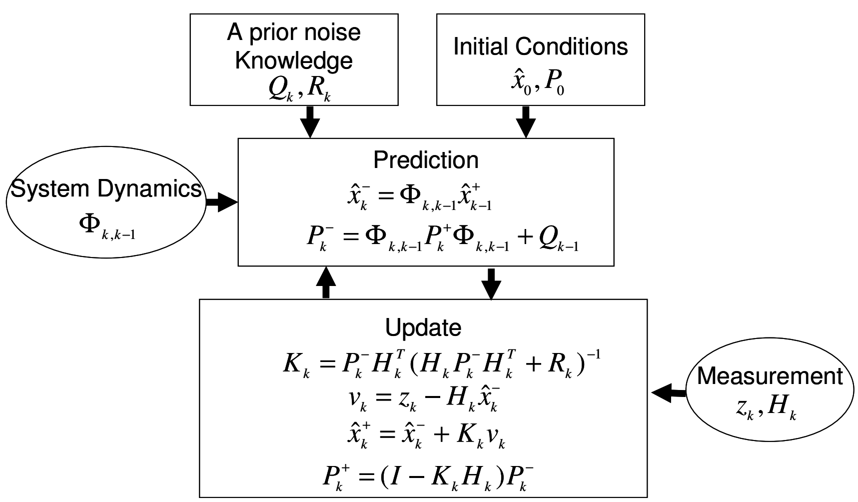

Figure 3.3 Kalman Filter

3.2.1 Extended Kalman Filter (EKF)

The aforementioned mathematical models are assumed to be linear. Unfortunately, they are non-linear in most of the navigation applications. The typical discrete-time non-linear system model and measurement model are illustrated in the following equations (Grewal and Andrew, 2001),

$$x_k = f(x_{k-1}, k-1) + w_{k-1} \tag{3.15}$$

$$z_k = h(x_k, k) + v_k \tag{3.16}$$

where $f(\cdot), h(\cdot)$ are the non-linear functions describing the system dynamics behavior and the measurement mechanization respectively.

The principle method to deal with the non-linear estimation problems is to linearize the models about a predetermined or instantaneous nominal trajectory. This nominal trajectory is defined as the trace of a time-varying parameter vector, which is typically the sequence of the system state vectors with the expected or estimated values (Grewal and Andrew, 2001). By using Taylor series expansion, the linearization process of the non-linear system model is listed as,

$$x_k^{NOM} = f(x_{k-1}^{NOM}, k-1) \tag{3.17}$$

$$x_k = x_k^{NOM} + \delta x_k \tag{3.18}$$

$$
\begin{aligned}
x_k &= f(x_{k-1}, k-1) + w_{k-1} \approx f(x_{k-1}^{NOM}, k-1) + \left.\frac{\partial f(x(t),t)}{\partial x}\right|_{x=x_{k-1}^{NOM},\ t=k-1} (x_{k-1} - x_{k-1}^{NOM}) + w_{k-1} \\
&= x_k^{NOM} + \left.\frac{\partial f(x(t),t)}{\partial x}\right|_{x=x_{k-1}^{NOM},\ t=k-1} (x_{k-1} - x_{k-1}^{NOM}) + w_{k-1}
\end{aligned}
\tag{3.19}
$$

or,

$$
\begin{aligned}
\delta x_k &= \left.\frac{\partial f(x(t),t)}{\partial x}\right|_{x=x_{k-1}^{NOM},\ t=k} \delta x_{k-1} + w_{k-1} \\
&= F_{k-1}\delta x_{k-1} + w_{k-1}
\end{aligned}
\tag{3.20}
$$

where,

x^{NOM} denotes the nominal trajectory;

δx is the system state perturbation from the nominal trajectory, which is also called "error state";

$f(x(t),t)$ is the continuous non-linear function;

F_{k-1} is the linearized system dynamics matrix, corresponding to the system transition matrix $\Phi_{k,k-1}$ in the linear case.

Similarly, the linearization of the measurement model is written as,

$$
\begin{aligned}
z_k &= h(x_k, k) + v_k \approx h(x_k^{NOM}, k) + \left.\frac{\partial h(x(t),t)}{\partial x}\right|_{x=x_k^{NOM},\ t=k} (x_k - x_k^{NOM}) + v_k \\
&= z_k^{NOM} + \left.\frac{\partial h(x(t),t)}{\partial x}\right|_{x=x_k^{NOM},\ t=k} (x_k - x_k^{NOM}) + v_k
\end{aligned}
\tag{3.21}
$$

or,

$$
\begin{aligned}
\delta z_k &= z_k - h(x_k^{NOM}, k) \\
&= \left.\frac{\partial h(x(t),t)}{\partial x}\right|_{x=x_k^{NOM},\ t=k} \delta x_k + v_k \\
&= H_k \delta x_k + v_k
\end{aligned}
\tag{3.22}
$$

where,

δz is the measurement perturbation from the nominal trajectory, which is also called "measurement closure" between actual and predicted measurements;

H_k is the linearized observation design matrix.

The combination of Eq. (3.20) and (3.22) reconstructs the linear system model and measurement model. As a result, the implementation of KF on this group of models achieves the optimal estimates of the error states. Lastly, the original system state is obtained by Eq. (3.18), which is called state "reset". If this reset stage is executed in closed loop after each KF measurement update step, or in other words, if the feedback on the nominal trajectory exists, the nominal trajectory trusts the estimation results and varies according to them. Afterwards, this error state will be set as "zero" to indicate the nominal value is the same as the estimation. This approach is named as Extended Kalman Filter (EKF). On the other hand, if the reset stage is executed in open loop, or in other words, if only the feedforward on the KF estimates exists, the nominal trajectory is determined beforehand and ignores the filter estimates. In this case, it is called Linearized Kalman Filter (LKF) (Nassar, et al., 2005; Shin, 2005). A description of the relationship between the filtering results and the nominal trajectory for LKF and EKF are shown in Figure 3.4 and Figure 3.5 respectively. It tells us that while the LKF nominal trajectory is independent of the filtering estimation results, the EKF nominal trajectory follows them if the feedback rate is the same as the measurement update rate.

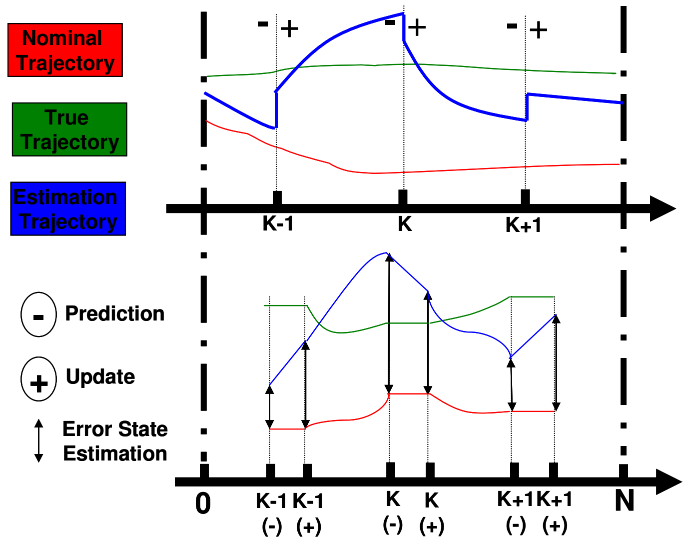

Figure 3.4. Relationship between Filtering Results and LKF Nominal Trajectory

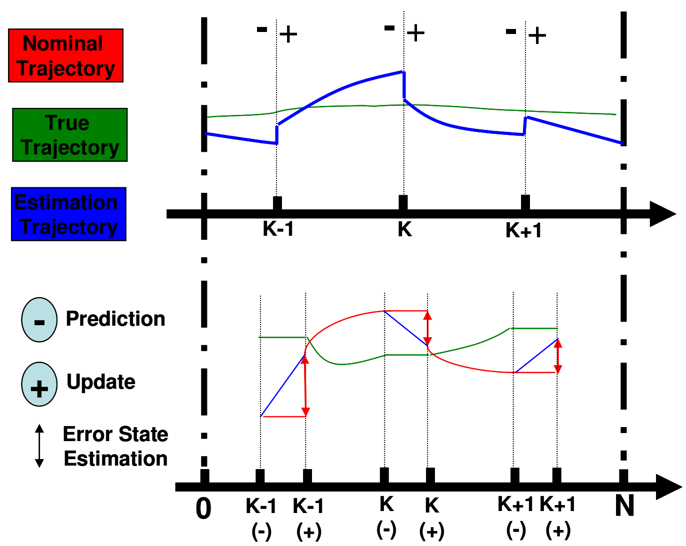

Figure 3.5 Relationship between Filtering Results and EKF Nominal Trajectory

3.2.2 EKF for Aided Inertial Navigation Systems

In aided INS, the INS error model is derived to represent the dynamics of navigation error states by applying the perturbation analysis. The reference values used in the perturbations are essentially the values of the nominal trajectory, about which the original INS mechanization equations are linearized. Moreover, while the determinant parts of the sensor parameters are calibrated in advance, the random sensor errors are modeled by linear stochastic processes. Eq. (3.23)-(3.25) describe the definitions of the system state x, the nominal state x^{NOM}, and the corresponding error state δx as follows:

$$x = [(r)^T, (v)^T, (q_b^n)^T, (b_g)^T, (b_{acc})^T, (SF_g)^T, (SF_{acc})^T]^T \tag{3.23}$$

$$x^{NOM} = [(r^{NOM})^T, (v^{NOM})^T, (q_b^{nNOM})^T, (b_g^0)^T, (b_{acc}^0)^T, (SF_g^0)^T, (SF_{acc}^0)^T]^T \tag{3.24}$$

$$\delta x = [(\delta r)^T, (\delta v)^T, \psi^T, (\delta b_g)^T, (\delta b_{acc})^T, (\delta SF_g)^T, (\delta SF_{acc})^T]^T \tag{3.25}$$

where b^0, SF^0 denote the determinant bias and scale factors; the representations of other denotations refers to Section 2.3.4.

The relationship between the states above is given by:

$$x = x^{NOM} - \delta x \tag{3.26}$$

where the attitude parameter correction is specifically processed by the quaternion production rule as in Shin (2005):

$$q_b^n = q_p^n \bullet q_b^p = q_p^n \bullet q_b^{nNOM} \tag{3.27}$$

$$q_p^n = \begin{bmatrix} \frac{\sin\|0.5\phi\|}{\|\phi\|}\phi \\ \cos\|0.5\phi\| \end{bmatrix} \quad \textbf{(3.28)}$$

$$\phi = \hat{\psi} + \delta\theta \quad \textbf{(3.29)}$$

$$\delta\theta = \begin{bmatrix} \delta r_E/(N+h) \\ -\delta r_N/(M+h) \\ -\delta r_E \tan\varphi/(N+h) \end{bmatrix} \quad \textbf{(3.30)}$$

where $\delta\theta, \phi, \psi$ are the rotation vectors referred to Section 2.2.

Referring to Section 3.2.1, the corresponding δz_k in Eq. (3.22) denotes the measurement difference between INS solutions and GPS observations at time epoch t_k as,

$$\delta\tilde{z}_k = \tilde{z}_k^{INS} - \tilde{z}_k^{GPS} \quad \textbf{(3.31)}$$

The corresponding system transition matrix and observation design matrix F_{k-1}, H_k in Eq. (3.20) and (3.22) are derived from the non-linear INS mechanization and measurement relationship f_{INS}, h as,

$$F_{k-1} = \left.\frac{\partial f_{INS}}{\partial x}\right| x = \hat{x}_k^{-NOM}, t = k \quad \textbf{(3.32)}$$

$$H_k = \left.\frac{\partial h}{\partial x}\right| x = \hat{x}_k^{-NOM}, t = k \quad \textbf{(3.33)}$$

where the details of F_{k-1} refers to Eq. (2.68)-(2.74); H_k refers to Section 2.4;

$\hat{x}_k^{-NOM}$ denotes the predicted value of the nominal trajectory at epoch t_k, which equals to one step INS mechanization solution from the updated nominal value $\hat{x}_{k-1}^{+\ NOM}$ as,

$$\hat{x}_k^{-NOM} = f_{INS}(\hat{x}_{k-1}^{+\ NOM}) \tag{3.34}$$

The group of KF prediction and update equations are recursively processed to achieve the optimal estimates of the error state as in Eq. (3.9)-(3.14).

In EKF, the error state correction in Eq. (3.26)-(3.30) is applied not only on the system output as a feedforward loop, but also on the nominal trajectory as a feedback loop after a full KF step. In addition, the updated error state will be reset as "zero" to indicate the nominal value is the same as the updated estimation. In this case, the nominal trajectory trusts the filtering estimation results and varies accordingly. The error state feedforward and feedback loops are described respectively as,

$$\hat{x}_k^{+} = \hat{x}_k^{-NOM} - \delta\hat{x}_k^{+} \tag{3.35}$$

$$\hat{x}_k^{+NOM} = \hat{x}_k^{-NOM} - \delta\hat{x}_k^{+} = \hat{x}_k^{+}; \delta\hat{x}_k^{+} \equiv 0 \tag{3.36}$$

where $\equiv$ denotes the error state reset.

Eq. (3.36) reformulats the succeeding KF loop as,

$$\hat{x}_{k+1}^{-\ NOM} = f_{INS}(\hat{x}_k^{+NOM}) = f_{INS}(\hat{x}_k^{+}) \tag{3.37}$$

$$\delta\hat{x}_{k+1}^{-} = F_{k-1}\delta\hat{x}_k^{+} = 0 \tag{3.38}$$

$$\hat{x}_{k+1}^{-} = \hat{x}_{k+1}^{-\ NOM} - \delta\hat{x}_{k+1}^{-} = \hat{x}_{k+1}^{-\ NOM} \quad \textbf{(3.39)}$$

$$\delta\hat{x}_{k+1}^{+} = \delta\hat{x}_{k+1}^{-} + K_{k+1}[\delta z_{k+1} - H_{k+1}\delta\hat{x}_{k+1}^{-}] = K_{k+1}\delta z_{k+1} \quad \textbf{(3.40)}$$

$$\hat{x}_{k+1}^{+} = \hat{x}_{k+1}^{-\ NOM} - \delta\hat{x}_{k+1}^{+} = \hat{x}_{k+1}^{-\ NOM} - K_{k+1}\delta z_{k+1} = \hat{x}_{k+1}^{-} - \delta\hat{x}_{k+1}^{+} \quad \textbf{(3.41)}$$

where Eq. (3.37) indicate that the nominal trajectory is determined by the Kalman Filter estimate.

The algorithm structure of EKF for INS-based integration is illustrated in Figure 3.6.

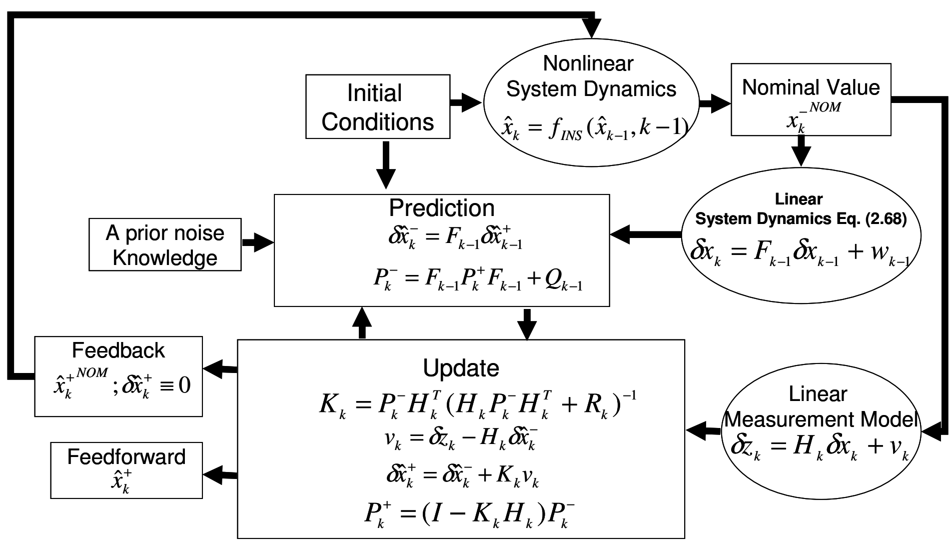

Figure 3.6 EKF Structure for INS-based Integration (After Liu et. al., 2009)

3.3 Fixed-Interval Smoothing

As discussed in Section 3.1, the fundamental idea of the fixed-interval smoothing is to obtain the optimal estimate at the current time by utilizing all the available measurements within the fixed time interval (Gelb, 1974). This concept can be intuitively performed by combining two Kalman filters, including one Forward Kalman Filter (FKF) and one Backward Kalman Filter (BKF). As depicted in Figure 3.7, while the FKF obtains its estimate with all the measurements up to the current time epoch t_k, the BKF optimally estimates the states by incorporating the measurements after t_k within the assumed time interval. Further, since the BKF is implemented reversely with time, the BKF prediction results $\hat{x}_{Bk}^-$ does not assimilate the measurement z_k, which has already been used by the FKF update $\hat{x}_{Fk}^+$. These two estimates are uncorrelated since no common data are used (Jansson, 1998). At the final step, both the solutions from the two filters will be combined in the following equations, of which the overall derivation refers to Gelb (1974), Crassidis and Junkins (2004).

$$\hat{x}_{Sk} = P_{Sk}({P_{Fk}^{+}}^{-1}\hat{x}_{Fk}^{+} + {P_{Bk}^{-}}^{-1}\hat{x}_{Bk}^{-}) \tag{3.42}$$

$$P_{Sk} = ({P_{Fk}^{+}}^{-1} + {P_{Bk}^{-}}^{-1})^{-1} \tag{3.43}$$

where the subscript Sk, Fk, Bk denote the smoothing, forward filtering, and backward filtering results at the time epoch t_k respectively.

Eq. (3.43) obviously indicates that the smoothing covariance is smaller than either filter covariance. As a result, it implies that the smoothed estimate, if not more accurate, could never be worse than the individual filter estimate (Brown and Hwang, 1997). Furthermore, since the smoothing algorithm depends on both of the two filters, accurate filtering is prerequisite to accurate smoothing (Gelb, 1974).

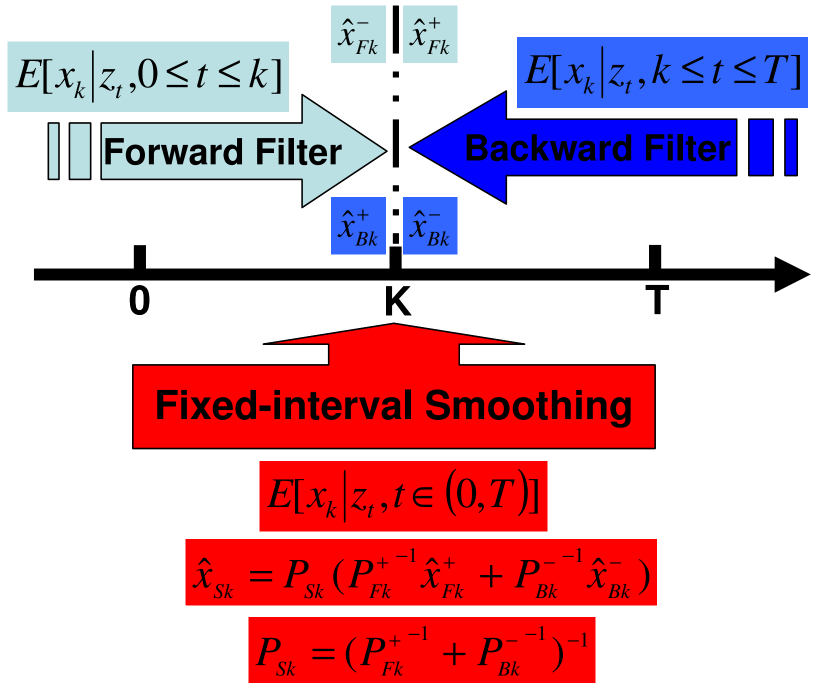

Figure 3.7 FKF, BKF and Smoothing

Mayne (1966) and Fraser (1967) derived different formulations of smoothing solutions by using the Maximum Likelihood (ML) principle. A simplified derivation and interpretation was published by Fraser and Potter (1969) regarding the optimum smoother as the combination of two optimum linear filter estimates. The discrete-time formulations of the Two Filter Smoother (TFS) are summarized in details in Crassidis and Junkins (2004), and Maybeck (1994).

On the other hand, earlier work yielded the fixed-interval smoother estimate as a correction to the KF estimate. Rauch-Tung-Striebel Smoother (Rauch et al., 1965) or RTSS derived by ML criterion has maintained its popularity since the initial paper (Crassidis and Junkins, 2004). To avoid the covariance matrix inversion required by RTSS, the smoothers by Bryson and Frazier (1962), Bierman (1973), expressed the correction term with the adjoint or costate variable which included the measurements by introducing the variational calculus to the smoothing problem. However, the application of Bryson and Frazier smoother is limited due to its numerical instability for long duration estimation (Mayne, 1966).

Most of the smoothers mentioned above were designed for linear dynamic systems. Therefore, they were not applicable for INS-based multi-sensor systems because of the high nonlinear characteristics of the INS navigation equations. The further attempt of applying the common EKF both forward and backward failed to accurately estimate the smoothing INS error states. This problem was resolved by a revised algorithm that was proposed specifically for pipeline surveys using IMUs (Yu et al., 2005). In this thesis, the schemes of two fixed-interval smoothers will be described in details for INS-based integration systems, i.e. TFS and RTSS. Further, the considerations related to optimal smoothing will be discussed.

3.3.1 Two-Filter Smoother (TFS)

As discussed above, TFS can be accomplished from a combination of two KFs manipulated forward and backward, i.e. FKF and BKF. The forward filter is the conventional EKF as in Section 3.2.2, which starts from a priori initial conditions determined by the INS initial alignment:

$$\begin{aligned} \delta x_{F0}^{+} &= 0 \\ P_{F0}^{+} &= E[\delta x_{F0}^{+} \delta x_{F0}^{+\,T}] \end{aligned} \qquad \textbf{(3.44)}$$

where the subscript 0 denotes the starting time epoch.

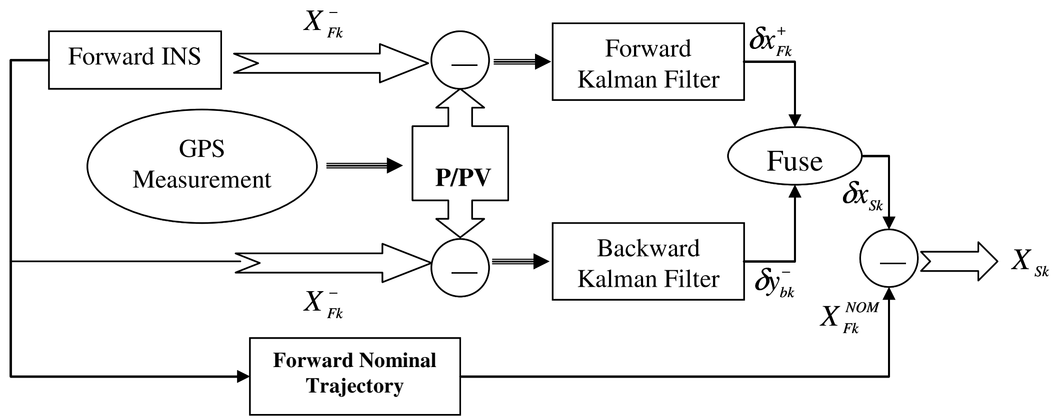

Figure 3.8 TFS Structure (INS/GPS) (After Liu et. al., 2009)

A completely independent backward filter is a choice for TFS, in which the backward INS mechanization is programmed to provide the INS solutions for both the backward nominal trajectory and the backward measurement updates. However, this encounters difficulty to implement backward initialization, as the unpredictable ending conditions of the test time interval cannot assure the serious requirement of statistic backward INS initial alignment. Conversely, the implementation of BKF without a backward INS mechanization relies on the stored FKF results. More specifically, the nominal trajectory and the measurements of BKF copy their counterparts of FKF. The TFS algorithm structure is illustrated in Figure 3.8. The details about BKF and its combination with the FKF in the TFS algorithm are introduced in discrete-time form as follows:

New Variable Definition and Initialization

In order to avoid the undesirable matrix inversions and to provide a valid boundary initialization, the following new variables in BKF are defined to replace the original error state and its covariance matrix (Crassidis and Junkins, 2004):

$$M_B = P_B^{-1} \quad \textbf{(3.45)}$$

$$\delta y_B = P_B^{-1}\delta x = M_B \delta x_B \quad \textbf{(3.46)}$$

where M_B is the covariance matrix inversion.

The smoothing is initialized using the FKF results at the final epoch t_N as,

$$\delta x_{SN} = \delta x_{FN}^{+} \quad \textbf{(3.47)}$$

$$P_{SN} = P_{FN}^{+} \quad \textbf{(3.48)}$$

which leads the BKF initialization derived by Eq. (3.42)-(3.43) as,

$$P_{SN} = (P_{FN}^{+\,-1} + P_{BN}^{-\,-1})^{-1} \quad \textbf{(3.49)}$$

$$M_{BN} = P_{BN}^{-\,-1} = P_{SN}^{-1} - P_{FN}^{+\,-1} = 0 \quad \textbf{(3.50)}$$

$$P_{BN}^{-} = \infty \quad \textbf{(3.51)}$$

$$\delta\hat{x}_{SN} = P_{SN}(P_{FN}^{+\,-1}\delta\hat{x}_{FN}^{+} + P_{BN}^{-\,-1}\delta\hat{x}_{BN}^{-}) \quad \textbf{(3.52)}$$

$$\delta\hat{y}_{BN}^{-} = P_{BN}^{-\,-1}\delta\hat{x}_{BN}^{-} = P_{SN}^{-1}\delta\hat{x}_{SN} - P_{FN}^{+\,-1}\delta\hat{x}_{FN}^{+} = 0 \quad \textbf{(3.53)}$$

where Eq. (3.51) and (3.53) indicate that the BKF initial error state is finite but uncertain. This is necessary since the two estimates from FKF and BKF are required to be uncorrelated (Jansson, 1998).

BKF Models

The backward INS error model as required by the BKF, which represents the inverse dynamic process of the system error states from the current time epoch t_k to the previous epoch t_{k-1}, is simply obtained by inversing the dynamics matrix from Eq. (3.20). The BKF system model as well as the measurement model can be written by,

$$\delta x_{Bk-1} = F_{k-1}^{-1} \delta x_{Bk} + F_{k-1}^{-1} w_k \tag{3.54}$$

$$\delta z_{k-1} = H_{k-1} \delta x_{Bk-1} + v_{k-1} \tag{3.55}$$

$$\delta \tilde{z}_{k-1} = \tilde{z}_{k-1}^{INS} - \tilde{z}_{k-1}^{GPS} \tag{3.56}$$

where $\tilde{z}_{k-1}^{INS}$ remain as the same INS solutions in FKF; the backward system dynamics matrix and observation design matrix are linearized about the FKF prediction results as,

$$F_{k-1} = \left. \frac{\partial f_{INS}}{\partial x} \right| x = \hat{x}_{Fk}^{-}, t = k \tag{3.57}$$

$$H_{k-1} = \left. \frac{\partial h}{\partial x} \right| x = \hat{x}_{Fk-1}^{-}, t = k-1 \tag{3.58),}$$

The equations above suggest that the backward nominal trajectory is predetermined as the sequence of FKF predictions, i.e.:

$$\hat{x}_{Bk}^{-} = \hat{x}_{Bk}^{-\ NOM} - \delta\hat{x}_{Bk}^{-} = \hat{x}_{Fk}^{-} - \delta\hat{x}_{Bk}^{-} \quad \textbf{(3.59)}$$

BKF Prediction

Referring to Maybeck (1994), the discrete-time form BKF prediction equations are derived with the new defined variables. From Eq. (3.54), since $\hat{\delta x}_{Bk}$ and w_k are uncorrelated, the BKF prediction covariance is derived as,

$$\begin{aligned} P_{Bk-1}^{-} &= E\left[\delta\tilde{x}_{Bk-1}^{-}\delta\tilde{x}_{Bk-1}^{-\ T}\right] = E[(F_{k-1}^{-1}\delta\tilde{x}_{Bk}^{+} + F_{k-1}^{-1}w_k)(F_{k-1}^{-1}\delta\tilde{x}_{Bk}^{+} + F_{k-1}^{-1}w_k)^T] \\ &= E[F_{k-1}^{-1}(\delta\tilde{x}_{Bk}^{+}\delta\tilde{x}_{Bk}^{+\ T} + 2\delta\tilde{x}_{Bk}^{+}w_k^T + w_k w_k^T)F_{k-1}^{-1\ T}] \\ &= F_{k-1}^{-1}\{E[\delta\tilde{x}_{Bk}^{+}\delta\tilde{x}_{Bk}^{+\ T}] + 2E[\delta\tilde{x}_{Bk}^{+}w_k^T] + E[w_k w_k^T]\}F_{k-1}^{-1\ T} \\ &= F_{k-1}^{-1}(P_{Bk}^{+} + Q)F_{k-1}^{-1\ T} \end{aligned} \quad \textbf{(3.60)}$$

where,

$$\delta\tilde{x}_{Bk-1}^{-} = \delta\hat{x}_{Bk-1}^{-} - \delta x_{k-1}; \delta\tilde{x}_{Bk}^{+} = \delta\hat{x}_{Bk}^{+} - \delta x_k \quad \textbf{(3.61)}$$

To apply the definition of the new variables, the Sherman-Morrison-Woodbury Matrix Inversion Lemma shown as follows is used (See proof in Goluband Van Loan, 1996; Crassidis and Junkins, 2004):

Let,

$$F = [A + BCD]^{-1} \quad \textbf{(3.62)}$$

where A, B, C, D are arbitrary $n \times n$ non-singular matrix. Then,

$$F = A^{-1} - A^{-1}B(DA^{-1}B + C^{-1})^{-1}DA^{-1} \quad \textbf{(3.63)}$$

With $A = P_{Bk}^{+}; B = I; C = Q; D = I$, the prediction covariance inversion is yielded as:

$$M_{Bk-1}^{-} = F_{k-1}^{T}(I - K_{Bk-1}^{-})M_{Bk}^{+}F_{k-1} \tag{3.64}$$

$$K_{Bk-1}^{-} = M_{Bk}^{+}Q(M_{Bk}^{+}Q + I)^{-1} \tag{3.65}$$

where K_{Bk-1}^{-} is the BKF prediction gain.

Using these equations, the desired form for the predicted error state is derived as,

$$\begin{aligned}
\delta\hat{y}_{Bk-1}^{-} &= M_{Bk-1}^{-}\delta\hat{x}_{Bk-1}^{-} = M_{Bk-1}^{-}(F_{k-1}^{-1}\delta\hat{x}_{Bk}^{+}) = M_{Bk-1}^{-}F_{k-1}^{-1}(P_{Bk}^{+}\delta\hat{y}_{Bk}^{+}) \\
&= F_{k-1}^{T}(I - K_{Bk-1}^{-})M_{Bk}^{+}F_{k-1}F_{k-1}^{-1}(P_{Bk}^{+}\delta\hat{y}_{Bk}^{+}) \\
&= F_{k-1}^{T}(I - K_{Bk-1}^{-})M_{Bk}^{+}P_{Bk}^{+}\delta\hat{y}_{Bk}^{+} \\
&= F_{k-1}^{T}(I - K_{Bk-1}^{-})\delta\hat{y}_{Bk}^{+}
\end{aligned} \tag{3.66}$$

BKF Update

The formulations of Information Kalman Filter (IKF) using the new defined variables are introduced for the BKF update equations in order to overcome the potential computational and numerical difficulties for large measurement sets (Crassidis and Junkins, 2004) as follows:

$$M_{Bk}^{+} = M_{Bk}^{-} + H_{k}^{T}R_{k}^{-1}H_{k} \tag{3.67}$$

$$\hat{y}_{Bk}^{+} = \hat{y}_{Bk}^{-} - H_{k}^{T}R^{-1}(\delta z_{k} - H_{k}\hat{x}_{Fk}^{-}) \tag{3.68}$$

The derivation for Eq. (3.68) is introduced as follows. By using Eq. (3.59), the backward error state update is given by,

$$\begin{aligned} \delta\hat{x}^{+}_{Bk} &= \delta\hat{x}^{-}_{Bk} + K^{+}_{Bk}[\delta z_k - H_k \delta\hat{x}^{-}_{Bk}] \\ &= \hat{x}^{-}_{Fk} - \hat{x}^{-}_{Bk} + K^{+}_{Bk}[\delta z_k - H_k(\hat{x}^{-}_{Fk} - \hat{x}^{-}_{Bk})] \end{aligned} \tag{3.69}$$

where K^{+}_{Bk} is the BKF update gain. Eq. (3.69) yields,

$$\begin{aligned} \hat{x}^{-}_{Fk} - \delta\hat{x}^{+}_{Bk} &= \hat{x}^{-}_{Bk} - K^{+}_{Bk}[\delta z_k - H_k(\hat{x}^{-}_{Fk} - \hat{x}^{-}_{Bk})] \\ &= (\hat{x}^{-}_{Bk} - K^{+}_{Bk} H_k \hat{x}^{-}_{Bk}) - K^{+}_{Bk}(\delta z_k - H_k \hat{x}^{-}_{Fk}) \\ &= (I - K^{+}_{Bk} H_k)\hat{x}^{-}_{Bk} - K^{+}_{Bk}(\delta z_k - H_k \hat{x}^{-}_{Fk}) \end{aligned} \tag{3.70}$$

Referring to (Crassidis and Junkins, 2004), the alternative forms for Kalman filter gain K and $I - KH$ are,

$$K^{+}_{Bk} = P^{+}_{BK} H^{T}_{k} R^{-1} \tag{3.71}$$

$$I - K^{+}_{Bk} H_k = P^{+}_{BK} {P^{-}_{BK}}^{-1} = P^{+}_{BK} M^{-}_{BK} \tag{3.72}$$

Substituting these two equations above to Eq. (3.70) yields,

$$\begin{aligned} \hat{x}^{+}_{Bk} &= \hat{x}^{-}_{Fk} - \delta\hat{x}^{+}_{Bk} \\ &= P^{+}_{BK} M^{-}_{BK} \hat{x}^{-}_{Bk} - P^{+}_{BK} H^{T}_{k} R^{-1}(\delta z_k - H_k \hat{x}^{-}_{Fk}) \end{aligned} \tag{3.73}$$

Eq. (3.73) is rearranged as,

$${P^{+}_{BK}}^{-1} \hat{x}^{+}_{Bk} = M^{-}_{BK} \hat{x}^{-}_{Bk} - H^{T}_{k} R^{-1}(\delta z_k - H_k \hat{x}^{-}_{Fk}) \tag{3.74}$$

$$\begin{aligned} \hat{y}^{+}_{Bk} &= M^{+}_{BK} \hat{x}^{+}_{Bk} \\ &= \hat{y}^{-}_{Bk} - H^{T}_{k} R^{-1}(\delta z_k - H_k \hat{x}^{-}_{Fk}) \end{aligned} \tag{3.75}$$

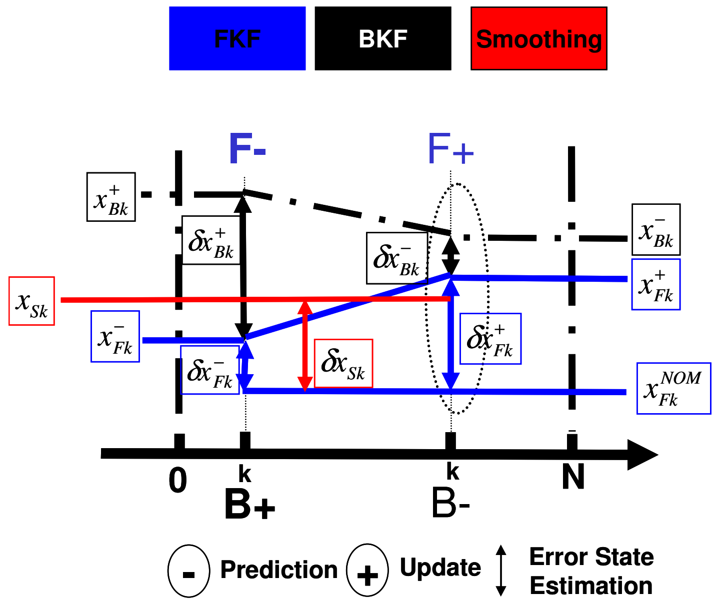

Figure 3.9 Relationship between BKF, FKF and Smoother in TFS

(After Liu et. al., 2009)

However, the straightforward practice of IKF on non-linear INS navigation model failed to achieve the expected superior smoothing results. This problem was resolved by the revision that was originally proposed for pipeline surveys using inertial measurement (Yu et al., 2005). As shown in Figure 3.9, the main idea of this modification is that the BKF nominal trajectory is reset to the FKF updated result at the BKF prediction step, which means the BKF nominal trajectory is revised to track the EKF estimation of the forward filter. This concept resembles the EKF error state feedback step. The details begin with a series of expressions as:

$$\hat{x}_{Fk}^{+} = \hat{x}_{Fk}^{-\ NOM} - \delta\hat{x}_{Fk}^{+} = \hat{x}_{Fk}^{-} - \delta\hat{x}_{Fk}^{+} \tag{3.76}$$

$$\hat{x}_{Bk}^{+} = \hat{x}_{Bk}^{+\ NOM} - \delta\hat{x}_{Bk}^{+} = \hat{x}_{Fk}^{-} - \delta\hat{x}_{Bk}^{+} \tag{3.77}$$

$$\hat{x}_{Bk}^{-} \equiv \hat{\bar{x}}_{Bk}^{-\ NOM} - \delta\hat{\bar{x}}_{Bk}^{-} = \hat{x}_{Fk}^{+} - \delta\hat{\bar{x}}_{Bk}^{-} \tag{3.78}$$

where $\hat{\bar{x}}_{Bk}^{-\ NOM}, \delta\hat{\bar{x}}_{Bk}^{-}$ is the revised BKF predicted nominal value, and the error state prediction (or the predicted perturbation);

Eq. (3.76) indicates that the FKF updated system state is perturbed from the FKF prediction as discussed in previous sections;

Eq. (3.77) indicates that the BKF updated system state is perturbed from the FKF prediction;

Eq. (3.59) indicates that the BKF predicted system state is originally perturbed from the FKF prediction;

Eq. (3.78) indicates that the BKF predicted system state is reset to be perturbed from the FKF update.

By using the relationship equations above, Eq. (3.68) is rearranged as,

$$\begin{aligned} M_{BK}^{+}\hat{x}_{Bk}^{+} &= M_{BK}^{+}(\hat{x}_{Fk}^{-} - \delta\hat{x}_{Bk}^{+}) \\ &= M_{BK}^{-}\hat{x}_{Bk}^{-} - H_k^T R^{-1}(\delta z_k - H_k\hat{x}_{Fk}^{-}) \\ &= M_{BK}^{-}(\hat{x}_{Fk}^{-} - \delta\hat{x}_{Bk}^{-}) - H_k^T R^{-1}(\delta z_k - H_k\hat{x}_{Fk}^{-}) \\ &\equiv M_{BK}^{-}(\hat{x}_{Fk}^{+} - \delta\hat{\bar{x}}_{Bk}^{-}) - H_k^T R^{-1}(\delta z_k - H_k\hat{x}_{Fk}^{-}) \end{aligned} \tag{3.79}$$

The desired form for updated error state is derived from Eq. (3.79) as (Yu et al., 2005):

$$\begin{aligned} \delta\hat{y}_{Bk}^{+} &= M_{BK}^{+}\delta\hat{x}_{Bk}^{+} \\ &= M_{BK}^{+}\hat{x}_{Fk}^{-} - M_{BK}^{-}(\hat{x}_{Fk}^{+} - \delta\hat{\bar{x}}_{Bk}^{-}) + H_k^T R^{-1}(\delta z_k - H_k\hat{x}_{Fk}^{-}) \\ &= M_{BK}^{+}\hat{x}_{Fk}^{-} - M_{BK}^{-}\hat{x}_{Fk}^{+} - H_k^T R^{-1} H_k\hat{x}_{Fk}^{-} + H_k^T R^{-1}\delta z_k + M_{BK}^{-}\delta\hat{\bar{x}}_{Bk}^{-} \end{aligned} \tag{3.80}$$

Substituting Eq. (3.67) into Eq. (3.80) yields,

$$\begin{aligned}\delta\hat{y}_{Bk}^{+} &= (M_{Bk}^{-} + H_k^T R^{-1} H_k)\hat{x}_{Fk}^{-} - M_{BK}^{-}\hat{x}_{Fk}^{+} - H_k^T R^{-1} H_k \hat{x}_{Fk}^{-} + H_k^T R^{-1}\delta z_k + M_{BK}^{-}\delta\hat{x}_{Bk}^{-} \\ &= M_{Bk}^{-}(\hat{x}_{Fk}^{-} - \hat{x}_{Fk}^{+}) + H_k^T R^{-1}\delta z_k + M_{BK}^{-}\delta\hat{x}_{Bk}^{-} \\ &= M_{Bk}^{-}\delta\hat{x}_{Fk}^{-} + H_k^T R^{-1}\delta z_k + M_{BK}^{-}\delta\hat{x}_{Bk}^{-}\end{aligned} \quad \textbf{(3.81)}$$

Therefore, Eq. (3.81) along with Eq. (3.67) constitutes the modified BKF updating equations.

FKF and BKF Combination

The smoothing estimate, i.e. the combination of the FKF update and the BKF prediction as in Eq. (3.42)-(3.43), will be fixed according to the revised relationship equations as (Yu et al., 2005):

$$P_{Sk} = (P_{Fk}^{+\,-1} + P_{Bk}^{-\,-1})^{-1} = (M_{Fk}^{+} + M_{Bk}^{-})^{-1} \quad \textbf{(3.82)}$$

$$\begin{aligned}\hat{x}_{Sk} &= P_{Sk}(P_{Fk}^{+\,-1}\hat{x}_{Fk}^{+} + P_{Bk}^{-\,-1}\hat{x}_{Bk}^{-}) \\ &= P_{Sk}(M_{Fk}^{+}\hat{x}_{Fk}^{+} + \hat{y}_{Bk}^{-}) \\ &= P_{Sk}[M_{Fk}^{+}\hat{x}_{Fk}^{+} + M_{Bk}^{-}(\hat{x}_{Fk}^{+} - \delta\hat{x}_{Bk}^{-})] \\ &= P_{Sk}(M_{Fk}^{+} + M_{Bk}^{-})\hat{x}_{Fk}^{+} - P_{Sk}M_{Bk}^{-}\delta\hat{x}_{Bk}^{-} \\ &= \hat{x}_{Fk}^{+} - P_{Sk}\delta\hat{y}_{Bk}^{-} = \hat{x}_{Fk}^{+} - \delta\hat{x}_{Sk}\end{aligned} \quad \textbf{(3.83)}$$

Another form to express the combination is derived as,

$$\hat{x}_{Sk} = \hat{x}_{Fk}^{-} - (\delta\hat{x}_{Fk}^{+} + P_{Sk}\delta\hat{y}_{Bk}^{-}) = \hat{x}_{Fk}^{-} - \delta\hat{x}_{Sk} \quad \textbf{(3.84)}$$

which indicates that the smoothing result can be regarded as the simple fixing of the FKF estimation; moreover, either the FKF update or the FKF prediction can be considered as the smoother nominal trajectory. These concepts are shown in Figure 3.9.

The two descriptions of the smoothing error state estimate corresponding to Eq. (3.83) and Eq. (3.84) are,

$$\delta\hat{x}_{Sk} = P_{Sk}\delta\hat{y}^{-}_{Bk}\,;\,\delta\hat{x}_{Sk} = \delta\hat{x}^{+}_{Fk} + P_{Sk}\delta\hat{y}^{-}_{Bk} \qquad \textbf{(3.85)}$$

Additionally, Joseph forms of BKF and smoother covariance equations are used to yield stable solutions as in Table 3.1 (Maybeck, 1994).

Table 3.1 Joseph forms

Joseph forms	**BKF Prediction**	$M^{-}_{Bk} = F^{T}_{k}\{[I-K^{-}_{Bk}]M^{+}_{Bk+1}[I-K^{-}_{Bk}]^{T} + K^{-}_{Bk}Q^{-1}K^{-\,T}_{Bk}\}F_{k}$
	Smoother Covariance	$K_{Sk} = (P^{+}_{Fk}M^{-}_{Bk} + I)^{-1}$ $W_{Sk} = P^{+}_{Fk}K^{T}_{Sk}$ $Y_{Sk} = I - W_{Sk}M^{-}_{Bk}$ $P_{Sk} = Y_{Sk}P^{+}_{Fk}Y^{T}_{Sk} + W_{Sk}M^{-}_{Bk}W^{T}_{Sk}$

3.3.2 Rauch-Tung-Striebel Smoother (RTSS)

The Rauch-Tung-Striebel Smoother (RTSS) was first presented by Rauch et al. (1965). It was proved as the optimal smoothing method for linear systems on basis of Maximum Likelihood (ML) criterion. It was demonstrated that the traditional TFS proposed by Fraser and Potter (1969) and the RTSS were mathematically equivalent in linear case. The RTSS has been widely applied in navigation applications due to its robustness and effectiveness.

The implementation of RTSS does not require the process of a full-scale BKF. It can be regarded as an add-on correction to the Kalman Filter (Gelb, 1974). RTSS is consisting of one forward data processing part and one backward data processing part. The former is the FKF as discussed in the previous section. The backward processing part propagates the filtering results and achieves the smoothing system state estimate by utilizing a set of equations as following,

$$K_{Sk} = P_{Fk}^{+} F_k (P_{Fk+1}^{-})^{-1} \tag{3.86}$$

$$P_{Sk} = P_{Fk}^{+} + K_{Sk} [P_{Sk+1} - P_{Fk+1}^{-}] K_{Sk}^{\ T} \tag{3.87}$$

$$\delta\hat{x}_{Sk} = \delta\hat{x}_{Fk}^{+} + K_{Sk} [\delta\hat{x}_{Sk+1} - \delta\hat{x}_{Fk+1}^{-}] \tag{3.88}$$

$$\hat{x}_{Sk} = \hat{x}_{Fk}^{-} - \delta\hat{x}_{Sk} \tag{3.89}$$

where K_{Sk} denotes the RTSS gain; $\delta\hat{x}_{Sk}$ denotes the RTSS perturbation.

The equations show that the FKF prediction results can be regarded as the RTSS nominal trajectory. Further, by utilizing all the information stored in the FKF, the RTSS recursively updates the smoothed estimate and its covariance in a backward sweep. On the other hand, the determination of the RTSS estimates does not involve the smoother covariance; the smoothing gain can be computed during the forward filter process. This convenience brings an important characteristic that the forward filter covariance as well as the state matrix needs not to be stored, if the smoother covariance calculation for analysis purpose can be omitted.

3.4 Smoother Considerations

3.4.1 Smoothability

A state is defined to be "smoothable" if an optimal smoother provides this state a superior estimate compared to that obtained by the simpler means of extrapolating the final FKF estimate backward in time (Gelb, 1974; Maybeck, 1994). Fraser (1967) showed that only those states controllable by the system driving noise were smoothable in linear systems. This indicates that the estimation accuracy of constant variable with no driving noise can barely be improved by optimal smoothing over filtering. This was simply proved with continuous-time smoothing equations by assuming the process noise as "zero" in a linear system. An alternative demonstration of this conclusion can be derived by examining the duality between control and estimation from solving the two-point-boundary-value-problem (TPBVP) associated with the optimal control theory (Crassidis and Junkins, 2004). The quantity representation of smoothability has not been clarified and is beyond the content of this research.

3.4.2 Measurement Gap Filling

KF update steps take place when measurements are available. IMU data rate is always higher than that of the augmentation sensor. Besides, due to occasional signal blockages and unexpected faults, the augmentation observations (especially GPS) are sometimes unavailable. These conditions are called measurement gaps. Under these conditions, the KF only works in prediction modes. Meanwhile, the error state and the covariance updates cannot be generated and the smoothing computation is interrupted, or even halted. To solve this problem, the straightforward idea is to interpret the KF prediction solution as the temporary update replacement (Nassar, 2003; Shin and El-Sheimy, 2002; Godha, 2006) as shown in Figure 3.10. It is reluctantly accepted for INS-based integration estimation applications since the predictions are the best obtainable resources when no dependable measurements are offered. This replacement is described as,

$$P^{+}_{FGAP} = P^{-}_{FGAP}; P^{+}_{BGAP} = P^{-}_{BGAP} \quad \textbf{(3.90)}$$

$$\delta\hat{x}^{+}_{FGAP} = \delta\hat{x}^{-}_{FGAP}; \delta\hat{x}^{+}_{BGAP} = \delta\hat{x}^{-}_{BGAP} \quad \textbf{(3.91)}$$

where the subscript GAP denotes the time intervals corresponding to the measurement gaps.

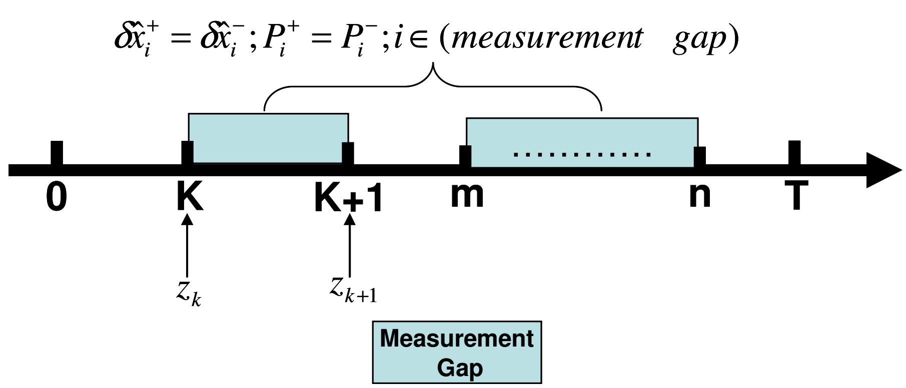

Figure 3.10 Measurement Gap Filling

3.4.3 Storage Requirement

The FKF information required for storage in TFS and RTSS is listed as,

- FKF nominal trajectory $\hat{x}^{-\ NOM}_{Fk}$;
- FKF error state update $\delta\hat{x}^{+}_{Fk}$; FKF covariance update P^{+}_{Fk};

- FKF error state prediction $\delta\hat{x}_{Fk}^{-}$; FKF covariance prediction P_{Fk}^{-}.

Other concerns related to storage requirement for smoothers include:

- If the reset feedback rate equals to the KF computing rate, only the nominal trajectory at the final epoch is needed to be stored. Others can be recomputed by using the FKF error state update.
- If the feedback rate equals to the KF computing rate, $\delta\hat{x}_{Fk}^{-} = 0 \quad k \in (t_0, t_N)$. Apparently, the FKF error state predictions are not required for storage under this condition.
- Because of the symmetric nature of covariance matrix, special polynomial techniques can be applied to improve its storage efficiency (Shin and El-Sheimy, 2002).
- In RTSS, the FKF covariance and the nominal trajectory need not to be stored since the RTSS gain can be computed during the forward filter process, if the smoother covariance for analysis purpose can be omitted.
- TFS does not acquire storing all the intermediate results of the forward filter. Instead, only the estimates and covariance during the intervals where the smoothing would be implemented are required to save. Conversely, since RTSS is recursively processed, all the information starting from the FKF final time epoch to the current smoothing time epoch is necessarily to be stored.

Chapter Four: OPTIMAL SMOOTHING FOR LAND-VEHICLE NAVIGATION USING INTEGRATED INS/GPS SYSTEMS

4.1 Overview of Land-Vehicle Navigation Using Integrated INS/GPS Systems

The last two decades have shown an increasing trend in the use of navigation technologies in vehicular applications which made Land-Vehicle Navigation (LVN) a typical business in the market. The most commonly used navigation systems in LVN applications are the systems that integrate a Global Positioning System (GPS) and an Inertial Navigation System (INS). This is due to the fact that both systems are complimentary and their integration overcomes their individual limitations. In INS/GPS integrated systems, the GPS provides position/velocity and the INS provides attitude information. In addition, the INS is used to detect and repair GPS cycle slips; it is also used for navigation during GPS signal loss of lock. The integration of high or medium quality Inertial Measuring Units (IMUs) with GPS has been implemented for precise kinematic navigation. However, these inertial systems are limited by their significant size and cost. In addition, with the new government regulations, the use of such systems will be restricted and permitted only for authorized personnel (Niu et. al., 2006). To meet the high demand in LVN, the market has been directed towards using Micro-Electro-Mechanical Systems (MEMS) inertial sensors.

In general, any type of IMU/GPS integrated system sometimes has a major problem. This problem is associated with the frequent occurrence of GPS outages caused by GPS signal blockages in certain situations such as urban centres. In case of GPS signal blockages, navigation is provided using the IMU instead of the GPS until satellite signals are obtained again with sufficient accuracy. Since any IMU can only provide very short-time high accuracy navigation, the accuracy of the provided navigation parameters during these periods decreases with time. During GPS signal outages, the accumulated IMU position error at the end of the outage interval is dependent on the outage time interval (time elapsed since last GPS update), the quality of the IMU, the quality of the GPS updates before the outage and the vehicle dynamics before and during the outage (Nassar et al. 2004). Kalman Filter (KF) is recognized as the most widely used optimal estimator in INS/GPS integrated systems. With the development of low-end tactical-grade and MEMS IMUs, the Extended Kalman Filter (EKF) is commonly accepted to resolve the system nonlinearity and accomplish the real-time navigation. However, in the context of INS/GPS integration, the KF will work in prediction mode during GPS signal outages where the navigation solution is completely obtained by stand-alone INS. During these GPS outages, the navigation accuracy degrades rapidly with time due to the INS time-dependent error behavior. As a result, this performance cannot meet the requirement of high accuracy LVN. Hence, post-processing methods such as backward smoothing can be employed in such cases to provide a better navigation solution.

The process model and the measurement model for integrated INS/GPS systems and the affiliated a priori noise knowledge for both forward and backward filters are referred to the discussions in the previous chapters.

The performance of both optimal smoothers will be demonstrated using two land-vehicle INS/GPS data sets with intentionally simulated GPS outages. The first data set incorporates a tactical-grade IMU (Litton LN200) while the second one utilizes a low-cost MEMS custom-built IMU by the MMSS Research Group at UofC. The achieved results for both data sets will be analyzed and discussed. Moreover, the TFS results are compared to those obtained by the RTSS. Finally, the effect of the GPS signal outage length on the smoother performance will be evaluated.

4.2 Tactical-grade IMU Test (1st Test)

4.2.1 Description of the 1st Test

A tactical-grade IMU, Litton LN200, was used to conduct the first field test. This test was performed along an L-shape route, in Balzac Park, Calgary, Alberta. NovAtel OEM4 GPS receivers were used to provide DGPS solutions. A navigation-grade IMU (Honeywell CIMU) was used to provide the inertial reference trajectory for the test by processing the DGPS/CIMU without any GPS signal outages. Three GPS outages, each with 60s length, were intentionally simulated in this test to evaluate the smoothing efficiency. The reference trajectories, as well as the GPS outages for this test are illustrated in Figure 4.1. The centimetre positioning accuracy levels, in terms of the Standard Deviations (STDs) for the DGPS solutions, are shown in Figure 4.2. The tuned parameters of the inertial sensors for the process noise spectral density matrix in the KF are listed in Table 4.1 (See Litton LN200 IMU Specifications in Appendix A), where the tuning technique refers to Goodall (2009). The data processing strategies to evaluate the performance of filters and smoothers are listed step by step as follows,

- Land-vehicle Forward Kalman Filter (FKF)
- Two Filter Smoother (TFS)
    - Backward Kalman Filter (BKF)
    - FKF/BKF Combination
- RTS Smoother (RTSS)

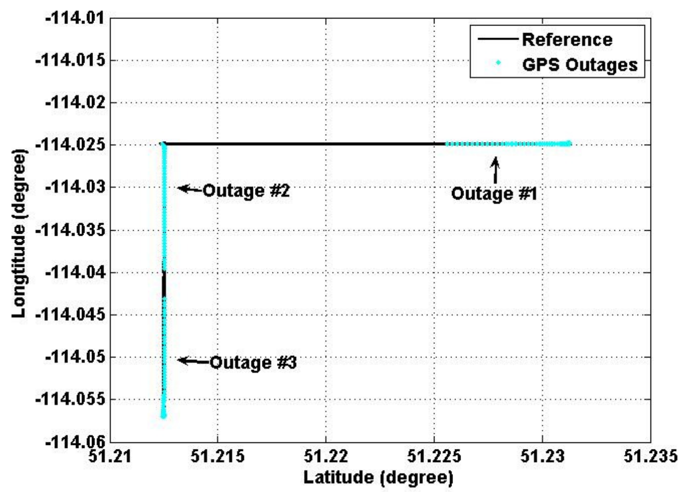

Figure 4.1 Reference Trajectory and GPS Outages in the 1st test

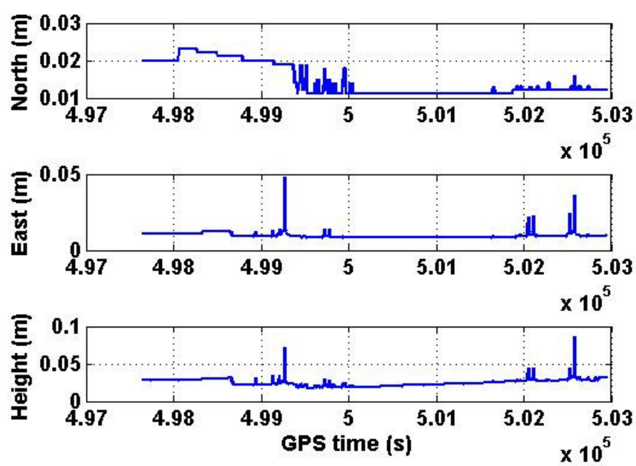

Figure 4.2 DGPS Positioning Accuracy in the1st Test

Table 4.1 Kalman Filter Process Noise Parameters in the 1st test

Tuned Parameters		
VRW	$0.030 m/s/\sqrt{hour}$	
ARW	$0.125 \deg/\sqrt{hour}$	
Gauss-Markov of Gyro Bias	$\sigma = 1 \deg/hour$	$T = 1 hour$
Gauss-Markov of Acc Bias	$\sigma = 300 mGal$	$T = 1 hour$
Gauss-Markov of Gyro SF	$\sigma = 100 PPM$	$T = 4 hour$
Gauss-Markov of Acc SF	$\sigma = 300 PPM$	$T = 4 hour$

4.2.2 FKF Results of the 1st Test

Since tactical-grade IMU is used in this test, analytic coarse alignment as well as fine alignment is introduced to determine the initial attitude during the first 185s static IMU data interval. DGPS solution provides the initial position estimation. The initial velocity is set to be zero as static initial alignment is utilized.

Figure 4.3 shows the forward filtering trajectory including the zoomed GPS outage regions compared to the reference solution. As expected, the FKF trajectory diverges from the reference at each of the GPS outage periods. As discussed earlier, KF will only work in prediction mode during GPS measurement gaps. Therefore, the positioning accuracy achieved by stand-alone INS will degrade rapidly with time. Figure 4.4 depicts the KF position errors of the LN200 IMU during three GPS outages in the first test. The LN200 position errors are calculated by subtracting the filtering results from the corresponding reference solutions. It can be noted that the horizontal position error increases to the meter level during the outages, and the height error reaches the decimetre level. A further representation of the degraded estimation accuracy can be observed from Figure 4.6, which depicts the position error STDs. The velocity errors and STDs during the three GPS outages are shown in Figure 4.5 and Figure 4.7 respectively.

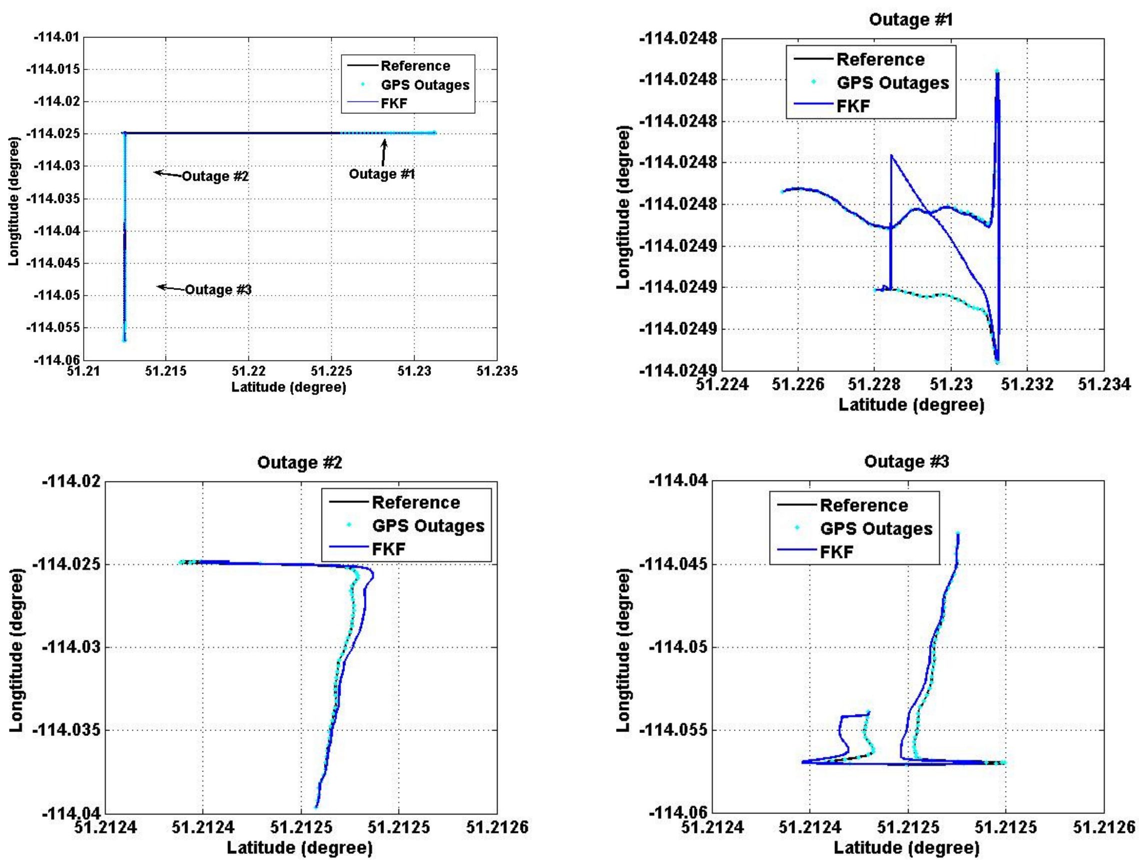

Figure 4.3 LN200 FKF Trajectory

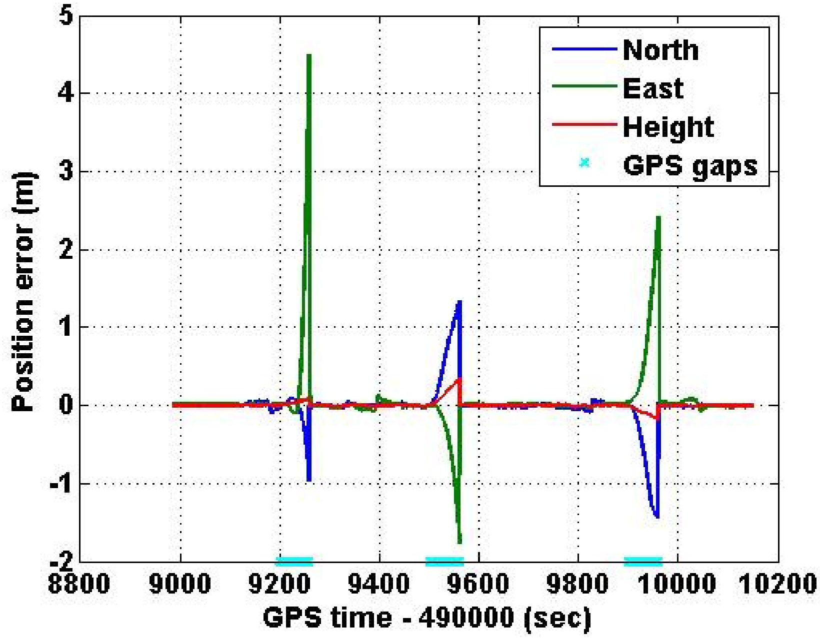

Figure 4.4 LN200 FKF Position Errors

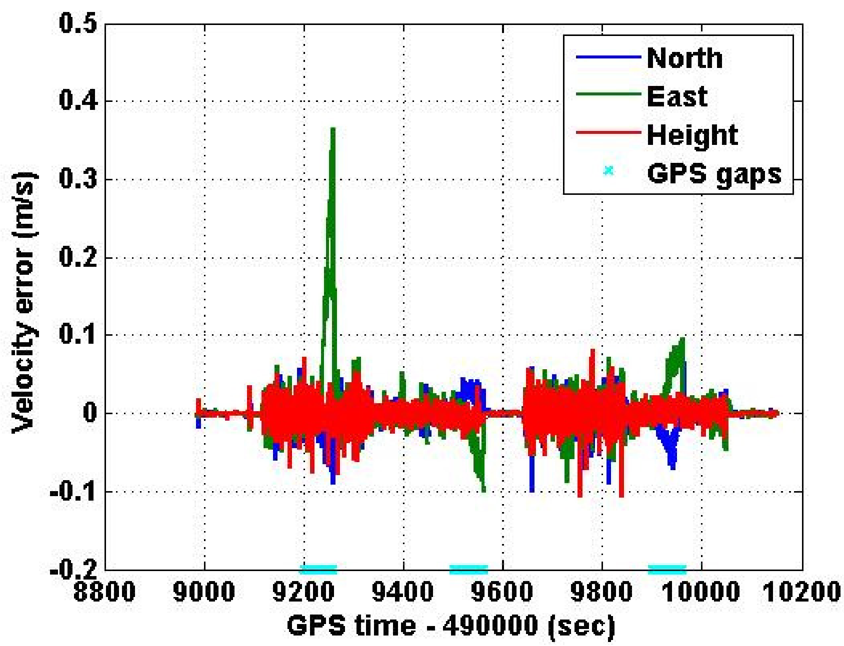

Figure 4.5 LN200 FKF Velocity Errors

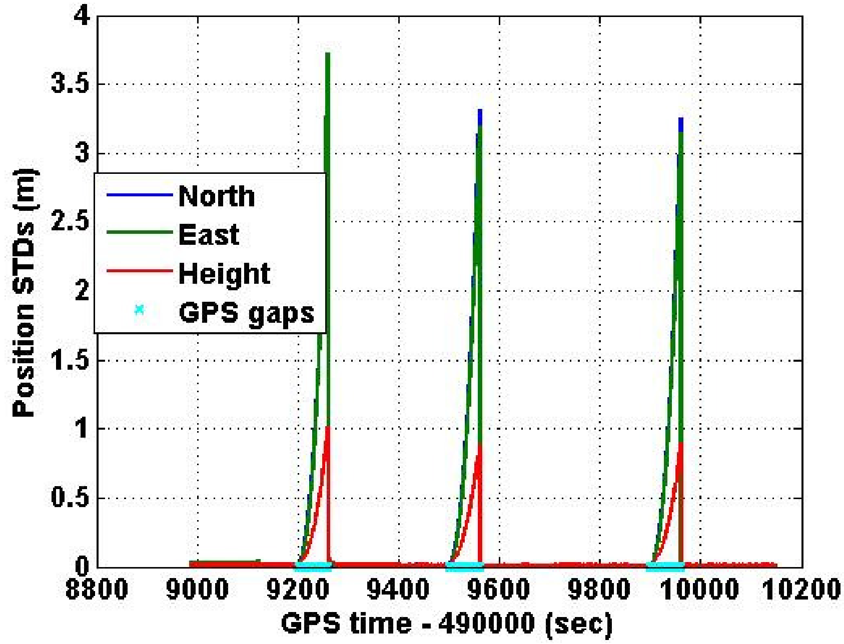

Figure 4.6 LN200 FKF Position Error STDs

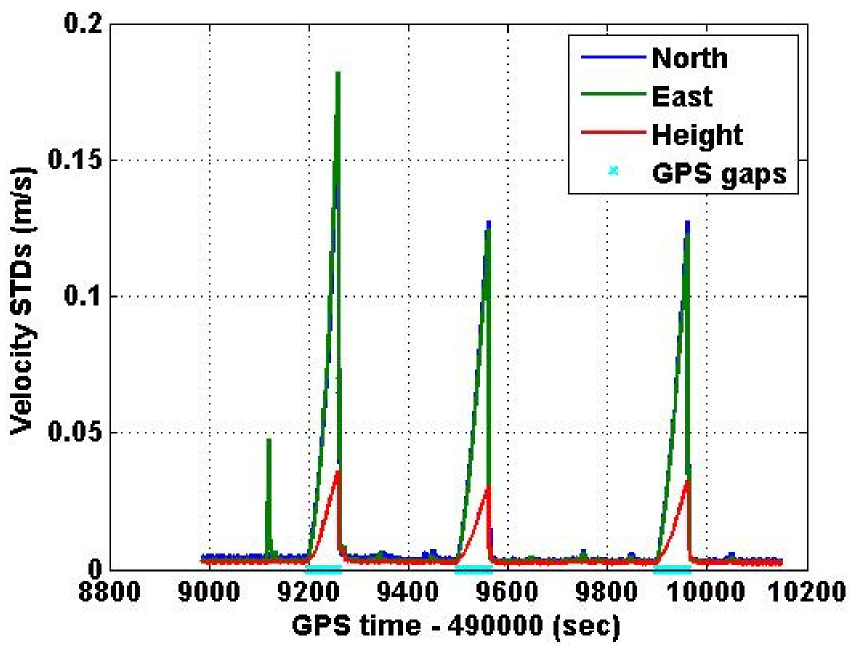

Figure 4.7 LN200 FKF Velocity Error STDs

4.2.3 TFS Results of the 1st Test

As stated earlier in Chapter 3, the implementation of TFS requires processing a backward filter, of which the INS solutions are dependent on the forward filter counterparts. The combination of the saved FKF results and the post-computed BKF results yields the smoother solutions. In order to avoid the undesirable matrix inversions and provide a valid backward initialization, new variables $P_B^{-1}, \delta y_B$ are introduced to replace the system error state and its covariance. Since the smoother is initialized using the FKF results at the final time epoch, the BKF initial error state is uncertain and its corresponding covariance is set to be infinity. As a result, the BKF results in terms of the original error state description δx_B will not be available to be calculated at the beginning part of BKF until the covariance matrix becomes relatively finite. Therefore, only the BKF results during the three GPS outages will be computed and shown for reference in this thesis since the measurement gaps are simulated with a reasonable distance from the final time epoch.

Figure 4.8 shows the trajectories of FKF, BKF, and TFS as well as the reference solution in the zoomed outage regions. Similar to FKF, the BKF trajectory diverges from the reference counterpart at each of the GPS outages, towards an uptrend reverse to the time increasing direction. Apparently, the smoothing trajectory approaches the reference solution compared to filtering results. Note that the BKF divergence at the third outage is even greater than the FKF. This is due to the fact that the norm of the backward covariance matrix is still remarkable since it is near the ending time epoch. This is gradually moderated as the backward filter runs reversely with time, which could be observed from the other two outages.

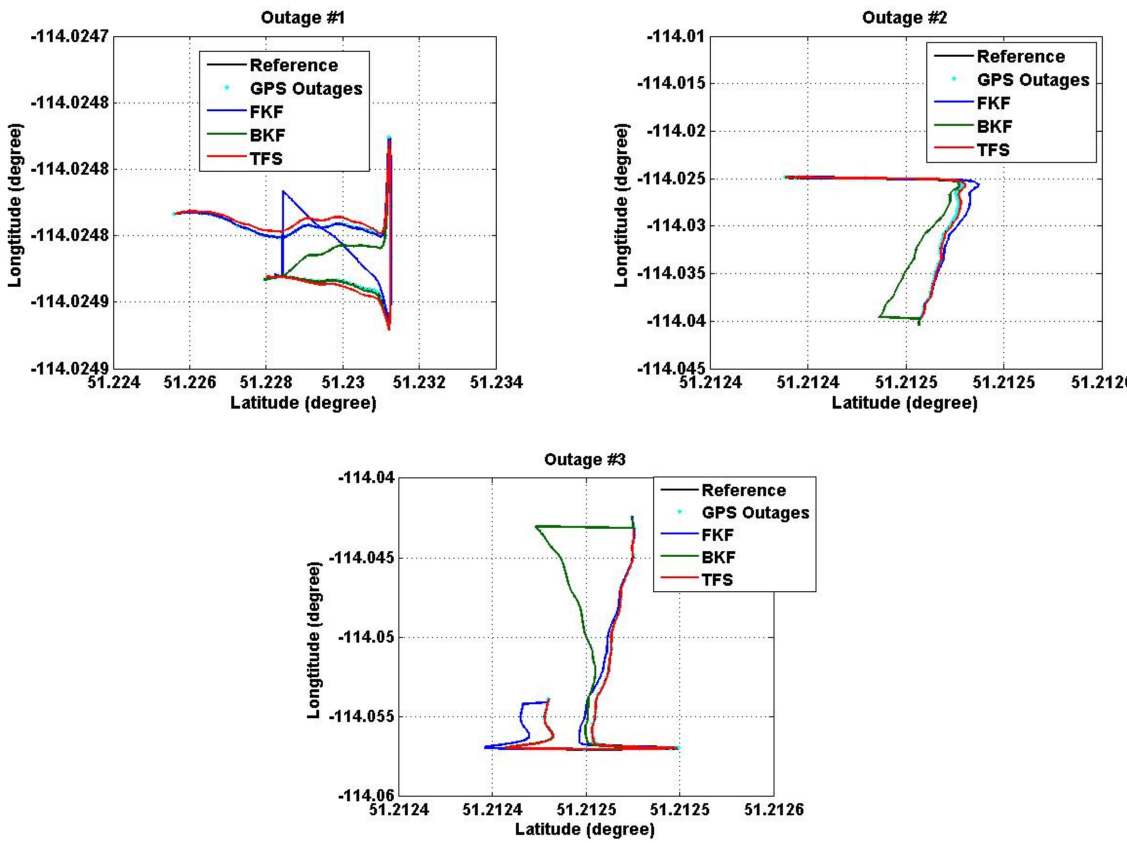

Figure 4.8 Trajectories of FKF, BKF, and TFS in the 1st Test

The LN200 TFS position errors across the three GPS outages and the corresponding STDs are shown in Figure 4.9 and Figure 4.11 respectively. It can be noted that while the horizontal position error is restricted to decimetre level, the height error is restricted to centimetre level. Additionally, the TFS velocity errors and STDs across the 3 DGPS outages are shown in Figure 4.10 and Figure 4.12 respectively. The position errors for TFS are calculated using the same criterion as in the FKF case.

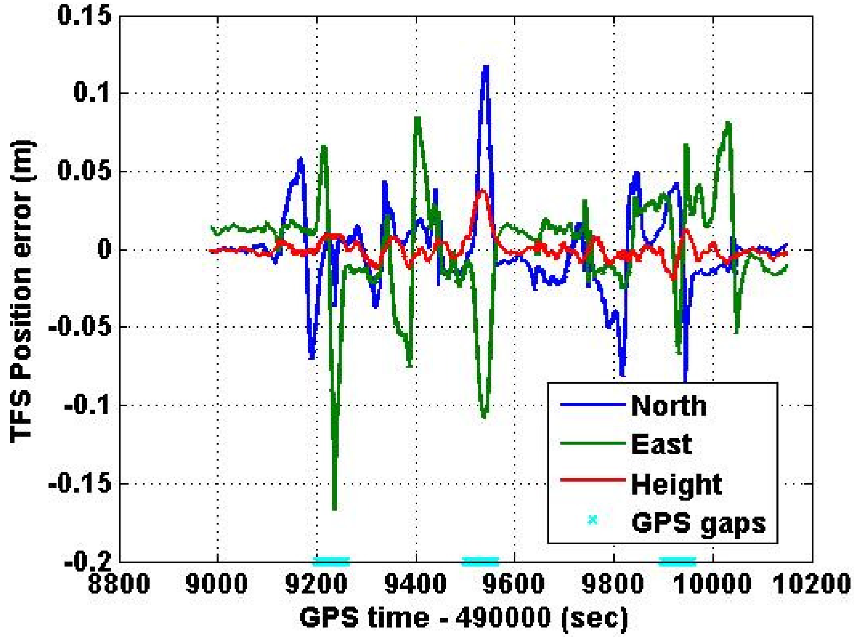

Figure 4.9 LN200 TFS Position Errors

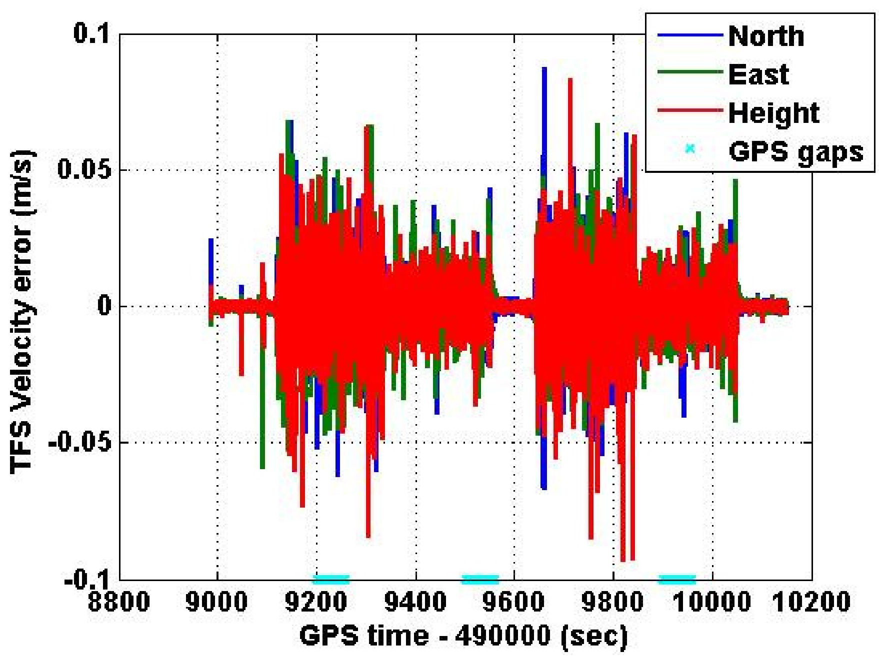

Figure 4.10 LN200 TFS Velocity Errors

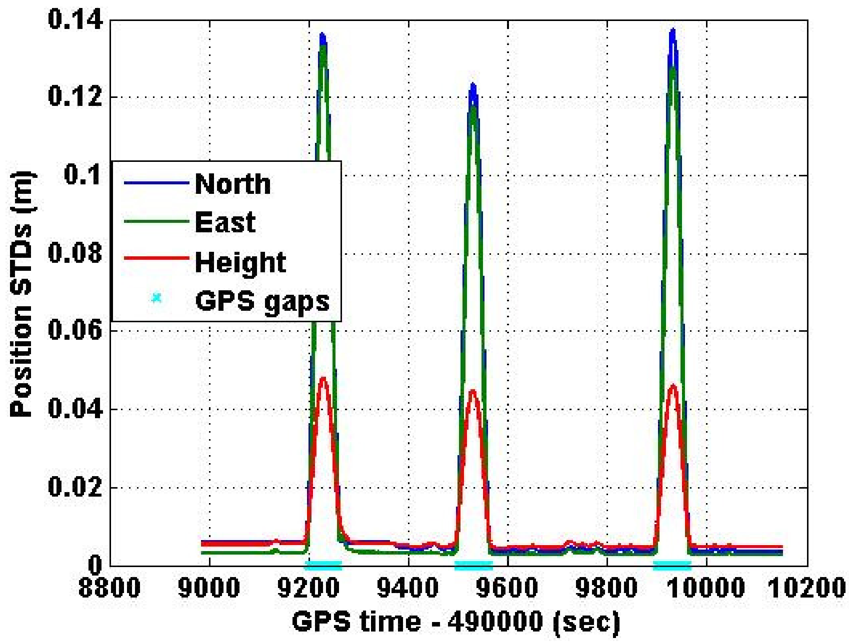

Figure 4.11 LN200 TFS Position Error STDs

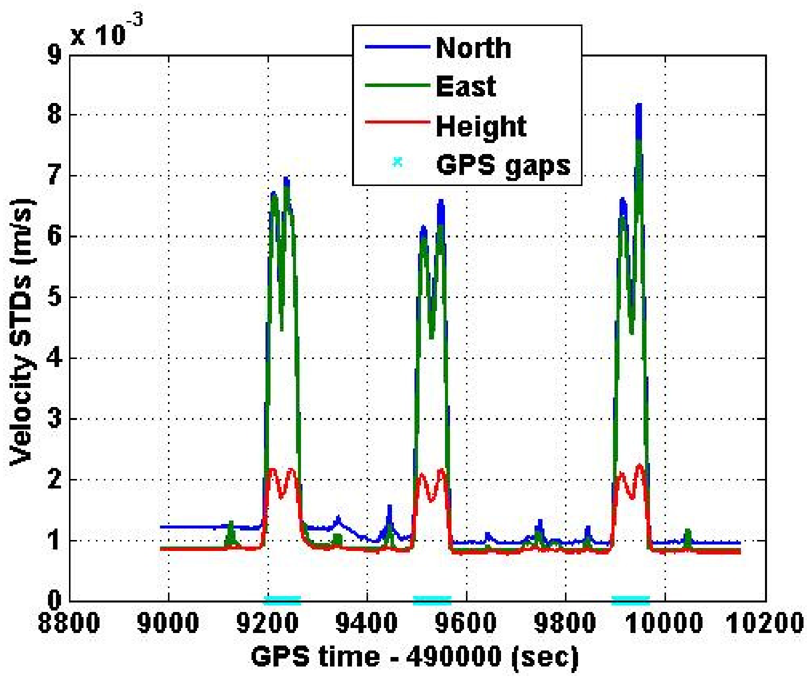

Figure 4.12 LN200 TFS Velocity Error STDs

4.2.4 RTSS Results of the 1st Test

Figure 4.13 shows the trajectories of FKF and RTSS as well as the reference solution in the zoomed outage regions. The LN200 RTSS position and velocity errors are shown in Figure 4.14. Their corresponding STDs are depicted in Figure 4.15.

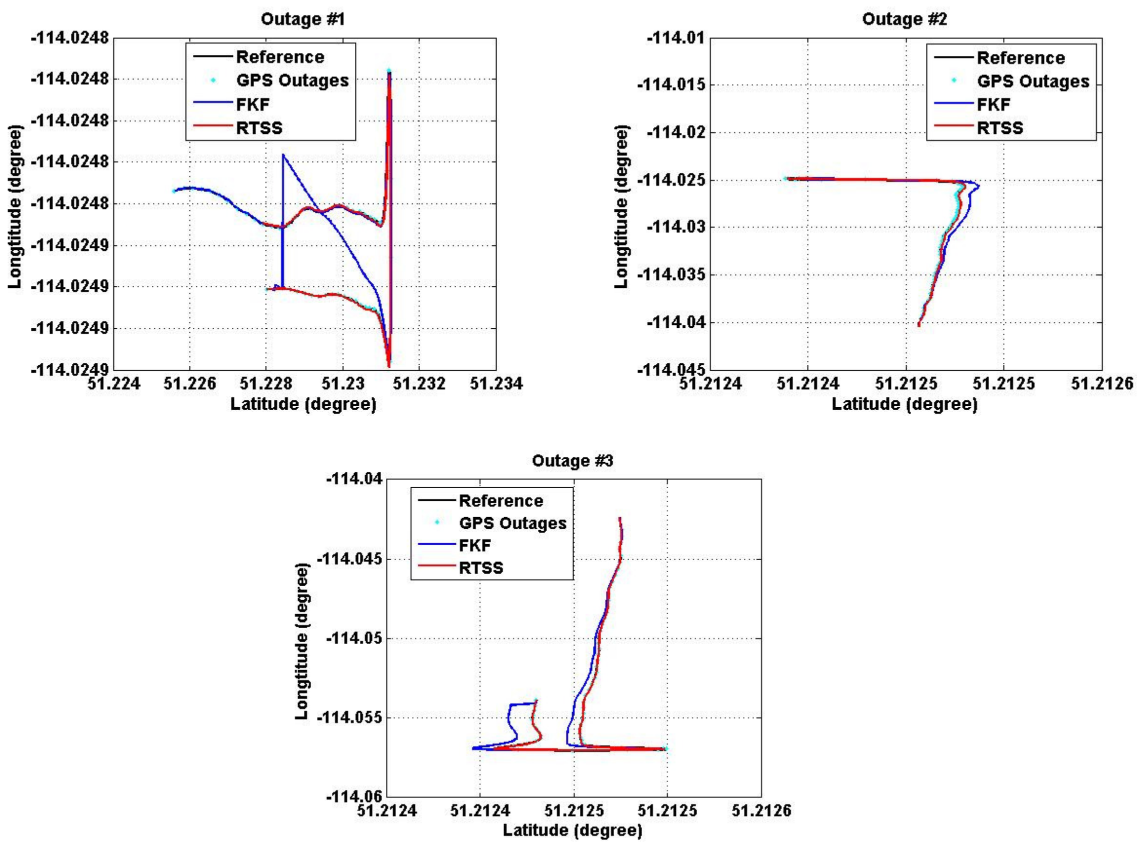

Figure 4.13 Trajectories of FKF and RTSS in the 1st Test

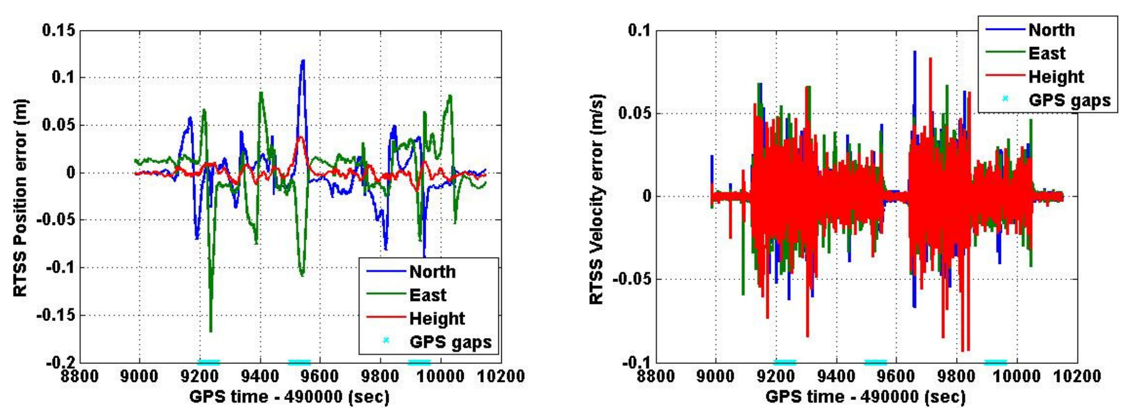

Figure 4.14 LN200 RTSS Position and Velocity Errors

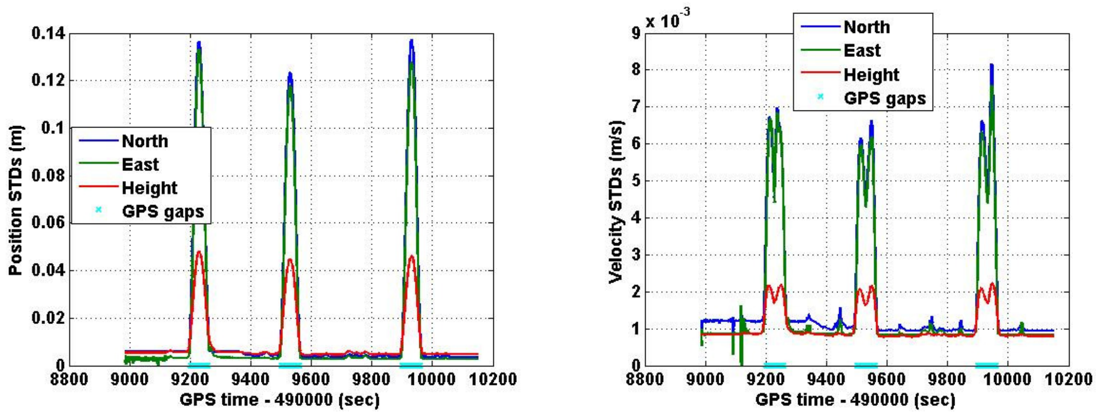

Figure 4.15 LN200 RTSS Position and Velocity Error STDs

4.2.5 Comparison between the TFS and RTSS Results of the 1st Test

The accumulated position errors can also be observed in the backward filtering results, but it will diverge towards the uptrend reverse to the FKF counterpart, i.e. the time increasing direction. By the combination of both filtering results, the position error drifts are expected to be suppressed or removed by the smoothing approaches. This effect is illustrated in Figure 4.16 which compares the north position errors between FKF, BKF, TFS and RTSS during the first 60s GPS outage. It shows that the position error drifts is restricted, or smoothed in the middle of both the forward and backward directions. In addition, Figure 4.17 shows the corresponding north position STD comparison.

The north position error and STD comparison in the other two outages are depicted in Figure 4.18 and Figure 4.19, respectively. They further indicate that the effect of large covariance matrix in backward filtering results will be gradually neutralized as the BKF is processed reversely with time.

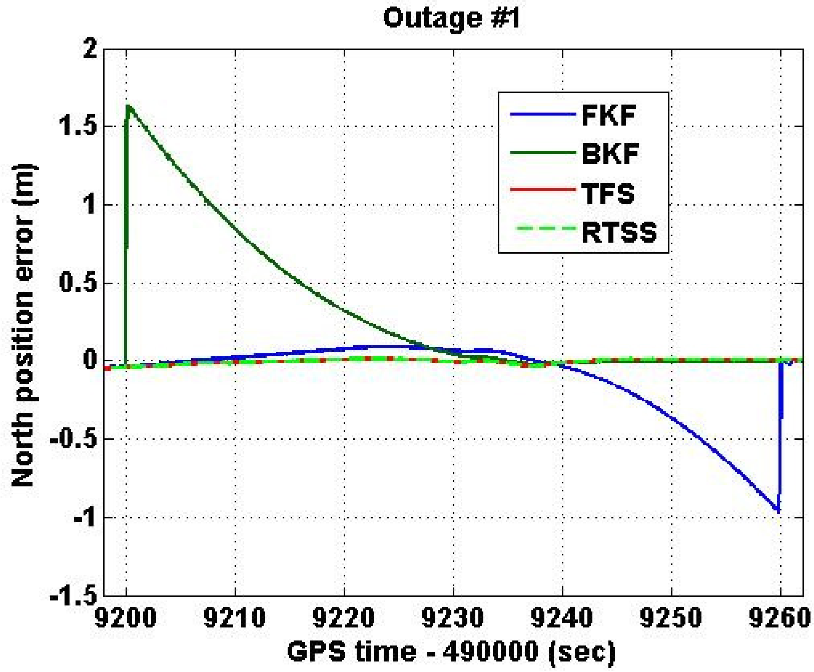

Figure 4.16 LN200 North Position Errors in the 1st Outage

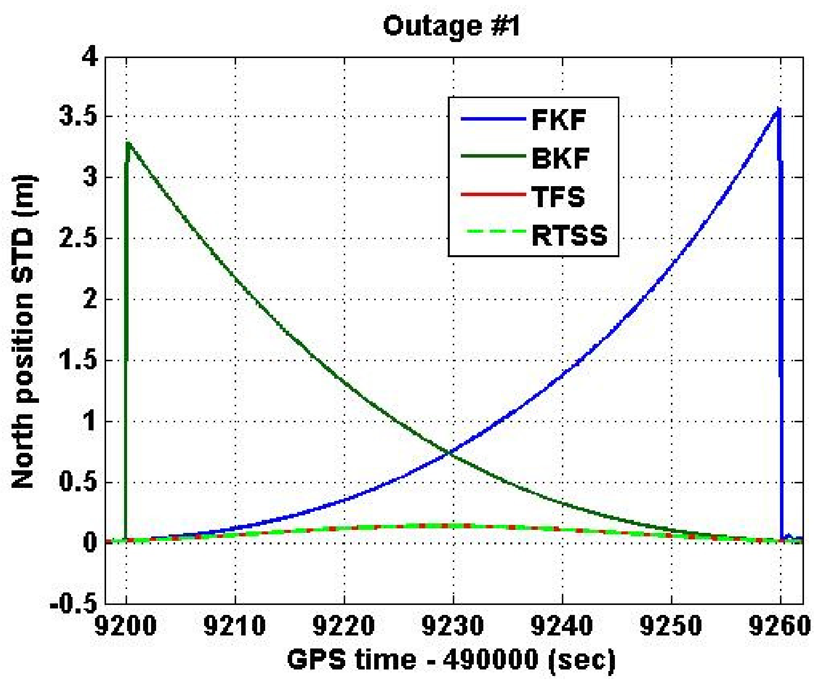

Figure 4.17 LN200 North Position Error STDs in the 1st Outage

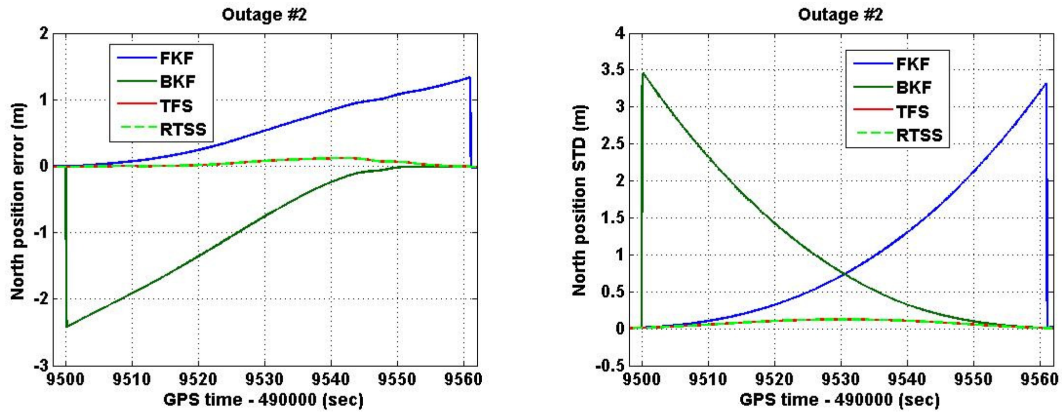

Figure 4.18 LN200 North Position Errors and STDs in the 2nd Outage

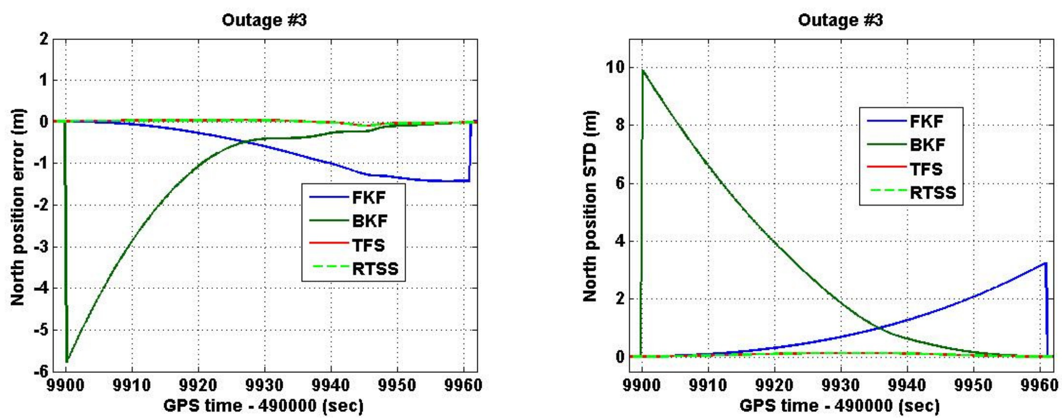

Figure 4.19 LN200 North Position Errors and STDs in the 3rd Outage

Table 4.2 LN200 Position Errors of FKF, TFS, and RTSS

Outage	North(m)			East(m)			Height(m)			3 D (m)		
	FKF	TFS	RTS	FKF	TFS	RTS	FKF	TFS	RTS	FKF	TFS	RTS
#1	0.968	0.042	0.042	4.490	0.167	0.167	0.086	0.010	0.010	4.594	0.169	0.169
#2	1.302	0.118	0.119	1.664	0.109	0.109	0.343	0.038	0.038	2.141	0.161	0.162
#3	1.426	0.093	0.096	2.349	0.067	0.072	0.188	0.019	0.020	2.752	0.108	0.108
Mean	1.232	0.084	0.085	2.835	0.114	0.116	0.205	0.022	0.023	3.162	0.146	0.147

The summary of the FKF, TFS, and RTSS LN200 results of the 1st test is shown in Table 4.2, in which the maximum position errors along north, east, and height directions are listed in each of the three GPS signal outage periods. The results showed that the navigation errors are significantly improved by both smoothing algorithms during GPS outages. In addition, the smoothing effect of the TFS is almost the same as the RTSS. The improvement level of both smoothers is nearly 95.4 %.

4.2.6 Effect of GPS Measurement Gap Length of the 1st Test

In addition to the three shown 60s GPS outage durations, 10s, 30s, 90s gap lengths are tested to evaluate the filtering and smoothing performance respectively. Similar to Figure 4.16, the comparison between the north position errors of FKF, BKF, TFS, and RTSS in the first 10s outage is illustrated in Figure 4.20. The corresponding comparison in the first 30s and 90s outage is shown in Figure 4.21 and Figure 4.22 respectively.

The detailed comparisons between different measurement GPS gap lengths (FKF, BKF, TFS, and RTSS) in terms of the mean maximum 3-D position errors and the improvement levels of smoothers over forward filtering are listed in Table 4.3. Further, the mean values of maximum position errors (north, east, height and 3-D) across all three outages for each estimation method and each measurement gap length are depicted in Figure 4.23 to Figure 4.26. The results show that although the position errors (including the smoothing results) rise as the outage length increases, the improvement level of each smoother over filtering becomes greater accordingly. This indicates that the efficiency of smoothers is upgrading with the increasing GPS outage period length despite that the upgrade is not remarkable from 60s to 90s. Also, the TFS and RTSS reach almost the same enhancement level with each outage length.

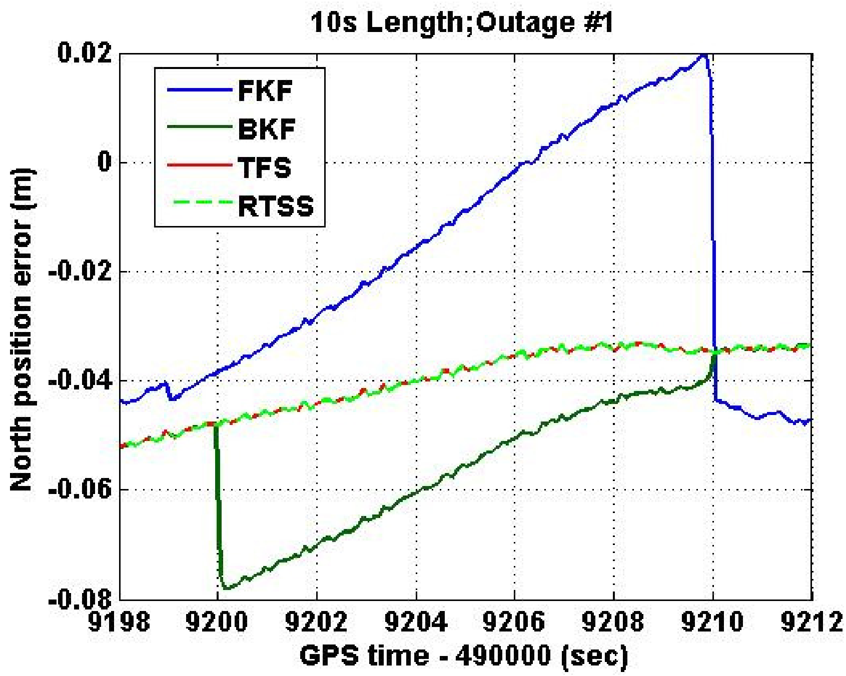

Figure 4.20 LN200 North Position Errors Comparison with 10s Outage Length

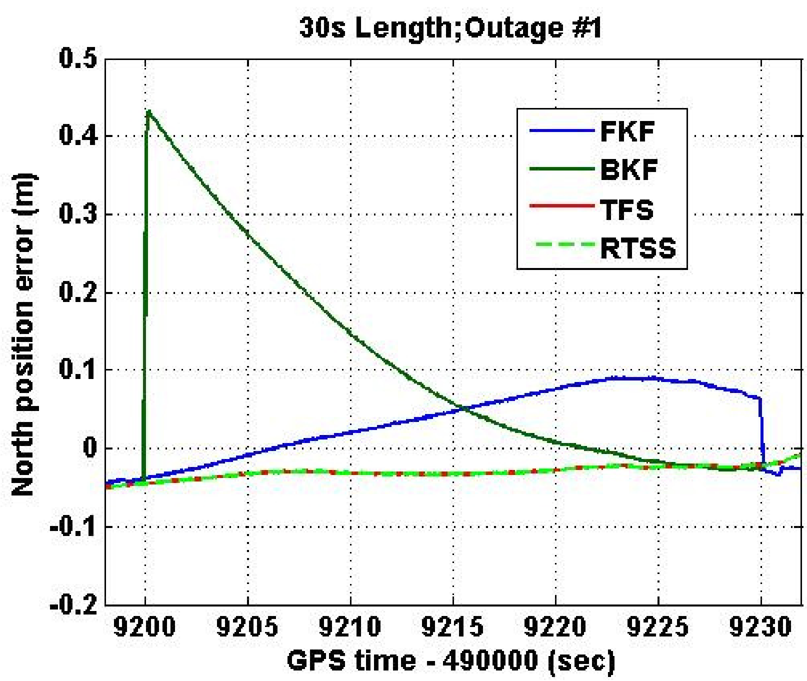

Figure 4.21 LN200 North Position Errors Comparison with 30s Outage Length

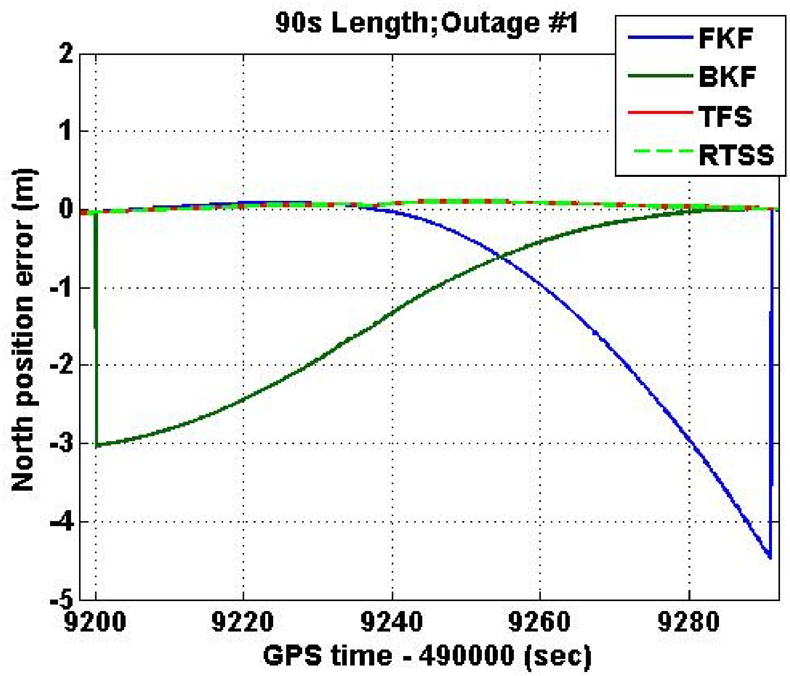

Figure 4.22 LN200 North Position Errors Comparison with 90s Outage Length

Table 4.3 LN200 3-D Position Error and Smoothing Improvement Level Comparison between Different Outage lengths

Outage Length	**Mean Maximum 3-D Position Error(m)**			**Improvement (%)**	
	FKF	**TFS**	**RTSS**	**TFS**	**RTSS**
10s	0.078	0.034	0.034	56.4	56.4
30s	0.519	0.053	0.053	89.8	89.8
60s	3.162	0.146	0.147	95.4	95.4
90s	11.54	0.398	0.392	96.6	96.6

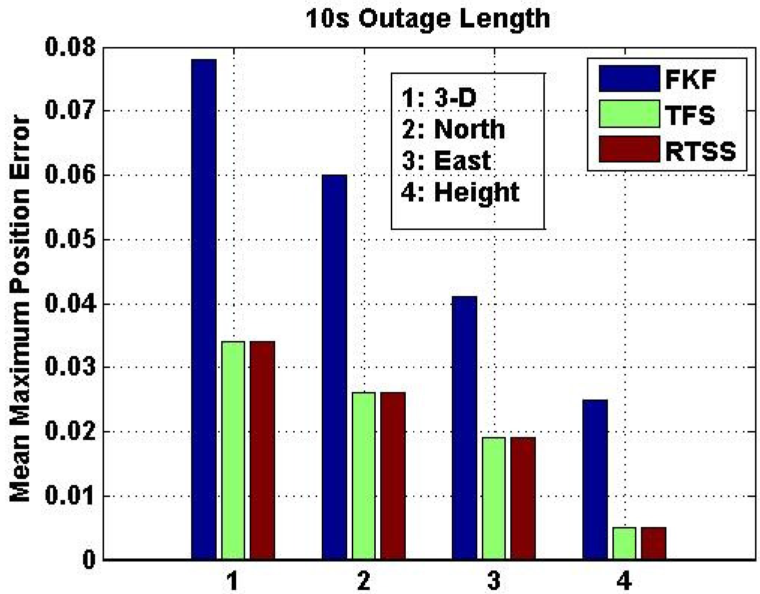

Figure 4.23 Mean Values of Maximum Position Errors across Three GPS 10s Outages

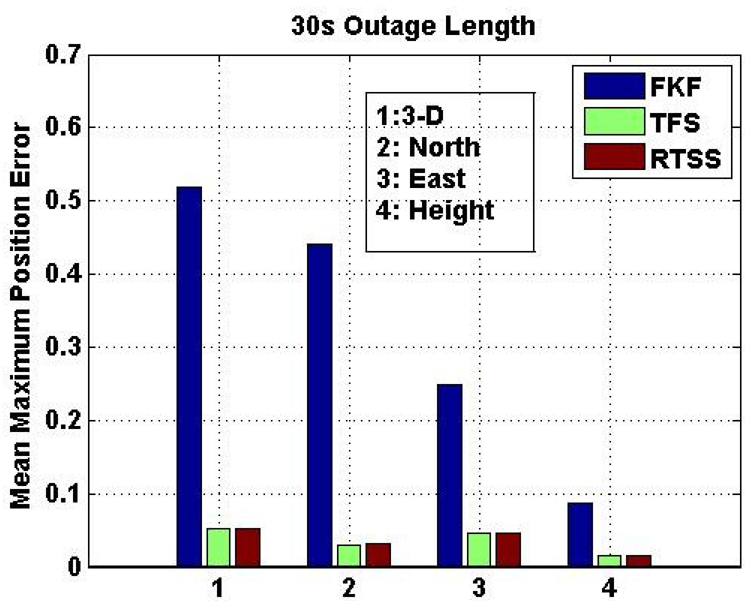

Figure 4.24 Mean Values of Maximum Position Errors across Three GPS 30s Outages

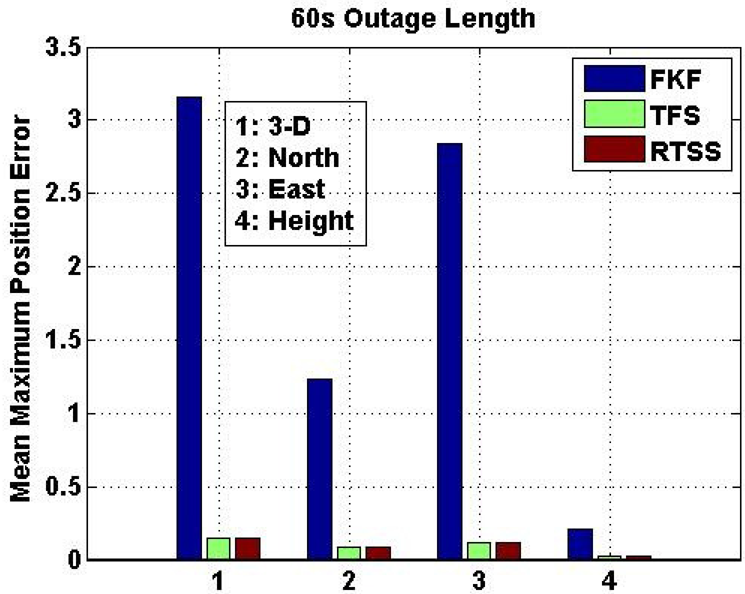

Figure 4.25 Mean Values of Maximum Position Errors across Three GPS 60s Outages

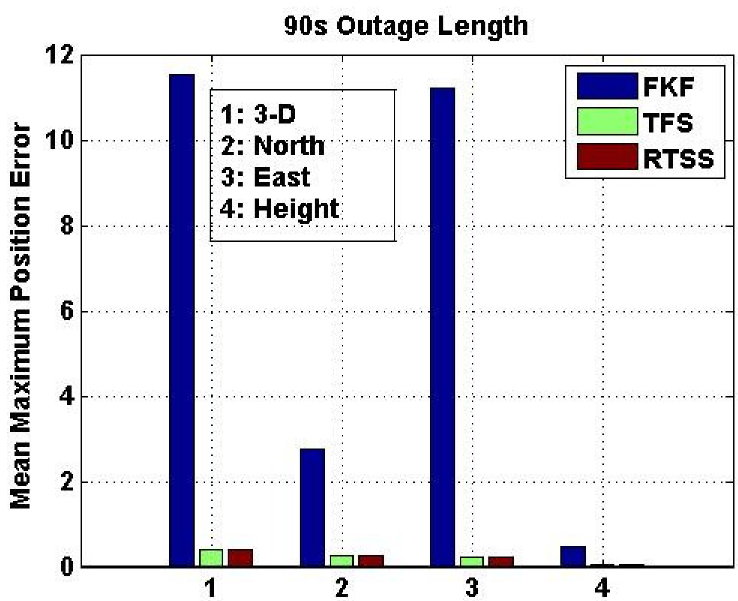

Figure 4.26 Mean Values of Maximum Position Errors across Three GPS 90s Outages

4.3 MEMS IMU Test (2nd Test)

4.3.1 Description of the 2nd Test

The second dataset was conducted along a large clockwise cycle route, Calgary, Alberta. A custom-built MEMS IMU integrated using inertial sensors from Analog Device Inc. (ADI), and a GPS Single Point Positioning (SPP) solution was used to verify the filtering and smoothing performance under the condition of meter level positioning aiding. The navigation-grade IMU (Honeywell C-IMU) was used to provide the reference trajectory without any GPS outages.

Five GPS outages, each with 60s length, were intentionally simulated in the second test to verify and compare the performance of filters and smoothers for error bridging. The reference trajectory, including the GPS outage regions for this test is illustrated in Figure 4.27. The positioning accuracy levels, in terms of the STDs for the GPS SPP solutions, are shown in Figure 4.28. The tuned parameters of the inertial sensors for the process noise spectral density matrix used in the KF are listed in Table 4.4. The data is processed as the same strategies of the 1st test discussed in the previous Section.

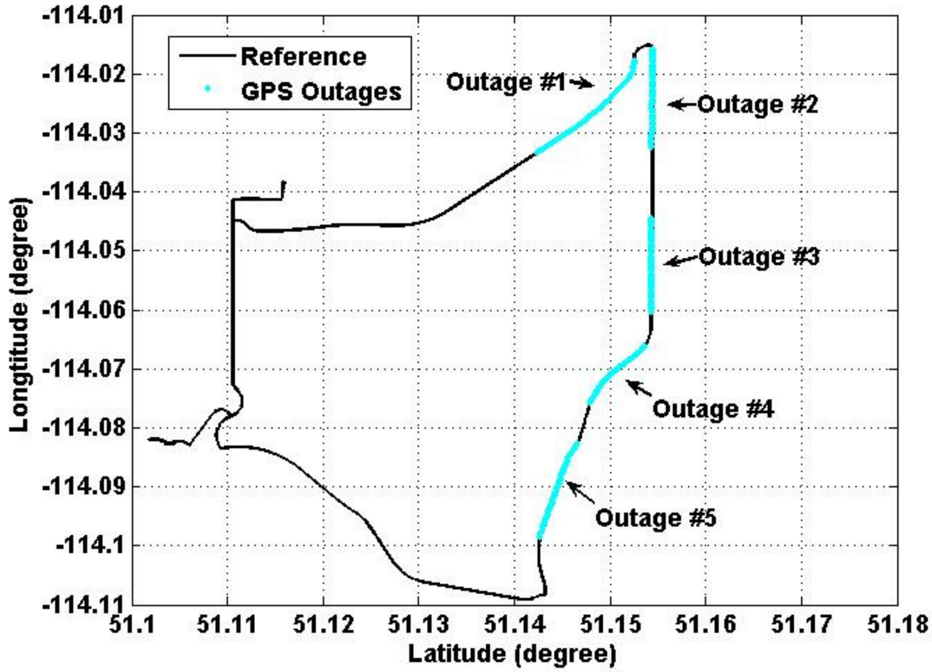

Figure 4.27 Reference Trajectory and GPS Outages in the 2nd Test

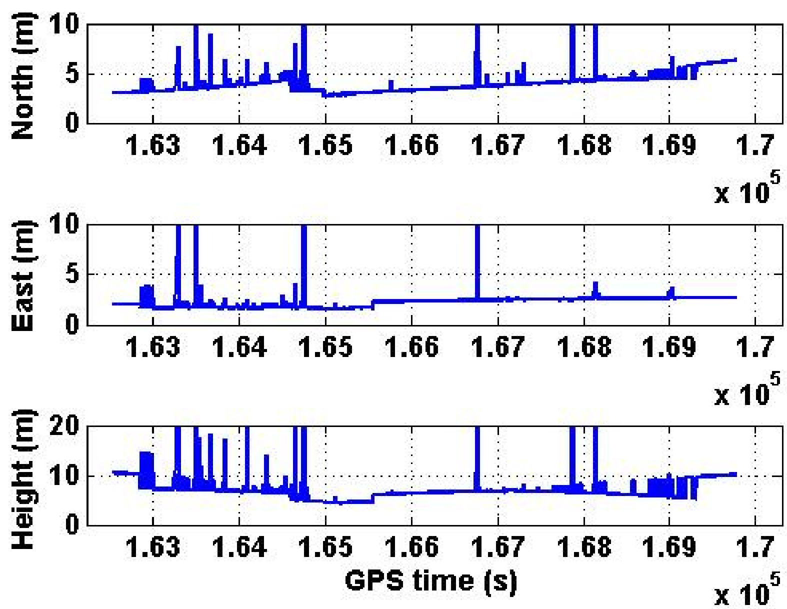

Figure 4.28 GPS SPP Accuracy in the 2nd Test

Table 4.4 Kalman Filter Process Noise Parameters in the 2nd Test

Tuned Parameters		
VRW	$0.660 m/s/\sqrt{hour}$	
ARW	$3.000 \deg/\sqrt{hour}$	
Gauss-Markov of Gyro Bias	$\sigma = 100 \deg/hour$	$T = 1hour$
Gauss-Markov of Acc Bias	$\sigma = 5000 mGal$	$T = 1hour$
Gauss-Markov of Gyro SF	$\sigma = 1000 PPM$	$T = 4hour$
Gauss-Markov of Acc SF	$\sigma = 1000 PPM$	$T = 4hour$

4.3.2 FKF Results of the 2nd Test

Since MEMS IMU were used in this test, static gyro compassing alignment step will fail to estimate the initial heading error. Therefore, the initial heading solution in the CIMU/GPS reference file is transferred to start the MEMS IMU/GPS FKF, while the initial roll and pitch are computed by levelling alignment. The initial positions are provided by the GPS measurements and the initial velocities are set to be zero. With five 60s GPS outages, the FKF results are illustrated in Figure 4.29-Figure 4.31, which show the FKF trajectory, the position and velocity errors with respect to the reference solutions, and the position and velocity STDs respectively.

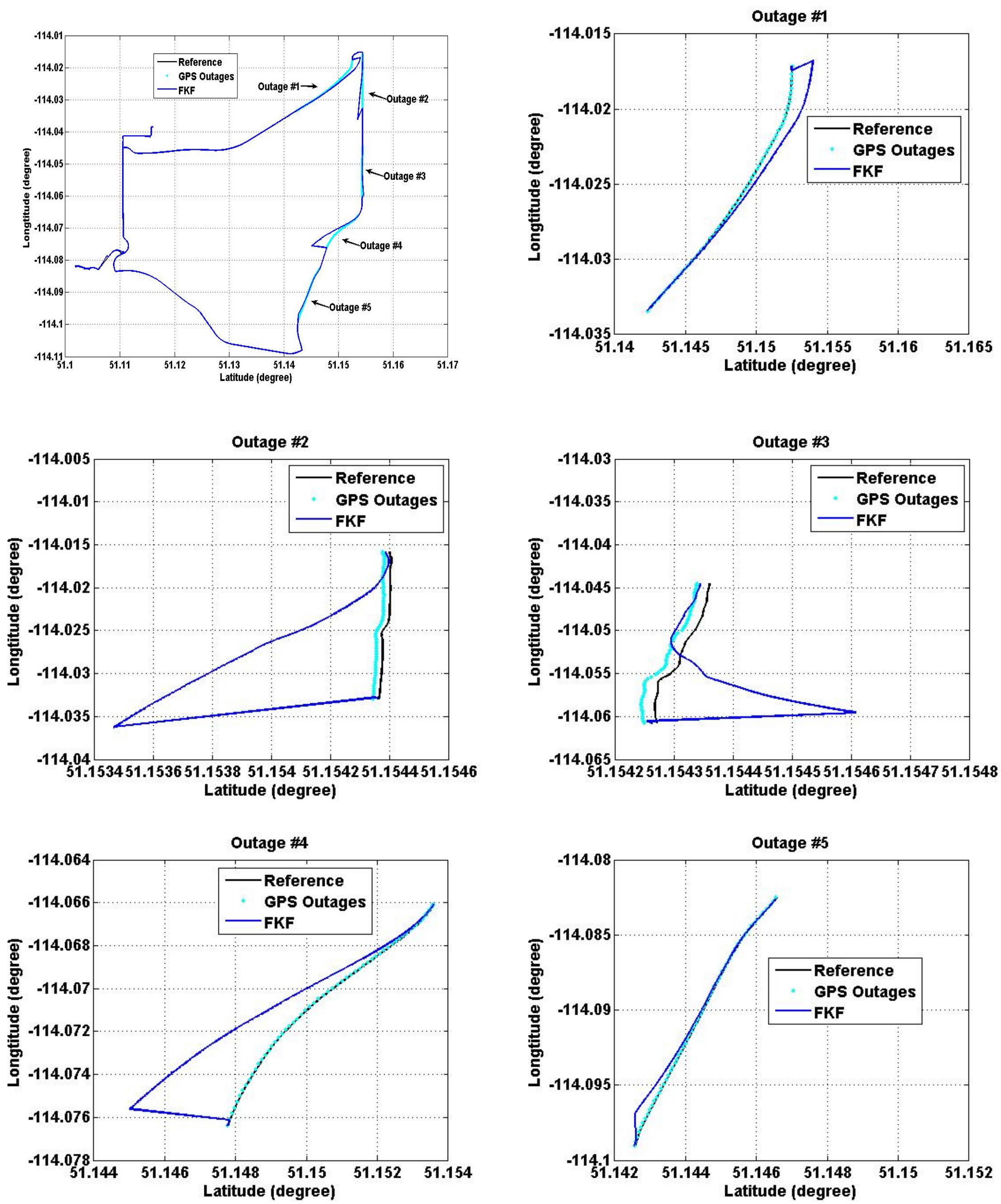

Figure 4.29 MEMS FKF Trajectory

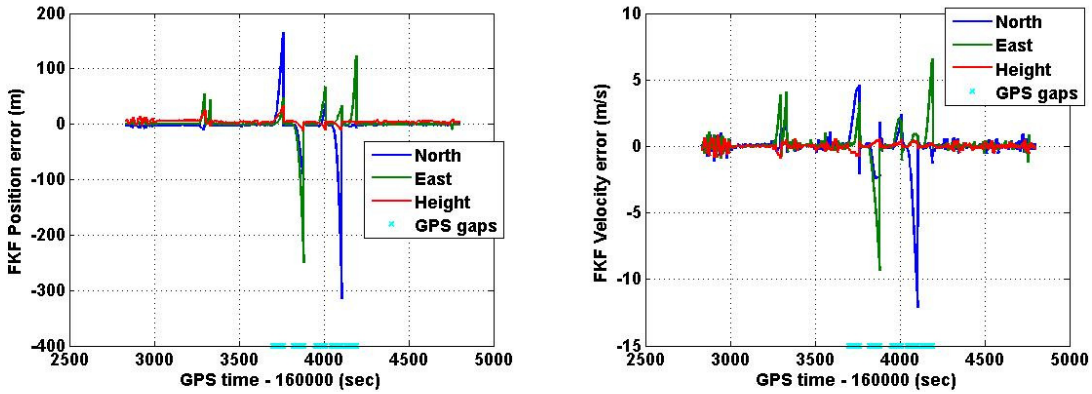

Figure 4.30 MEMS FKF Position and Velocity Errors

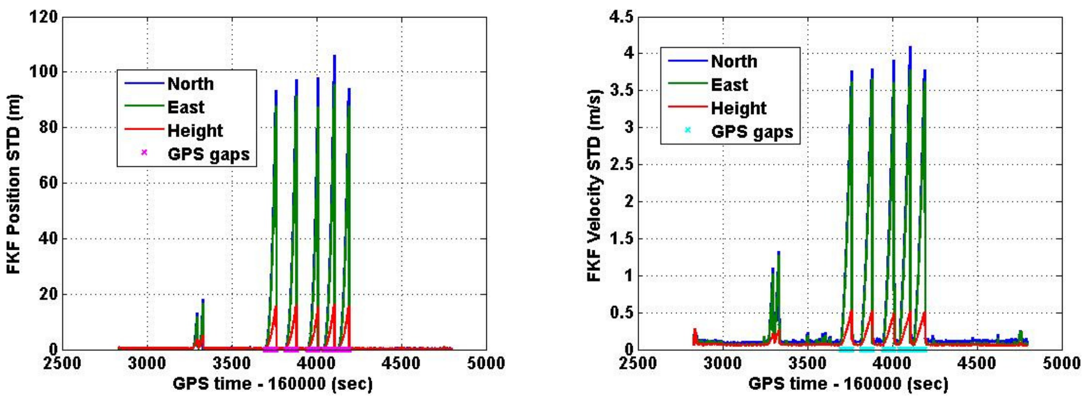

Figure 4.31 MEMS FKF Position and Velocity Error STDs

4.3.3 Smoothing Results of the 2nd Test

Figure 4.32 shows the TFS position and velocity errors across five GPS outages in the 2nd test. The corresponding position and velocity STDs are shown in Figure 4.33. It can be noted that while the horizontal position error is restricted to 5-meter level from 100-meter level, the height error is restricted to 5-meter level from 10-meter level by using TFS. The TFS trajectory and the RTSS processing results are included in Appendix B for reference.

The summary of the MEMS IMU FKF, TFS and RTSS results (maximum position errors) of the 2nd test is given in Table 4.5 corresponding to the five GPS outage periods. Note that the system here integrates GPS SPP (and not DGPS) with the MEMS IMU. The enhancement level of the positioning accuracy of the two smoothers is about 95.7% compared to the FKF results.

4.3.4 Effect of GPS Measurement Gap Length in the 2nd Test

Similar to the 1st test, 10s, 30s and 90s GPS outages are processed and analyzed in the second dataset. The figures to illustrate the measurement gap length effect refer to the Appendix B. The comparisons between different measurement gap lengths for FKF, TFS and RTSS in terms of the mean maximum 3-D position errors and the improvement levels are listed in Table 4.6. It can be noted that although the position errors rise as the outage length increases, the efficiency of both smoothers is upgrading with the increase of the GPS signal outage period length.

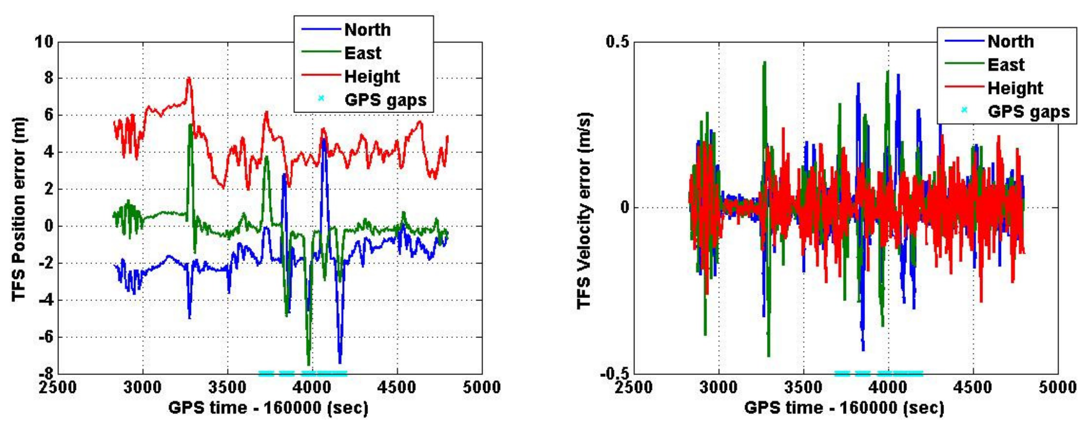

Figure 4.32 MEMS TFS Position and Velocity Errors

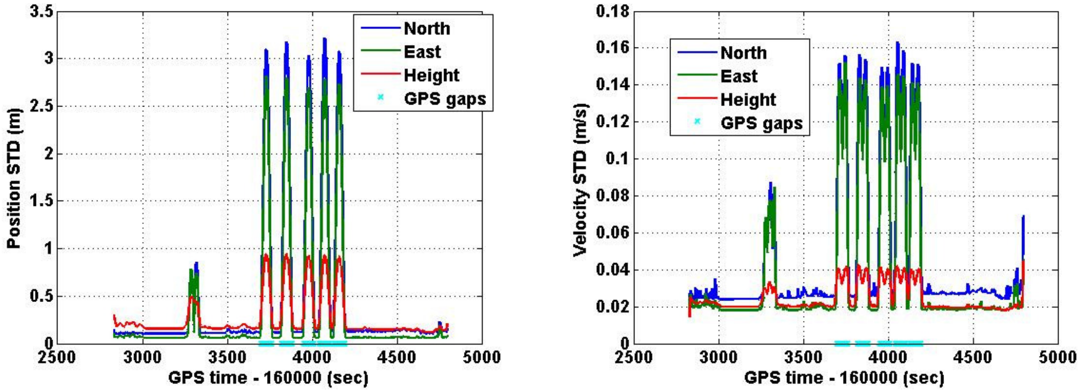

Figure 4.33 MEMS TFS Position and Velocity Error STDs

Table 4.5 MEMS Position Errors of FKF, TFS, and RTSS (60s Outage Length)

Outage	North(m)			East(m)			Height(m)			3 D (m)		
	FKF	TFS	RTS	FKF	TFS	RTS	FKF	TFS	RTS	FKF	TFS	RTS
#1	161.3	1.978	1.978	446.4	3.780	3.763	33.79	6.200	6.198	170.7	7.262	7.251
#2	97.96	4.685	4.682	240.8	4.886	4.886	12.00	4.774	4.775	260.3	6.207	6.205
#3	35.26	4.603	4.600	66.20	7.535	7.535	9.381	3.886	3.886	75.59	9.510	9.507
#4	303.1	4.741	4.752	32.92	2.961	2.965	10.90	5.352	5.352	305.1	7.617	7.624
#5	5.210	7.436	7.436	118.5	3.036	3.043	4.957	4.503	4.503	118.6	8.967	8.967
Mean	120.6	4.689	4.690	100.6	4.440	4.439	14.21	4.943	4.943	186.1	7.912	7.911

Table 4.6 MEMS 3-D Position Error and Smoothing Improvement Level Comparison between Different Outage lengths

Outage Length	Mean Maximum 3-D Position Error(m)			Improvement (%)	
	FKF	TFS	RTSS	TFS	RTSS
10s	6.599	4.313	4.313	34.6	34.6
30s	36.20	4.780	4.782	86.8	86.8
60s	186.1	7.912	7.911	95.7	95.7
90s	999.1	35.74	35.82	96.4	96.4

Chapter Five: OPTIMAL SMOOTHING FOR PIPELINE SURVEYS USING INTEGRATED INS/ODOM/CUPT SYSTEMS

5.1 Overview of Pipeline Surveys

Pipelines are constructed to transport or dispose liquid and gases, commonly operated by oil, gas, sewerage and chemical industries. The vast and complex underground network requires regular surveys to inspect, detect and isolate the damage along the pipelines (Hanna, 1990; Todd et al., 1990). Other than the frequent air scanning, Pipeline Inspection Gauges (PIG) are the alternative tools that can be sent through the pipelines to monitor the inside conditions. An example of the PIG is shown in Figure 5.1. The PIG is a torpedo shaped vehicle with red plastic rings/cups that fit tightly against the pipe wall. Behind the cups are the carrying wheels. In the figure, the thin wheels sticking at the back of the tool are the odometers (Kennedy, S., 2003).

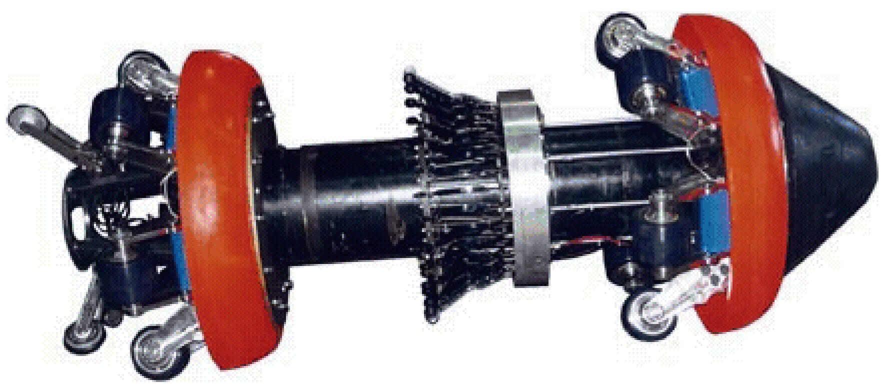

Figure 5.1 An Example of A PIG (Courtesy of BJ Pipeline Inspection Services)

The INS is employed to conduct the overall PIG navigation due to the unavailability of GPS inside the pipeline. Considering the pipeline size and the surveying accuracy requirement, IMUs with FOG gyros are typically used as the ideal surveying tools in this application. Aiding sensors are applied to compensate the growing errors induced by the stand-alone INS. Coordinate Updates (CUPT), also known as control point update, can be available along the pipeline, which usually exist several kilometres apart. These coordinates are always located at pipeline features (e.g. valves) or at Above Ground Markers (AGMs), of which the geodetic positions are precisely surveyed by DGPS (Shin and El-Sheimy, 2005). The tracking modules of control points detect the magnetic signals of the PIG and store the time when the PIG passes underneath them (Yu et al., 2005). Although the accuracy of CUPTs is violated by the uncertain lever-arm effect due to the time synchronization issue between the IMU and AGMs, currently most of the processed pipeline trajectories are forced to fit to these points (Kennedy, S., 2003).

Odometers (ODOMs) can provide the forward velocity information by differentiating the distance travelled by the PIG. Additionally, the measurement updating equations can be augmented with the non-holonomic constraints. The PIG is pushed in and driven through the pipeline by the differential pressure of medium flows like oil, gas or refined products. As a result, the PIG might experience some unexpected speed excursions when it is stuck due to mechanical failure or residue on the pipe wall (deposit solids from gases and waxes from oil), and suddenly re-pushed by the building up flow pressure (Kennedy, S., 2003; Allan and Hawes, 2005). Besides, the vibrations and the varying contacts between the odometer wheels and the pipe wall could increase the uncertainty in the velocity measurements.

The PIG sits stationary in the launch trap in the beginning of the surveying job, which provide the required time for INS initial alignment. While the PIG travels along the pipeline, the Data Acquisition System (DAS) on the PIG stores outputs from all the sensors, including IMU, odometers and other inspection tools, in real-time (Yu et al., 2005). The collected multi-sensor data are then processed in post mission to achieve the navigation solutions using filtering and smoothing methodologies. These solutions will provide the reference for both the pipeline trajectory and the leakage, blockage, and damage locations.

In this thesis, the performance of KF and optimal smoothers for pipeline surveys will be demonstrated using one real data set of the integrated INS/ODOM/CUPT system. The knowledge about the process model and the measurement models were discussed in the previous chapters.

5.2 Test Description

The PIG integrates a tactical-grade IMU (LN200), odometers and other inspection sensors. The sampling rates of the IMU and odometers are 100 Hz and 4 Hz respectively. The odometer-derived velocity measurement is shown in Figure 5.2. The PIG travelled slowly with a speed ranging from 0.2 m/s to 0.8m/s. Note that the noise level of the output is not obvious, which indicates the whole surveying process was under a benign vibration condition in a relatively clean pipeline. The bumps at 5 km after the PIG left the launching point illustrate that the PIG experienced speed excursions, induced by sharp pipe curves or the push by accumulated flow pressure at the unexpected blockages.

The PIG approximately travelled 32 km in about 21.4 hour. 12 GPS-derived coordinates were provided along the whole survey route, of which the first CUPT point corresponds to the starting survey point (distance 0.0m). Each of the travelled distance (calculated by odometer data) and time separations between the adjacent CUPTs are listed in Table 5.1. The pipeline route linearly interpolated by the CUPTs is illustrated in Figure 5.3.

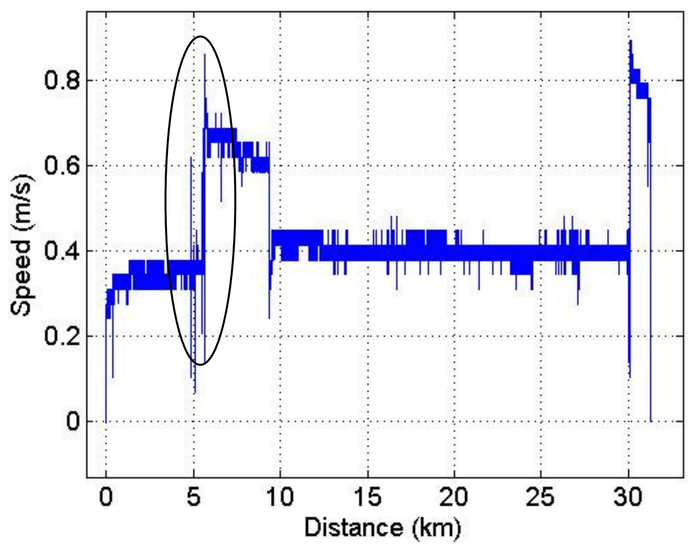

Figure 5.2 PIG Velocity Measurement from Odometer

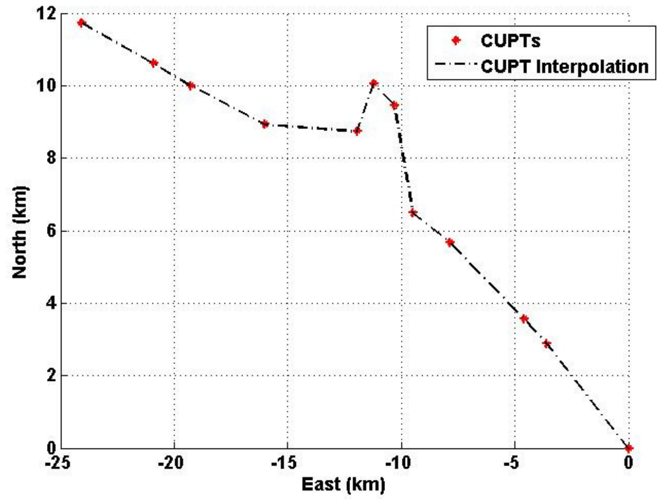

Figure 5.3 Surveying Route Interpolated by CUPTs

Table 5.1 Time and Distance Separation between CUPTs

CUPTs	Time Separation (min)	Distance (m)
#1	0	0
#2	238	4770
#3	48	1239
#4	111	3913
#5	73	1818
#6	149	3599
#7	55	1337
#8	65	1564
#9	185	4414
#10	148	3439
#11	74	1755
#12	121	3389

5.3 Results

The IMU data was processed using KF with the aiding from CUPTs and odometer-derived velocity measurements. Since the PIG stayed stationary at the launching trip in the first 300s before being pushed into the pipeline, analytic coarse alignment associated with fine alignment was applied to initialize the attitude. The first GPS-derived coordinate provided the initial positions, and the initial velocity is set to be zero. The tuned sensor parameters for the process covariance matrix and the measurement covariance matrix are listed in Table 5.2.

Table 5.2 Kalman Filter Noise Parameters

Tuned Parameters		
VRW	$0.015 m/s/\sqrt{hour}$	
ARW	$0.15 \deg/\sqrt{hour}$	
Gauss-Markov of Gyro Bias	$\sigma = 1 \deg/hour$	$T = 4 hour$
Gauss-Markov of Acc Bias	$\sigma = 300 mGal$	$T = 4 hour$
Gauss-Markov of Gyro SF	$\sigma = 100 PPM$	$T = 4 hour$
Gauss-Markov of Acc SF	$\sigma = 300 PPM$	$T = 4 hour$
CUPT STD	$0.5 m$	
Odometer STD	$0.05 m/s$	

The INS/ODOM/CUPT integration results will be discussed and analyzed in the following order,

- Pipeline Surveying Forward Kalman Filter (FKF)

- Two Filter Smoother (TFS)
- RTS Smoother (RTSS)

5.3.1 FKF Results

Figure 5.4 shows the forward filtering trajectory and the zoomed regions compared to the route interpolated by CUPTs (i.e. the reference). Note that the filtering positioning errors diverged before being restricted by the control points. For example, the horizontal positioning error increases to 278.3m before it reaches the second CUPT, while it is reduced to 1.569m afterwards. This improvement can be further checked by the FKF height estimation with respect to the CUPT interpolation in Figure 5.5. These errors are calculated by subtracting the FKF position estimations from the corresponding reference coordinates at control points. The difference between FKF positioning results and the CUPT interpolation is shown in Figure 5.6 for a rough evaluation of the filtering performance during intervals without the aiding of control points. Note that since the CUPTs are linearly interpolated to obtain the north, east, and height coordinates, the interpolation route can hardly reveal the actual pipeline trajectory in field and are provided as approximate reference. Since the stand-alone INS positioning errors could reach tens of kilometres within one hour (El-Sheimy, 2007; Shin and El-Sheimy, 2005), the hundred-meter level divergence in Figure 5.6 indicates that the odometer-derived velocities as well as the non-holonomic constraints keep the filtering trajectory straight and effectively restrict the unaccepted position error accumulation.

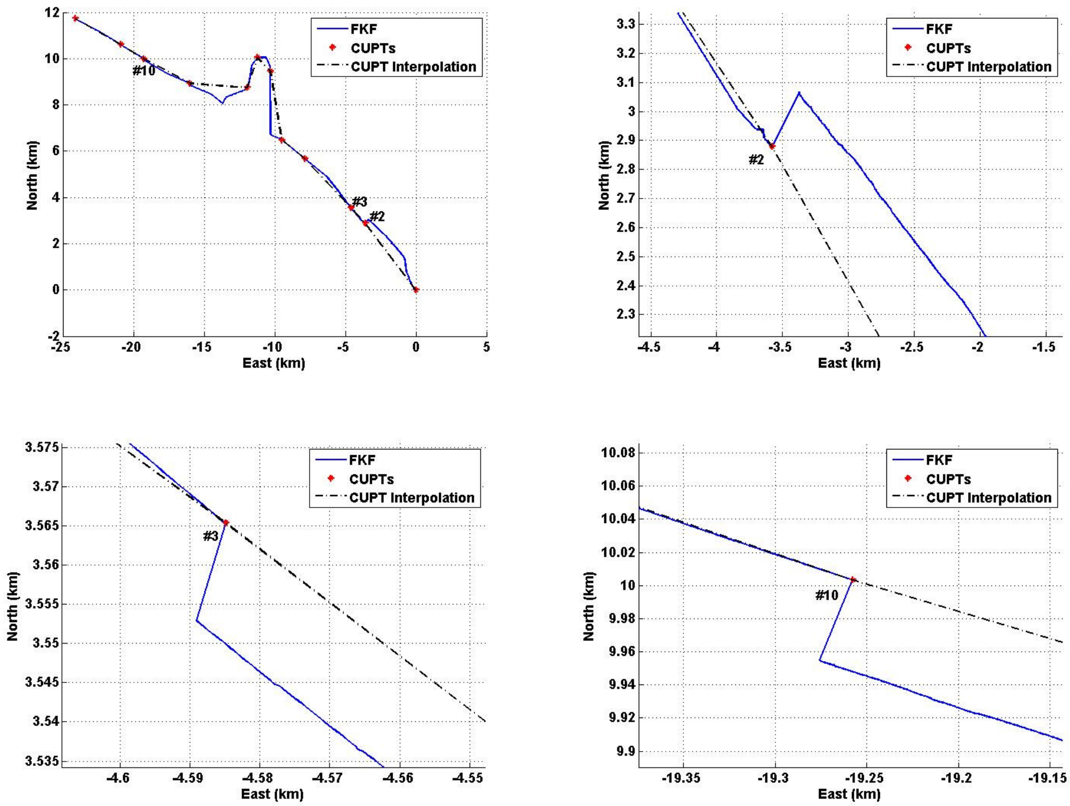

Figure 5.4 FKF Trajectory

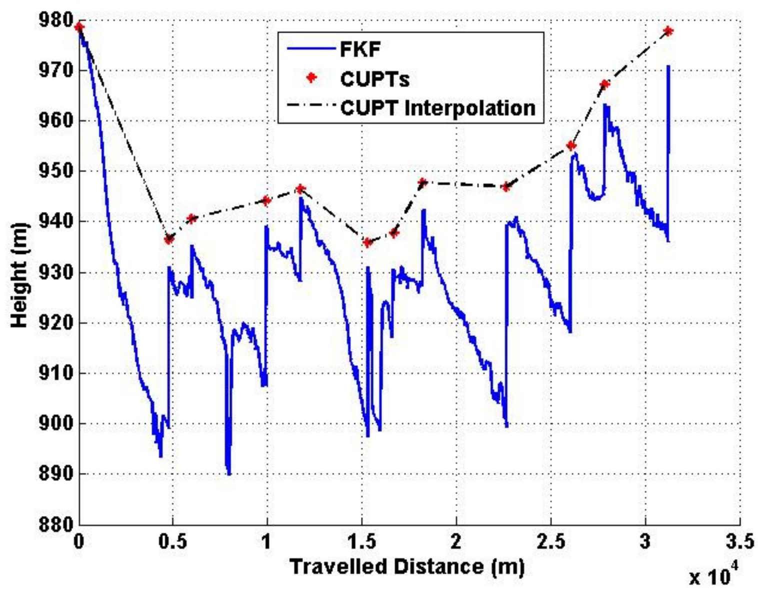

Figure 5.5 FKF Height Estimation

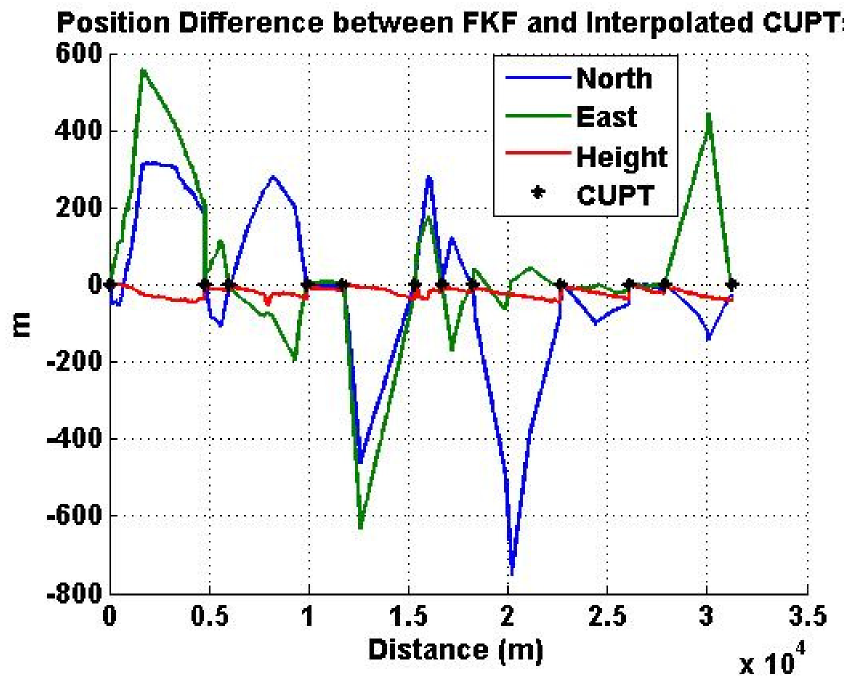

Figure 5.6 Positioning Difference between Filtering and CUPT Interpolation

The FKF velocity estimation results as well as the odometer-derived speed are shown in Figure 5.7, which indicate that the PIG proceeded in the pipeline slowly and stably except for some speed excursions in the up direction.

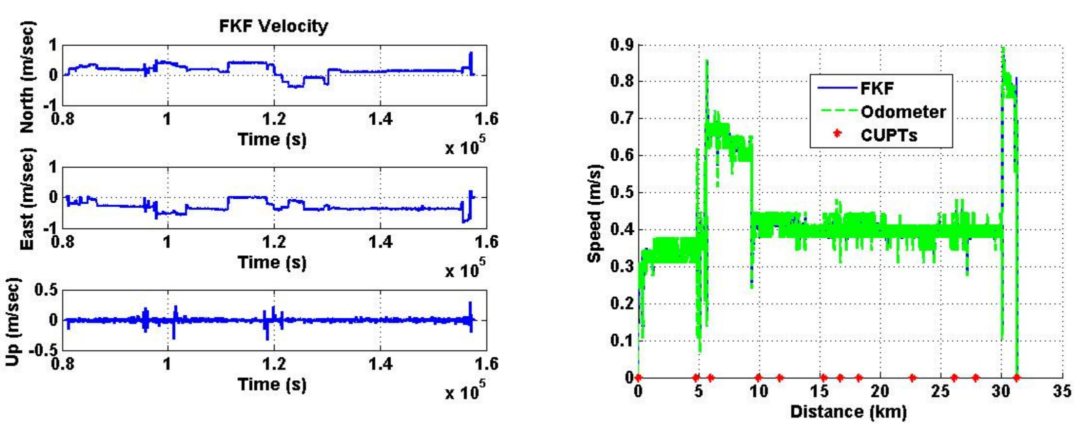

Figure 5.7 FKF Velocity Estimation

Figure 5.8 shows the FKF attitude of the PIG, the bump at the beginning in the pitch figure indicates that the PIG experienced a sharp jump about 30 degrees. This occurred when the PIG was pushed down from the launching trip into the pipeline by the flows during a short time interval. Further, irregular and trembling roll angles could be observed within -50 degrees as the PIG travelled through the pipeline.

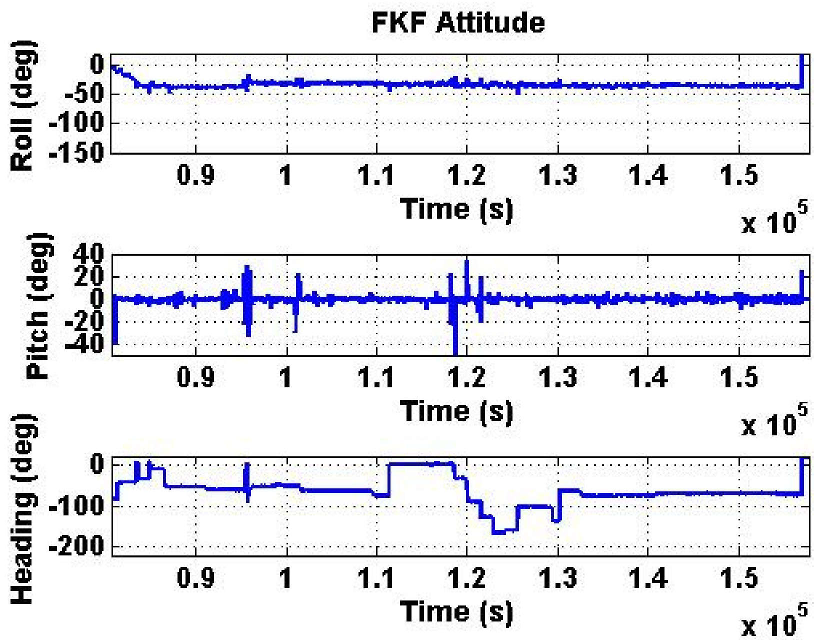

Figure 5.8 FKF Attitude Estimation

5.3.2 TFS Results

The plane trajectory estimations by the TFS as well as the associated BKF are shown in Figure 5.9. The height estimation is shown in Figure 5.10. Similar to FKF results, the BKF trajectory diverged from the reference coordinates before it reached the control points, in the reverse directions. The positioning errors are effectively restricted by smoothing. Note that the TFS horizontal positioning error is reduced to 2.85m before it reaches the 10th CUPT compared to 51.8m in FKF and 55.6m in BKF, while the height error is reduced to 9.5 m compared to -36.6m in FKF and 21.9m in BKF. A further 3-D trajectory illustration of this improvement is shown in Figure 5.11.

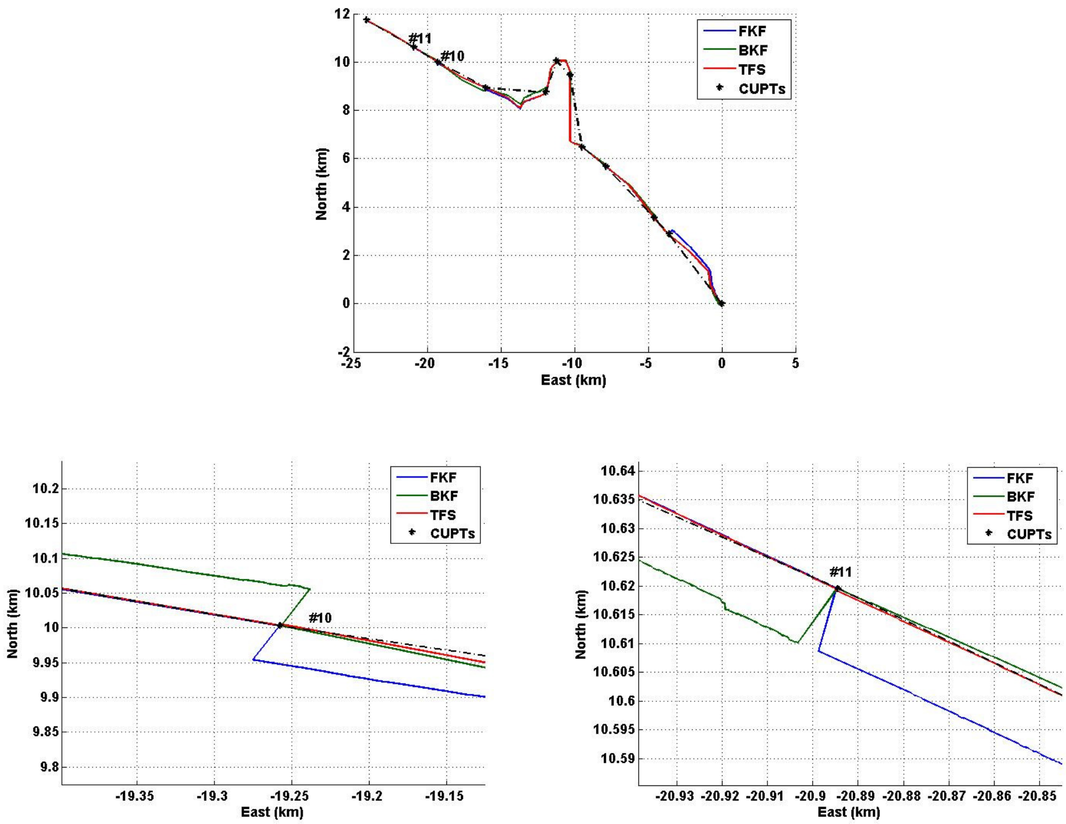

Figure 5.9 TFS and BKF Trajectory

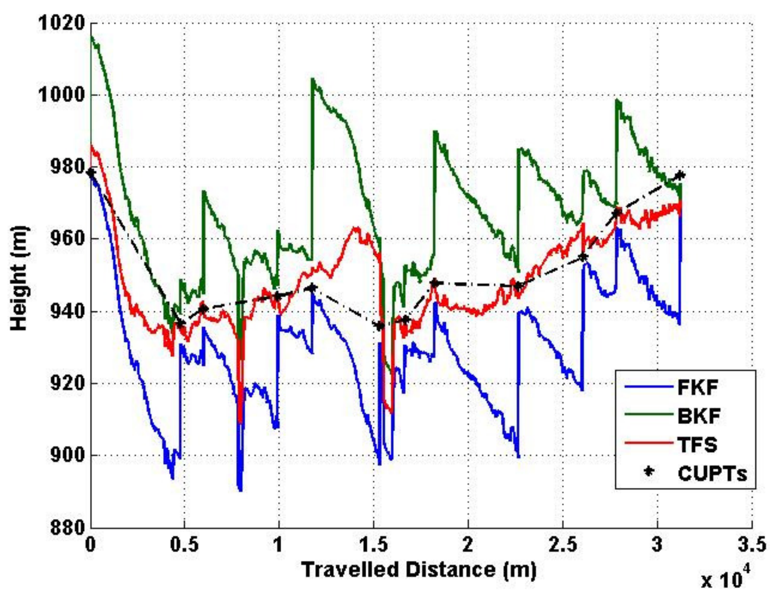

Figure 5.10 TFS and BKF Height Estimation

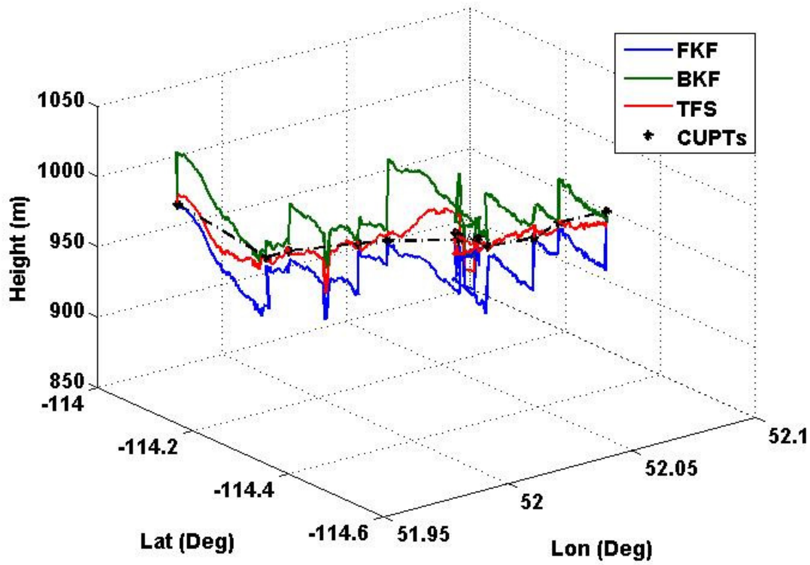

Figure 5.11 TFS and BKF 3-D Trajectory

5.3.3 RTSS Results

The RTSS trajectory compared to FKF and the CUPT interpolation is shown in Figure 5.12 including the zoomed regions. The height estimation and 3-D trajectory are shown in Figure 5.13 and Figure 5.14 subsequently. Similar to the TFS results, the RTSS significantly improves the positioning estimation over forward filtering.

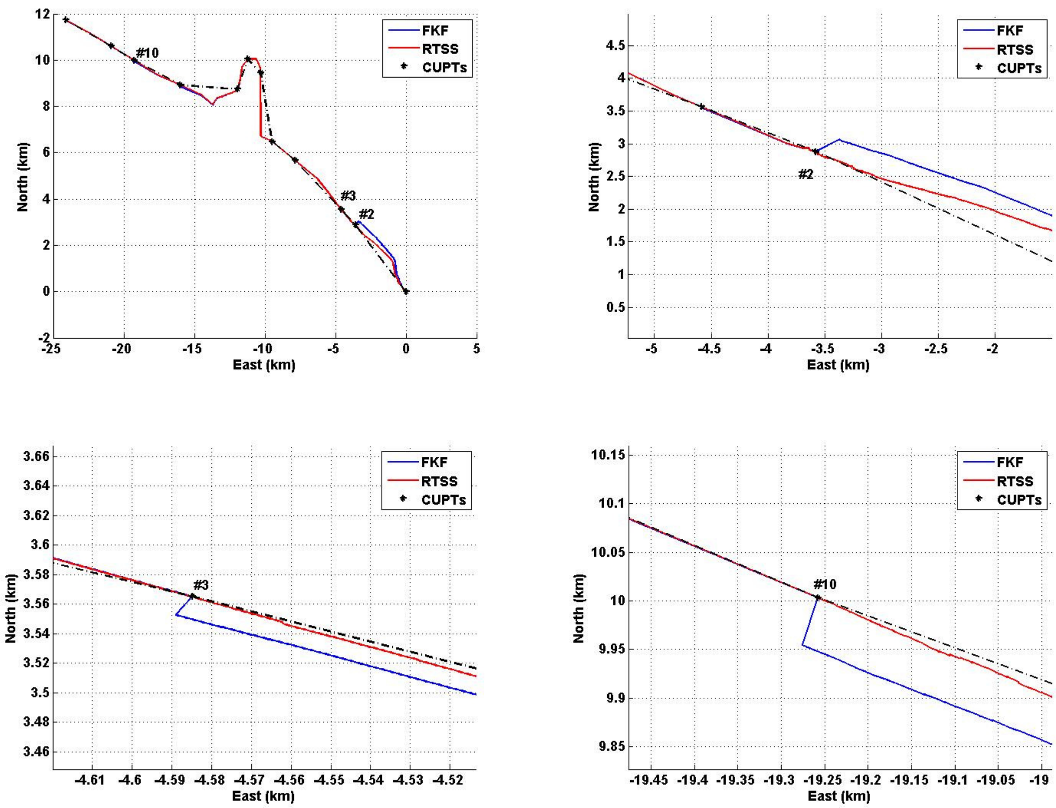

Figure 5.12 RTSS Trajectory

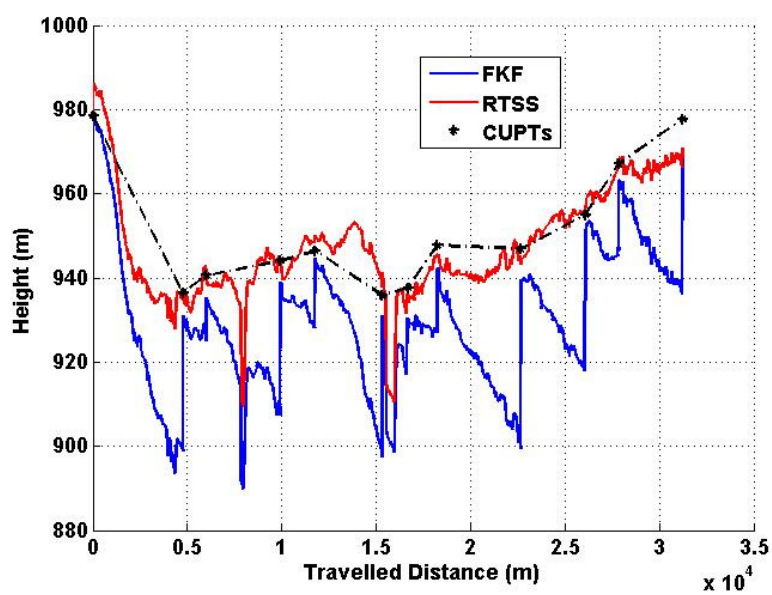

Figure 5.13 RTSS Height Estimation

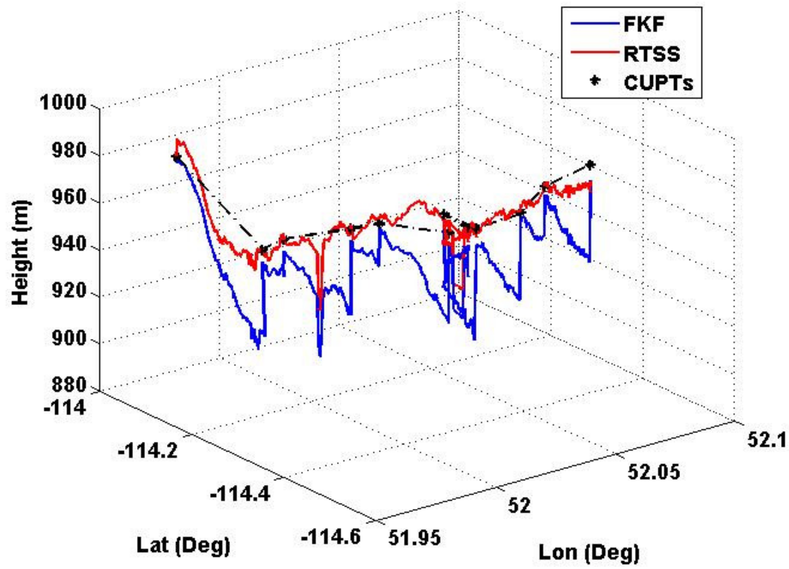

Figure 5.14 RTSS 3-D Trajectory

5.3.4 Comparison

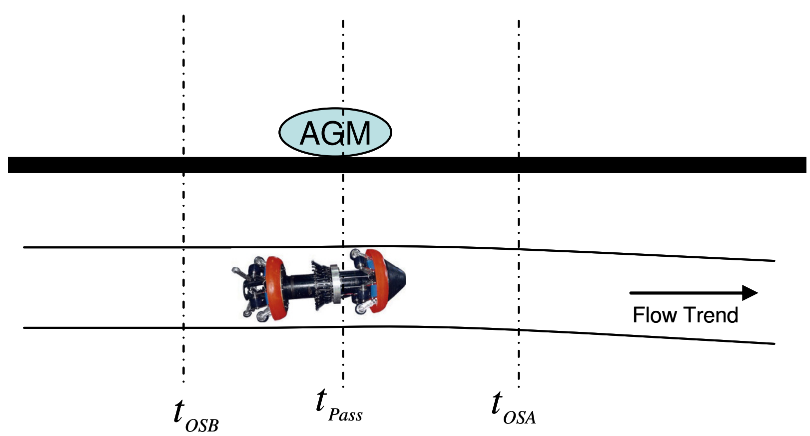

Figure 5.15 Time Epochs when the PIG Passes an AGM

As depicted in Figure 5.15, the passing time of the PIG under an AGM is between two data output time epochs, including the time one sample before (OSB) and the time one sample after (OSA) (Yuksel, 2008). Table 5.3 listed the computed OSB and OSA position errors of the forward filtering, including north, east, height, horizontal (2-D) and

3-D, by subtracting the filtering results from the corresponding reference coordinates at control points. Similarly, the position errors of BKF, TFS and RTSS are summarized in Table 5.4-Table 5.6. In addition, illustrations of the 2-D and 3-D errors are shown in Figure 5.16–Figure 5.17 respectively.

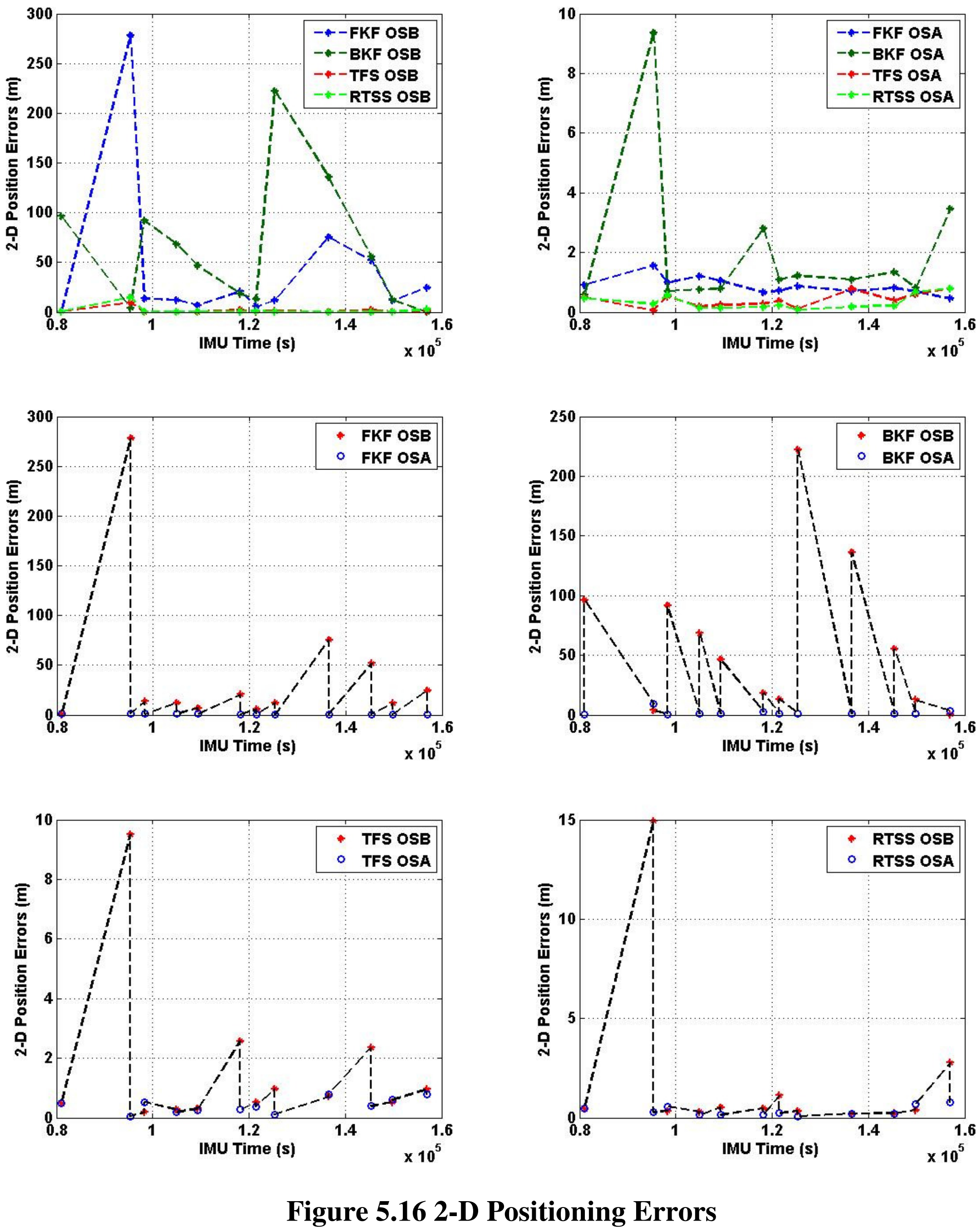

Figure 5.16 2-D Positioning Errors

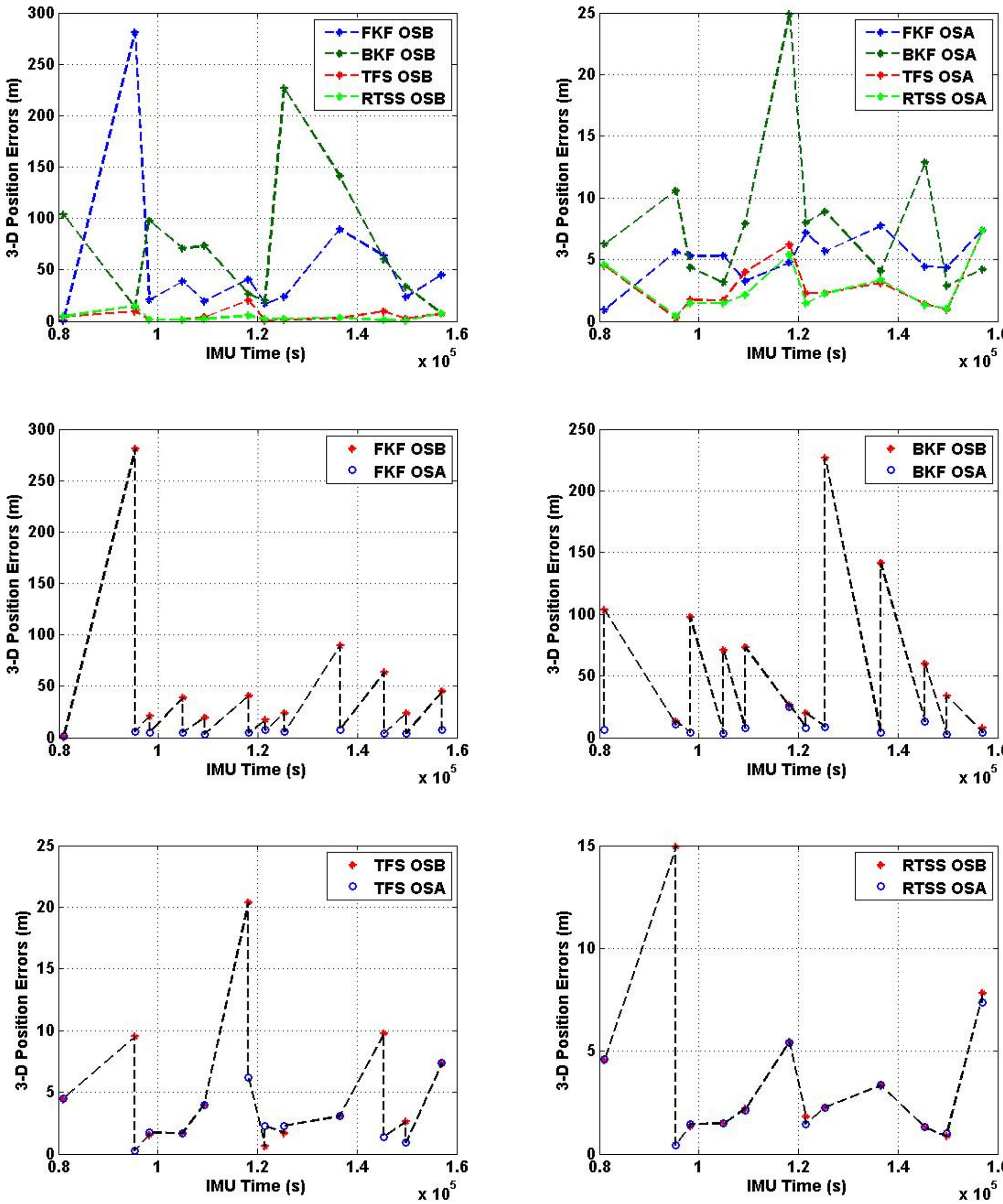

Figure 5.17 3-D Positioning Errors

The comparison between the errors indicates that the position errors can be effectively restricted by the coordinate updates. Further, the divergence of the navigation errors in FKF and BKF are substantially improved by both smoothing algorithms. The smoothing efficiency of TFS is nearly 90.0% according to the 3-D OSB errors compared to the filtering results, while the improvement level of RTSS is nearly 92.9%. The smoothing effect of the TFS is nearly 42.3% according to the OSA 3-D errors compared to the filtering solution, while the improvement level of RTSS is nearly 48.0%.

Note that the smoothers improved the position errors during GPS outages by 95.4% in the first test and 95.7 % in the second test as shown in Chapter 4, which are greater than those in this test. Further, the enhancement efficiencies of TFS and RTSS in this test are not exactly the same. However, with the consideration of the fact that the coordinate measurement updates in vehicle navigation application are much more sufficient than those in pipeline navigation, both TFS and RTSS can be accepted as the effective smoothing methodologies in the application of pipeline surveys, and their smoothing efficiency are comparable to each other.

Additionally, the height errors are greater than in horizontal directions, after they are restricted by the CUPTs and further smoothed by TFS and RTSS. This is mainly due to the longer lever-arms in the vertical direction than in the horizontal plane between the above ground markers and the passing PIG inside the underground pipeline. On the other hand, referring to the velocity and pitch estimations in Section 5.3.1, the PIG experienced some sudden jumps, speed excursions and continuous trembling velocity in the up direction, which could increase the height uncertainty and jeopardize its estimation accuracy.

Table 5.3 FKF Positioning Errors

	North		East		Height		2-D		3-D	
	OSB	**OSA**	**OSB**	**OSA**	**OSB**	**OSA**	**OSB**	**OSA**	**OSB**	**OSA**
#1	-0.081	-0.095	0.782	0.906	-0.045	-0.021	0.787	0.911	0.788	0.911
#2	186.9	-0.817	206.2	1.334	-35.54	-5.410	278.3	1.565	280.5	5.632
#3	-13.00	-0.673	-3.392	0.729	-15.67	-5.188	13.44	0.992	20.64	5.282
#4	-10.54	-0.594	6.647	1.046	-36.62	-5.162	12.46	1.203	38.68	5.301
#5	-5.514	-0.497	3.825	0.927	-18.13	-3.058	6.711	1.052	19.33	3.234
#6	-1.113	-0.656	-20.58	-0.083	-35.25	-4.705	20.61	0.662	40.83	4.751
#7	-5.413	0.437	-1.752	0.577	-16.10	-7.138	5.610	0.724	17.08	7.174
#8	-3.364	0.704	11.52	0.499	-20.55	-5.608	12.00	0.863	23.80	5.674
#9	-74.57	-0.269	-11.52	0.651	-47.55	-7.703	75.45	0.704	89.19	7.735
#10	-48.94	-0.360	-17.05	0.729	-36.60	-4.363	51.83	0.812	63.45	4.438
#11	-11.25	-0.319	-3.367	0.617	-20.33	-4.293	11.74	0.695	23.48	4.349
#12	-24.60	-0.416	-2.621	0.190	-38.06	-7.369	24.74	0.458	45.40	7.383
Mean	32.11	0.486	24.10	0.691	26.70	5.001	42.81	0.887	55.27	5.155

Table 5.4 BKF Positioning Errors

	North		East		Height		2-D		3-D	
	OSB	OSA	OSB	OSA	OSB	OSA	OSB	OSA	OSB	OSA
#1	-54.04	0.212	-79.56	0.546	37.71	6.217	96.18	0.585	103.3	6.244
#2	3.918	-7.623	-0.175	-5.438	12.44	4.956	3.922	9.364	13.05	10.59
#3	80.46	-0.247	44.47	0.659	32.71	4.311	91.93	0.704	97.58	4.368
#4	62.94	0.012	26.67	0.763	18.09	3.036	68.35	0.763	70.70	3.131
#5	34.42	0.031	31.43	0.782	56.65	7.882	46.61	0.783	73.36	7.921
#6	12.10	-1.723	13.79	2.223	19.11	24.70	18.34	2.812	26.49	24.86
#7	-4.714	0.547	12.26	0.949	14.73	7.916	13.13	1.096	19.73	7.991
#8	222.0	1.214	-13.29	0.177	42.20	8.796	222.4	1.226	226.3	8.881
#9	-130.7	-0.440	-38.18	1.004	37.91	3.895	136.2	1.096	141.3	4.047
#10	51.82	-0.070	20.16	1.335	21.89	12.80	55.60	1.337	59.75	12.87
#11	-9.918	-0.332	-7.797	0.739	30.98	2.750	12.62	0.810	33.45	2.866
#12	-0.234	-3.378	0.187	-0.794	-7.468	-2.375	0.299	3.471	7.474	4.205
Mean	55.60	1.319	24.00	1.284	27.66	7.469	63.79	2.004	72.71	8.164

Table 5.5 TFS Positioning Errors

	North		East		Height		2-D		3-D	
	OSB	**OSA**	**OSB**	**OSA**	**OSB**	**OSA**	**OSB**	**OSA**	**OSB**	**OSA**
#1	0.205	0.208	-0.428	-0.444	4.412	4.458	0.475	0.490	4.437	4.485
#2	-7.489	-0.017	-5.849	0.049	0.374	0.229	9.503	0.052	9.510	0.235
#3	0.018	0.349	0.190	-0.389	-1.505	-1.624	0.191	0.523	1.517	1.706
#4	-0.025	0.163	0.275	-0.098	-1.647	-1.679	0.276	0.190	1.670	1.689
#5	-0.273	-0.083	0.147	-0.227	3.980	3.968	0.310	0.241	3.992	3.975
#6	-0.422	0.273	2.540	0.020	20.21	6.184	2.575	0.274	20.37	6.190
#7	-0.355	-0.347	0.378	0.136	-0.301	-2.252	0.519	0.372	0.600	2.282
#8	0.702	0.094	-0.666	-0.061	1.386	-2.274	0.968	0.112	1.691	2.277
#9	-0.717	-0.617	-0.106	-0.485	-2.989	-3.006	0.725	0.785	3.076	3.107
#10	2.096	0.386	1.056	0.033	9.481	1.353	2.347	0.388	9.767	1.408
#11	-0.403	0.011	-0.349	-0.597	-2.562	0.736	0.534	0.598	2.617	0.946
#12	-0.953	0.616	-0.023	0.501	-7.280	-7.318	0.953	0.794	7.342	7.361
Mean	1.138	0.264	1.001	0.253	4.677	2.923	1.615	0.402	5.549	2.972

Table 5.6 RTSS Positioning Errors

	North		East		Height		2-D		3-D	
	OSB	**OSA**	**OSB**	**OSA**	**OSB**	**OSA**	**OSB**	**OSA**	**OSB**	**OSA**
#1	0.202	0.202	-0.400	-0.414	4.524	4.574	0.448	0.461	4.546	4.597
#2	-11.65	0.204	-9.337	0.186	0.293	0.292	14.93	0.276	14.93	0.402
#3	-0.333	0.126	-0.062	-0.553	-1.293	-1.331	0.339	0.567	1.337	1.447
#4	-0.188	-0.003	0.229	-0.145	-1.443	-1.475	0.296	0.145	1.473	1.482
#5	-0.317	-0.128	0.418	0.044	2.127	2.115	0.525	0.135	2.191	2.119
#6	-0.276	0.169	-0.380	-0.007	5.413	5.408	0.470	0.169	5.433	5.411
#7	-1.057	-0.151	-0.379	-0.173	-1.438	-1.426	1.121	0.230	1.823	1.445
#8	0.350	-0.064	0.008	-0.055	-2.228	-2.229	0.350	0.084	2.255	2.231
#9	-0.043	0.039	0.208	-0.174	-3.317	-3.334	0.212	0.178	3.323	3.339
#10	-0.112	0.177	0.205	-0.115	1.275	1.286	0.234	0.211	1.296	1.303
#11	-0.283	-0.147	-0.281	-0.652	0.767	0.755	0.399	0.668	0.864	1.008
#12	2.517	0.615	1.161	0.501	-7.317	-7.318	2.772	0.793	7.824	7.361
Mean	1.444	0.169	1.089	0.252	2.619	2.629	1.841	0.326	3.941	2.679

* The mismatches between the OSB results of TFS and RTSS at certain control points are caused by the algorithm numerical stability during implementations.

Chapter Six: OPTIMAL SMOOTHING FOR HORIZONTAL/VERTICAL BUILDING SURVEYS USING INTEGRATED INS/ZUPT/CUPT SYSTEMS

6.1 Introduction to Building Surveys

Location Based Services (LBS) triggered the growing demands of indoor/outdoor navigations in urban areas. Navigation and surveying of public and residential buildings can be one of the promising LBS applications with great potentials. The databases containing precisely surveyed positioning information are essentially helpful for public safety, convenience, emergency route guidance, and personal tracking (Singh, 2006; MacGougan, 2003).

However, GPS positioning accuracy suffers from the faded signal power and multipath effect in urban or indoor environments. This inadequacy drives the emergence of various indoor positioning techniques. Among them, the most significant include high-sensitivity GPS (HSGPS) and assisted-GPS (AGPS), which are designed to improve tracking and acquisition of low-power GPS signals (Watson, 2005). Another commonly researched technique is wireless location such as utilizing WiFi signals by fingerprinting or proximity methods (O'Keefe, 2008). This technique is recommended to be applied in areas where sufficient wireless access points are deployed reasonably, such as public libraries, hospitals, business buildings, research parks and so forth.

Gyros and accelerometers can be used in indoor navigation systems as supplements or alternatives. The potential success of indoor navigation systems with MEMS inertial sensors could contribute to great investment opportunities for mini unmanned vehicles, portable navigation devices, and individual guidance devices. The feasibility has partially been researched by assessing the performance of INS-based Pedestrian Navigation Systems (PNS) (Godha et al., 2006; Syed, 2009).

The absence of GPS updates and the time-dependent error behaviour of INS call for the external aiding information. Zero Velocity Updates (ZUPTs) are efficient and feasible for indoor navigations, since the carriers would likely experience frequent stops. ZUPTs with appropriate time durations and intervals effectively limit the growing velocity errors, slowing down the positioning errors and providing the chances to evaluate the sensor bias and attitude errors (El-Sheimy, 2007; Huddle, 1998). Moreover, CUPTs are indispensable for stand-alone INS to control the fast growing positioning errors. Control points can be fixed separately at certain frequently passed locations around buildings by conventional surveying techniques. In the sequel, the IMU measurements associated with the corresponding aiding information will be post-processed to obtain the navigation solutions using both filters and smoothers.

In this Chapter, two building surveying tests conducted by one of the ENGO 500 Project Groups at the Department of Geomatics Engineering (UofC) will be utilized to evaluate the indoor/outdoor navigation performance of filters and smoothers on integrated INS/ZUPT/CUPT systems. Tactical-grade IMU (Litton LN200) was used in both tests.

The objective of the first test was to evaluate the horizontal navigation quality along the fixed route around some buildings at U of C with predetermined CUPT points inside and outside them. On the other hand, the second test aimed at evaluating the height estimation quality in a 7-floor campus elevator with the relative height of each floor measured by a total station. The vertical positioning information will be useful for safety monitoring of lifts in underground mining operations as well as recreational applications (Martell, 1991; Skaloud and Schwarz, 2000). GPS solutions were available while outdoor for both tests (where precise initial alignment was achieved). Frequent ZUPTs were added during both tests with intentionally chosen time durations and intervals. A cart installed with equipment including LN200, NovAtel OEM4 GPS receiver, laptops and other necessary hardware were used to collect the data of both tests. More details on these tests can be found in Isackson et al (2008).

6.2 Description and Results of the First Test

6.2.1 Horizontal Test Description

Before the horizontal test, a conventional traverse survey was performed to place 7 control points inside the basements of and outside the Engineering Complex at the U of C campus (See Figure 6.1 and Figure 6.2). Two Alberta Survey Control Markers (ASCMs), 263079 and 26252, were used to provide Universal Transverse Mercator (UTM) coordinates. The traverse started south from ASCM 263079 where three outside control points were placed. The 4th to 7th control points were placed in the basement of the Engineering Complex. The coordinate values of the traverse points in both UTM and

WGS84 are listed in Table 6.1. Note that height coordinates were not provided in this test since it aims to evaluate the horizontal navigation quality only.

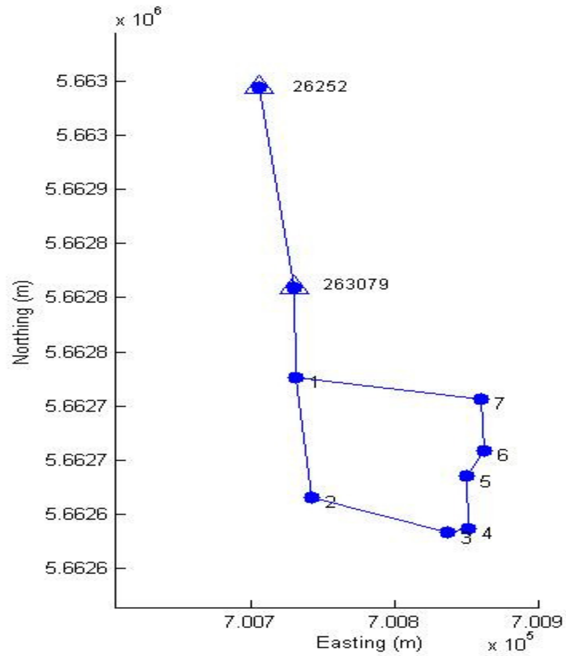

Figure 6.1 Points of the Traverse in UTM Coordinates (Zone 11)
(After Isackson et al., 2008)

The equipment on the cart (See Figure 6.2) was left stationary for more than 10 minutes for GPS signal acquisition and INS initial alignment. The procedure of the horizontal testing was conducted along the reverse route. The test started from Point #1 to #7. It continued along the basement passing Point #6, #5, #4 and exited the Engineering building at Point #3. After exiting the building and regaining satellite observations, the cart was carried down the stairs and continued north back along the surveyed route from Point #3 to Point #2 until reaching the beginning control point (Isackson et al., 2008). Note that the GPS signals are intentionally blocked during this time interval while data processing to simulate the indoor environment. Also, another 10 minute static observations were recorded at the end of the survey. Twenty one ZUPTs, among which six happened at the ground control points from Point #7 to Point #2 (Each lasted for about one minute; See the green rows in Table 6.2), were implemented.

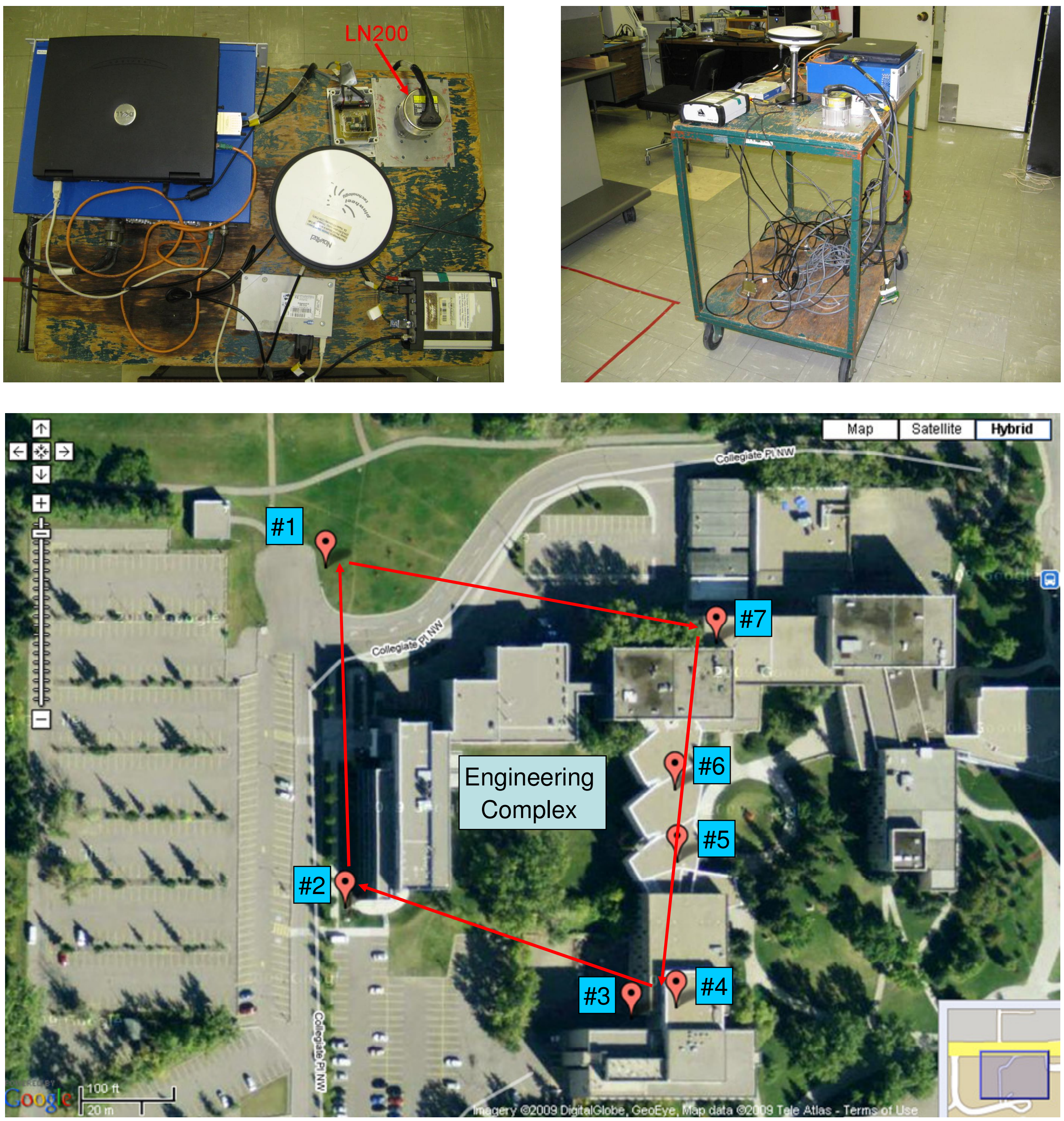

Figure 6.2 Horizontal Testing Equipment and Route (Courtesy of Google)

Table 6.1 Traverse Control Point Coordinates (After: Isackson et al., 2008)

Point	UTM Zone 11		WGS84					
	Northing (m)	Easting (m)	Latitude (° ' ")			Longitude (° ' ")		
1	5662726.691	700731.313	51	04	51.175	114	08	2.777
2	5662616.010	700741.973	51	04	47.583	114	08	2.451
3	5662583.347	700837.085	51	04	46.407	114	07	57.634
4	5662587.373	700851.430	51	04	46.519	114	07	56.890
5	5662635.169	700850.177	51	04	48.066	114	07	56.859
6	5662659.228	700862.281	51	04	48.829	114	07	56.189
7	5662706.688	700859.918	51	04	50.366	114	07	56.215

Table 6.2 Horizontal Testing ZUPTs (After: Isackson et al., 2008)

ZUPT(#)	Start GPS Time (s)	End GPS Time (s)	Duration (s)
1	333876.01	334962.566	1087
2	334987.116	335002.226	15
3	335029.487	335042.557	13
4	335067.957	335082.677	15
5	335108.928	335123.768	15
6	335159.109	335214.529	55
7	335241.48	335257.36	16
8	335282.11	335337.291	55
9	335364.382	335416.942	53
10	335441.993	335496.204	54
11	335522.874	335577.145	54
12	335616.916	335676.637	60
13	335708.617	335731.638	23
14	335758.528	335772.298	14
15	335797.189	335814.769	18
16	335838.689	335856.04	17
17	335880.52	335894.81	14
18	335910.08	335966.391	56
19	335992.092	336007.732	16
20	336033.912	336052.683	19
21	336089.653	336108.034	18

6.2.2 Horizontal Test Results

The accumulated systematic position errors due to initial value errors and determinant accelerometer biases over short time intervals are highly correlated to the velocity errors (Skaloud and Schwarz, 2000). Because of this correlation, approximately 75-80% of position errors over a short travel period can be removed with the aid by ZUPTs (Huddle, 1998). The residual errors in navigation-grade INS are mainly caused by white noise and will accumulate with the square root of stop number if regular ZUPT time durations and intervals are chosen (Huddle, 1998). However, the exclusive use of ZUPTs is limited by the inability to estimate the acceleration-dependent errors (e.g. accelerometer scale factor), since the integrated acceleration between two stops sums up to zero by a constant error (Skaloud and Schwarz, 2000).

The research on INS system observability demonstrated a strong coupling effect exiting between tilt errors and horizontal velocities (Bar-Itzhack and Berman, 1988). Hence, the observed velocity errors during ZUPTs are capable of providing accurate estimations of roll, pitch and the associated horizontal gyro drifts (Grejner-Brzezinska et al., 2001). Conversely, the weak observability of heading error by velocities as well as the lack of dynamics during static periods leads to the uncontrolled azimuth and the vertical gyro drift (Godha et al., 2006). Unfortunately, the azimuth error is one of the primary factors contributing to the positioning divergence. As a result, external information, from CUPTs in this case, is required to observe and estimate the uncompensated residuals induced by acceleration-dependent and azimuth errors when using ZUPTs only. The errors can be further restricted and removed by backward smoothing in post-mission. The horizontal indoor navigation dataset will be processed in the order of INS-Only, INS/ZUPT, INS/CUPT, and INS/ZUPT/CUPT for performance evaluation under different integration strategies. Then, both filtering and smoothing results of FKF, TFS and RTSS will be discussed and analyzed.

INS-Only

The INS-Only trajectories including forward filtering, TFS, and RTSS are shown in Figure 6.3. It can be observed that the forward filtering diverged after the GPS measurements became unavailable, i.e. near Point #7. Meanwhile, neither TFS nor RTSS could improve the filtering performance. Note that the DGPS solutions were only available at the beginning part (raw data processed by Waypoint GrafNav/GrafNet™ software from NovAtel Inc). Therefore, without the external aiding, the long-term stand-alone INS results cannot meet the indoor navigation requirements.

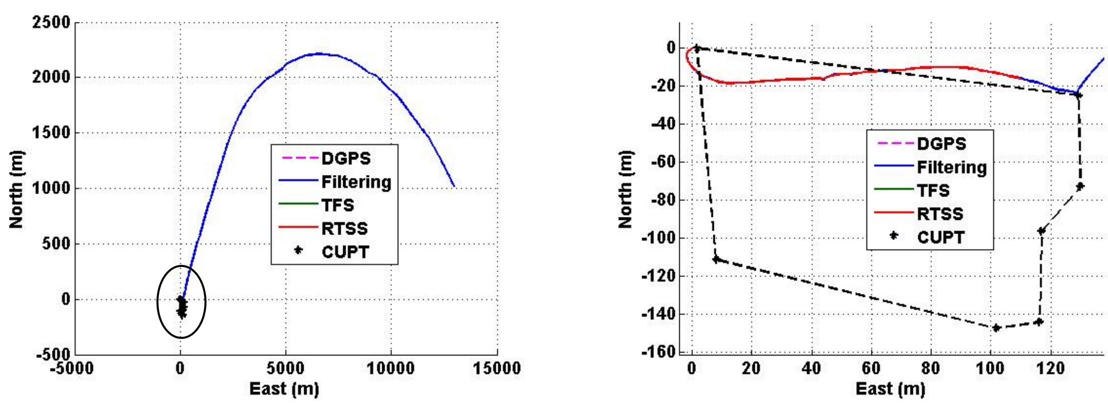

Figure 6.3 INS-Only Trajectories

INS/CUPT

Figure 6.4 shows the INS/CUPT trajectories of forward filtering, TFS and RTSS. Similar to the discussions in Section 5.3.4, the positioning displacement between the estimation results and the corresponding reference coordinates at the control point will be calculated in terms of both the time one sample before (OSB) the CUPT and the time one sample after (OSA) the CUPT. Table 6.3 lists the OSB position errors of forward filtering TFS and RTSS, with respect to north, east, and 2-D. Table 6.4 lists the OSA position errors. The 2-D position errors are illustrated in Figure 6.5.

The results indicate that without the ZUPT aiding, the filtering position errors obtained by stand-alone INS increased rapidly with time to hundred-meter level before restricted by the coordinate updates. Further, TFS and RTSS substantially improved the positioning accuracy both during CUPT-free gaps and at control points.

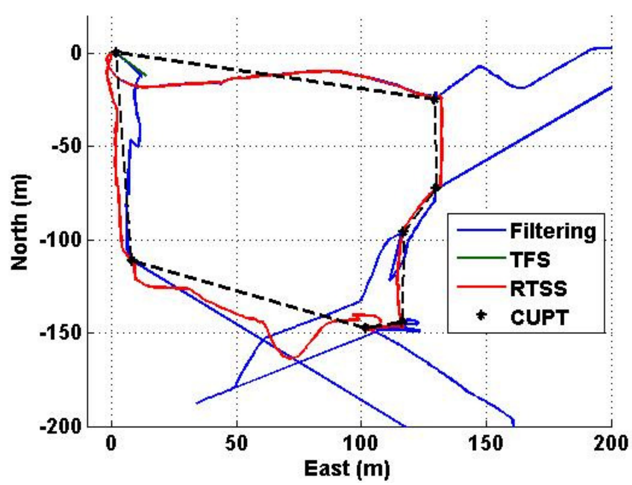

Figure 6.4 INS/CUPT Trajectories

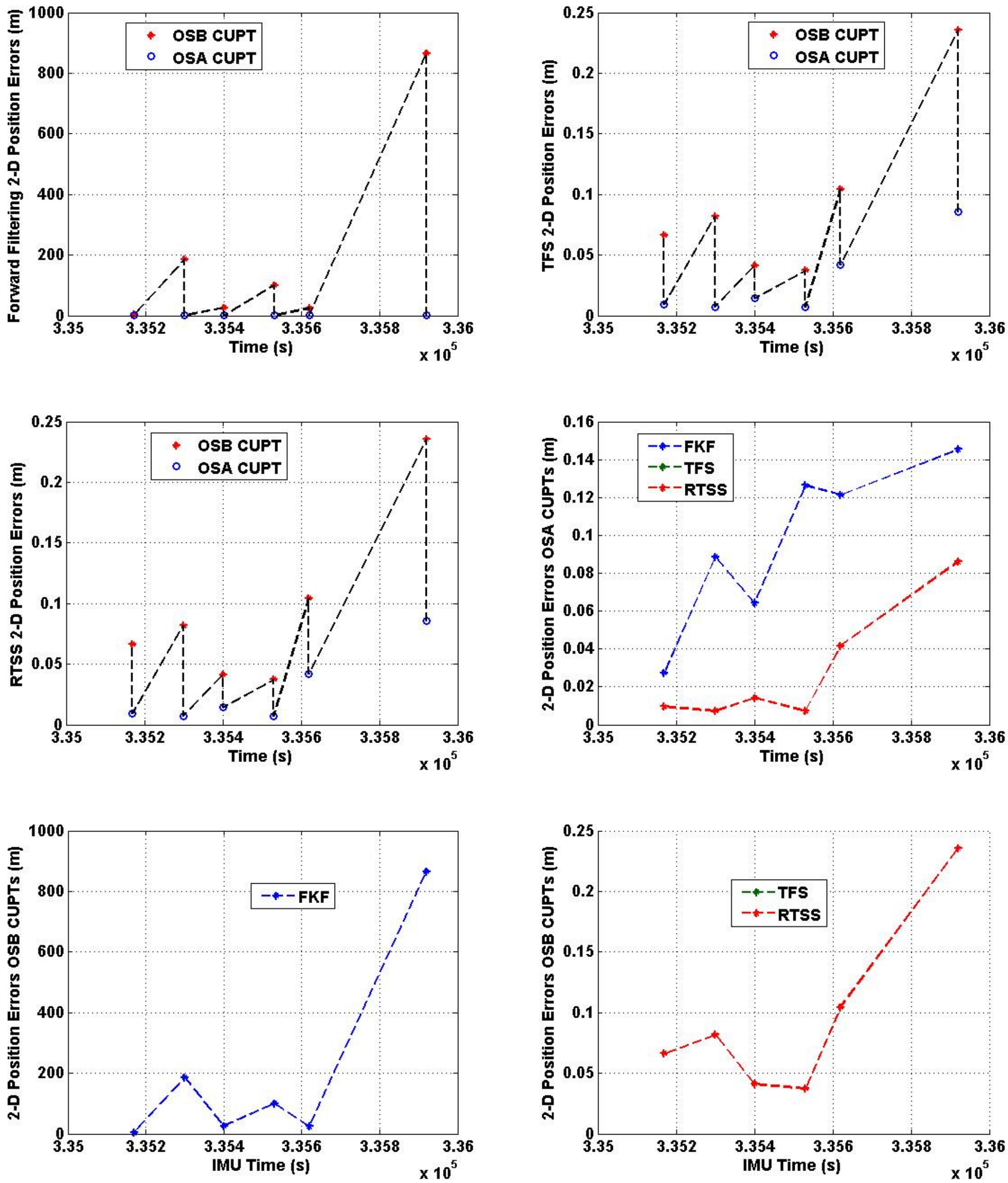

Figure 6.5 INS/CUPT 2-D Position Errors

Table 6.3 INS/CUPT Position Errors One Sample Before (OSB) Control Points

Control Point	North(m)			East(m)			2-D (m)		
	FKF	**TFS**	**RTSS**	**FKF**	**TFS**	**RTSS**	**FKF**	**TFS**	**RTSS**
#7	3.922	0.0463	0.0463	0.2675	0.0476	0.0475	3.931	0.0664	0.0664
#6	107.1	-0.0435	-0.0435	151.9	-0.0692	-0.0692	185.9	0.0817	0.0817
#5	-25.52	-0.0205	-0.0205	-6.085	-0.0356	-0.0356	26.24	0.0411	0.0411
#4	-43.49	0.0030	0.0030	-89.80	0.0373	0.0373	99.78	0.0374	0.0374
#3	-1.578	0.0595	0.0595	23.92	0.0858	0.0857	23.98	0.1044	0.1044
#2	-516.2	0.2058	0.2058	693.7	-0.1143	-0.1143	864.7	0.2354	0.2355
Abs Mean	116.3	0.0631	0.0631	161.0	0.0650	0.0649	200.8	0.0944	0. 0944

Table 6.4 INS/CUPT Position Errors One Sample After (OSA) Control Points

Control Points	North(m)			East(m)			2-D (m)		
	FKF	**TFS**	**RTSS**	**FKF**	**TFS**	**RTSS**	**FKF**	**TFS**	**RTSS**
#7	0.0256	0.0068	0.0068	0.0101	-0.0066	-0.0066	0.0275	0.0095	0.0095
#6	-0.0830	-0.0055	-0.0055	-0.0307	-0.0049	-0.0049	0.0885	0.0073	0.0073
#5	-0.0313	-0.0068	-0.0068	-0.0560	-0.0124	-0.0124	0.0641	0.0141	0.0141
#4	0.0534	-0.0003	-0.0003	0.1146	0.0072	0.0072	0.1264	0.0072	0.0072
#3	-0.0492	0.0243	0.0244	0.1109	0.0339	0.0339	0.1213	0.0416	0.0418
#2	0.1357	0.0826	0.0826	-0.0521	-0.0240	-0.0240	0.1454	0.0860	0.0860
Abs Mean	0.0630	0.0211	0.0211	0.0624	0.0148	0.0148	0.0955	0.0277	0.0277

INS/ZUPT

The INS/ZUPT trajectories are shown in Figure 6.6. Apparently, frequent ZUPTs helped to control the filtering horizontal error drifts around ten-meter level throughout the entire surveying process. As discussed previously, without the external aiding like CUPTs, the exclusive use of ZUPTs is unable to estimate the acceleration-dependent errors and the weak observable heading errors. The visible translational displacement between estimated trajectories and control points (as shown in the zoomed figure) shows the consequence of these limitations. The position errors in terms of the time “AT” the control points (different from the aforementioned OSA since a time interval of ZUPT existed at each of the points) are calculated by subtracting the INS/ZUPT estimations from the corresponding reference coordinates, which are listed in Table 6.5. The comparison between filtering and smoothing manifests that the aiding from velocity updates could not help optimal smoothing to provide notable improvement over filtering. On the contrary, the filtering performance even outweighs the TFS by checking the absolute mean errors.

INS/CUPT/ZUPT

Figure 6.7 depicted the INS/CUPT/ZUPT trajectories of forward filtering, TFS and RTSS. It indicates that this integration gains the merits of the two strategies analyzed earlier (i.e. CUPTs & ZUPTs). With frequent ZUPTs, the filtering position errors are effectively controlled during the CUPT-free intervals. On the other hand, the CUPTs lead the estimation trajectory to converge towards the control points, which mitigates the notable translational displacement in Figure 6.6. Table 6.6 and Table 6.7 list the position errors OSB and AT the control points respectively. By checking the mean 2-D position errors, the improvement level by TFS is nearly 66.4% while it is 55.7% by RTSS.

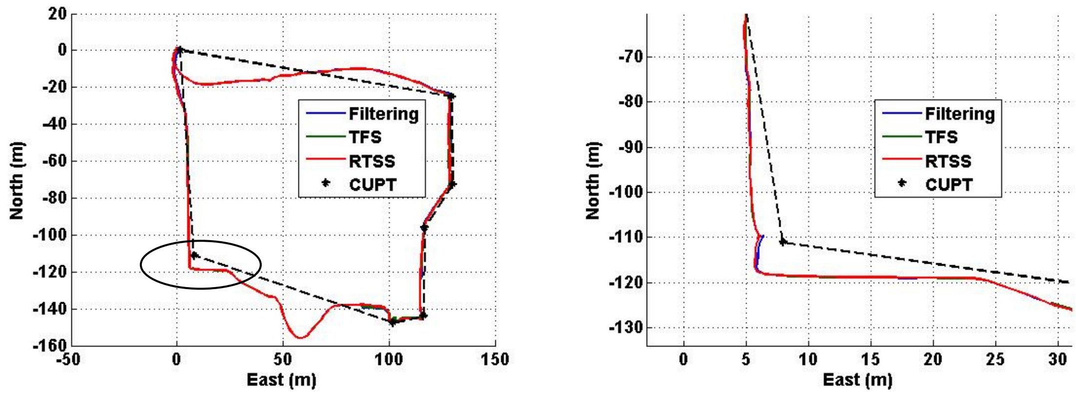

Figure 6.6 INS/ZUPT Trajectories

Table 6.5 INS/ZUPT Position Errors AT Control Points

Control Point	North(m)			East(m)			2-D (m)		
	FKF	TFS	RTSS	FKF	TFS	RTSS	FKF	TFS	RTSS
#7	-0.458	-1.030	-0.862	-1.198	-1.581	-1.463	1.283	1.887	1.698
#6	-1.122	-1.158	-0.724	-2.063	-2.308	-1.610	2.349	2.582	1.765
#5	-0.206	-0.134	-0.271	-0.265	-0.202	-0.401	0.336	0.242	0.484
#4	-0.349	-0.223	-0.426	-1.002	-0.949	-1.103	1.061	0.974	1.182
#3	1.567	1.702	1.095	-1.746	-1.712	-1.723	2.346	2.414	2.041
#2	1.271	1.241	1.241	-1.976	-2.043	-2.075	2.350	2.310	2.417
Abs Mean	0.829	0.915	0.770	1.375	1.466	1.396	1.621	1.748	1.598

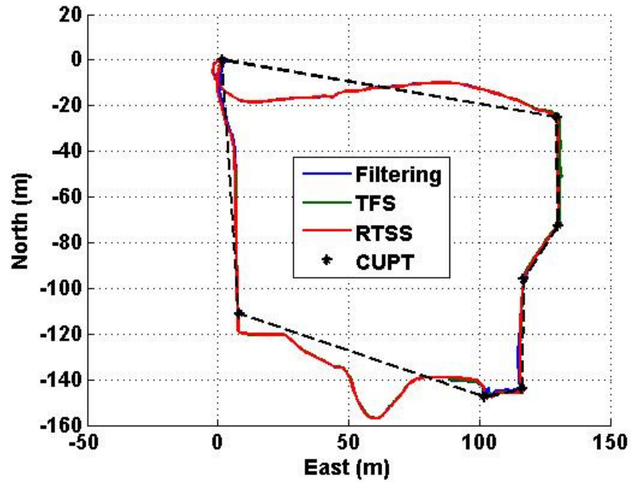

Figure 6.7 INS/CUPT/ZUPT Trajectories

Table 6.6 INS/CUPT/ZUPT Position Errors OSB Control Points

Control Point	North(m)			East(m)			Horizontal(m)		
	FKF	TFS	RTS	FKF	TFS	RTS	FKF	TFS	RTS
#7	-0.3934	0.0543	-0.0424	-1.1696	-0.0391	-0.0847	1.2340	0.0669	0.0948
#6	0.1418	-0.0079	-0.0016	-0.0827	-0.0143	-0.0037	0.1642	0.0164	0.0040
#5	0.6957	0.0082	0.0047	1.2651	0.0172	0.0110	1.4438	0.0190	0.0120
#4	-0.2099	-0.0278	-0.0080	-0.7426	-0.0032	-0.0009	0.7717	0.0280	0.0081
#3	2.0378	0.0448	0.0107	-0.6014	0.0226	-0.0087	2.1247	0.0502	0.0138
#2	0.1987	-0.0002	0.0004	-0.1794	-0.0012	-0.0021	0.2677	0.0012	0.0022
Abs Mean	0.6129	0.0239	0.0113	0.6735	0.0163	0.0185	1.0010	0.0303	0.0225

Table 6.7 INS/CUPT/ZUPT Position Errors AT Control Points

Control Point	North(m)			East(m)			Horizontal(m)		
	FKF	TFS	RTS	FKF	TFS	RTS	FKF	TFS	RTS
#7	0.0910	-0.0134	-0.0273	0.0785	-0.0322	-0.0584	0.1202	0.0349	0.0645
#6	0.0046	-0.0116	-0.0026	0.0346	-0.0075	-0.0097	0.0349	0.0138	0.0100
#5	-0.017	0.0008	0.0032	-0.0173	0.0075	0.0089	0.0243	0.0076	0.0095
#4	-0.010	-0.0137	-0.0077	0.0046	0.0018	0.0009	0.0114	0.0138	0.0077
#3	-0.028	-0.0017	0.0051	0.0093	0.0006	0.0008	0.0299	0.0018	0.0052
#2	0.0026	-0.0014	-0.0018	0.0031	0.0035	0.0020	0.0041	0.0037	0.0027
Abs Mean	0.0257	0.0071	0.0079	0.0246	0.0089	0.0135	0.0375	0.0126	0.0166

Comparison between Different Integration Strategies

The positioning accuracy of the horizontal test under different integration strategies can further be explained by the north position covariance information, as shown in Figure 6.8. The first plot indicates that the filtering position estimation by stand-alone INS degrades rapidly with time before being constrained by coordinate updates. At the same time, backward smoothing significantly improves the positioning accuracy over filtering. The second plot denotes that frequent ZUPT aiding restricts the position STD within 5 meters throughout the process, which is a notable overall improvement compared to the INS/CUPT results. However, it can be observed that the position accuracy keeps degrading with time and the smoothing cannot efficiently limit or remove this divergence. This demonstrates the fact that the residual position errors after the ZUPT corrections will remain and accumulate. The last plot shows that INS/CUPT/ZUPT integration can include the merits of both the two aiding sources and achieve a superior performance.

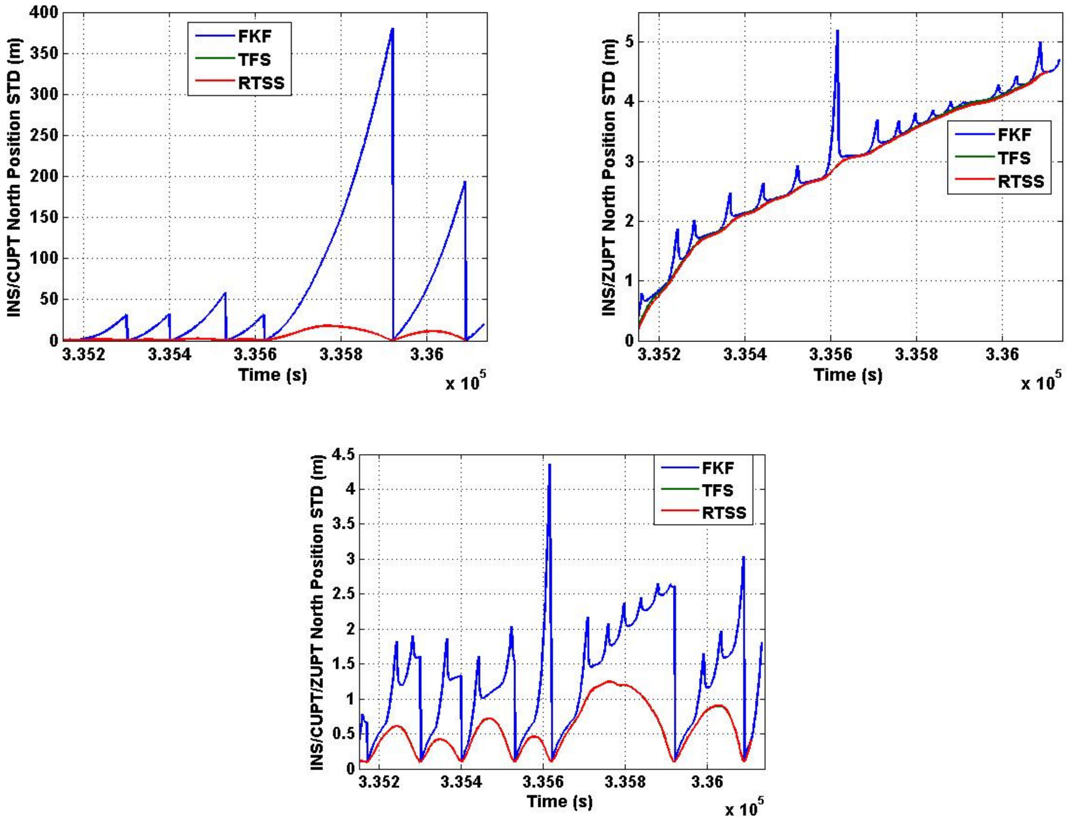

Figure 6.8 North Position STDs Using Different Integration Strategies

Roughly speaking, the position states in INS-based integration systems are not driven by random noises (Refer to the Q matrix in Section 2.3.4). As discussed in Section 3.4.1, only those states which are controllable by the system driving noise are smoothable in linear systems. However, the results shown in the previous Chapters proved that smoothers provide the position a superior estimation over filtering. This could probably be explained by the fact that the measurements from either GPS solutions or CUPTs directly improve the observability of the position states, which in turn improve their smoothability. Note that, due to the nonlinearity nature, the comprehensive controllability and the observability knowledge in the INS-based integration systems has not yet been fully understood. Therefore, it could be reasonable that the position errors are smoothable as long as CUPTs are provided; conversely, this performance can hardly be achieved by ZUPT, which is a velocity-based aiding technique.

The attitude standard deviations under different integration strategies are illustrated in Figure 6.9. These plots indicate that the roll and pitch angles can accurately be estimated using each of the three implemented integration strategies. Compared to the results of the INS/CUPT scheme, the ZUPT aiding (in both INS/ZUPT and INS/CUPT/ZUPT schemes) provides tilt angles with high accuracy due to their tight coupling with horizontal velocities. Meanwhile, the implementation of optimal smoothing improves the tilt error estimation accuracy. On the other hand, the estimation of heading error is not as accurate as the tilt angles and its STD diverges with time. This is mainly because of its poor observability from the occasional coordinate updates and frequent velocity updates. Further, smoothing can hardly obtain enhancement of heading estimation over filtering despite the minor improvement provided by the INS/CUPT/ZUPT scheme. This once again implies that the smoothability of a system state is not only related to the driving noise controllability but also its observability from measurements.

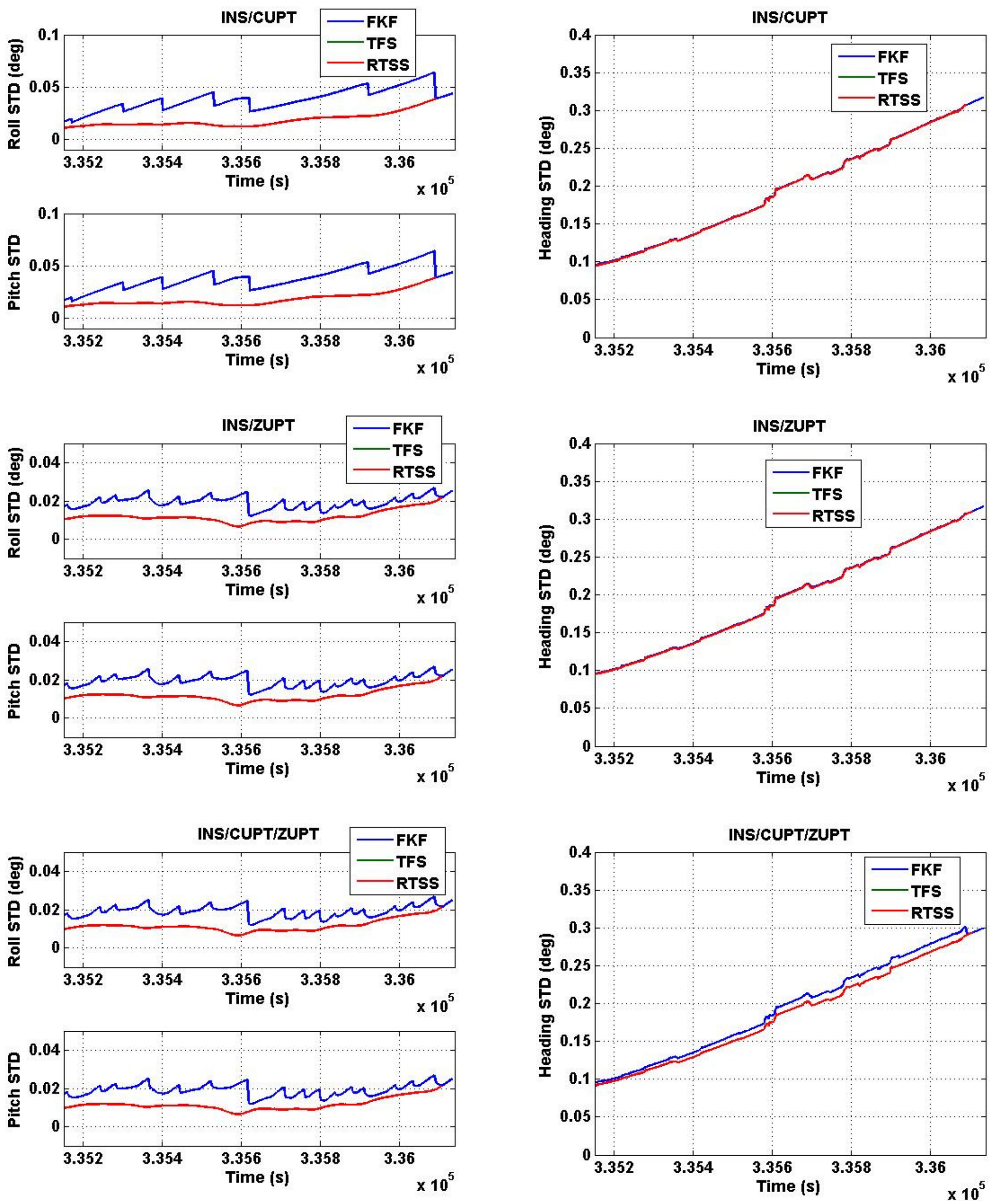

Figure 6.9 Attitude STDs Using Different Integration Strategies

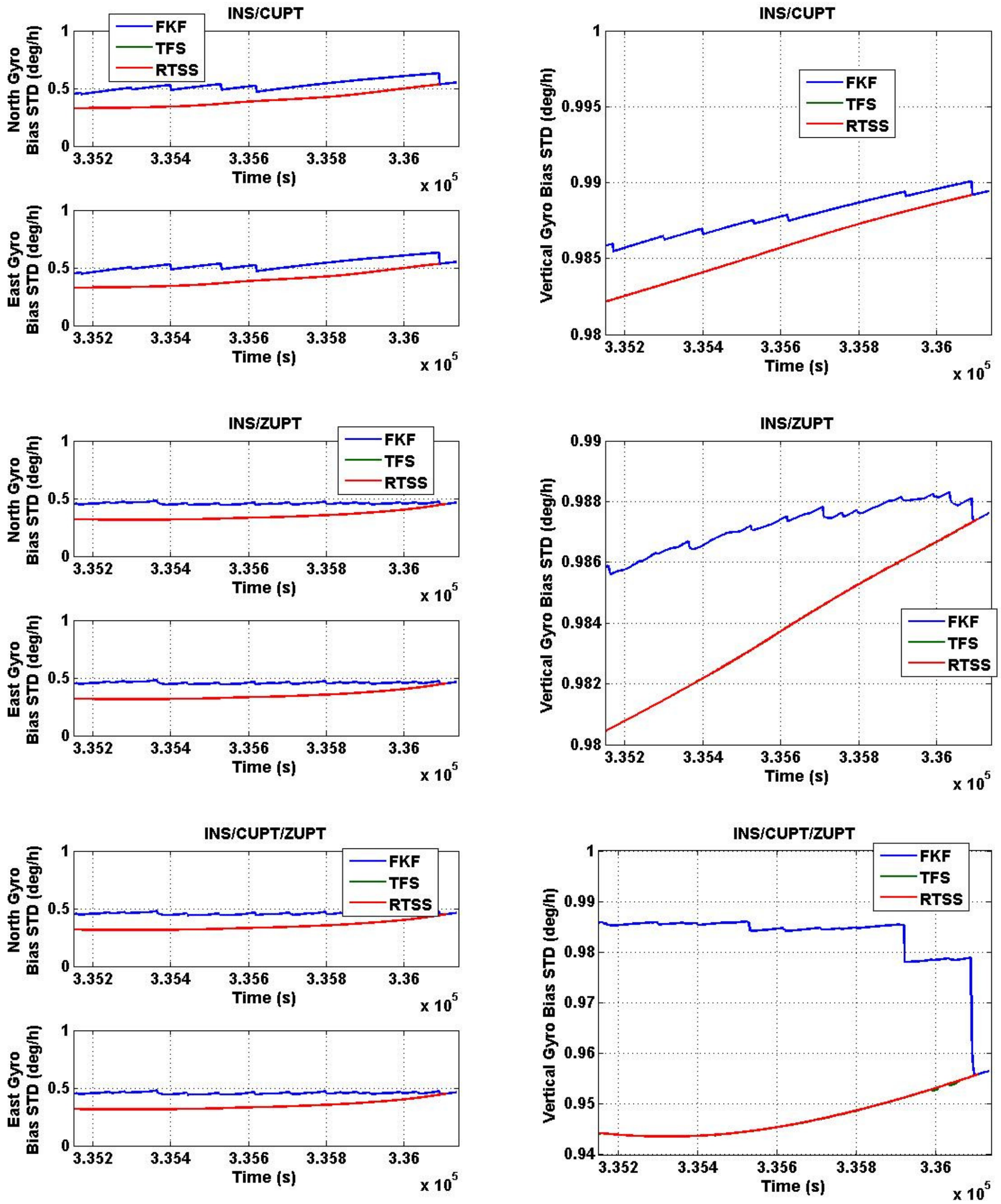

Figure 6.10 Gyro Bias STDs Using Different Integration Strategies

The gyro bias standard deviations are shown in Figure 6.10. The estimations of north and east gyro biases achieve high performance by ZUPT aiding and backward smoothing because of their strong and direct influence on tilt angles. Unfortunately, vertical gyro bias cannot be estimated accurately due to its coupling with azimuth, despite the little improvement of vertical gyro bias estimation provided by optimal smoothing (most notable when using INS/CUPT/ZUPT).

6.3 Description and Results of the Second Test

6.3.1 Vertical Test Description

The vertical test was conducted in an elevator of the ICT building at U of C. The transparent windows on the elevator make the laser ranging feasible in this test (Figure 6.11). The height of each of the building seven floors was measured in advance to provide aiding information as well as the reference to evaluate the estimation accuracy. A total station (see Figure 6.11) was set up at a long enough distance from the building to minimize foresight errors and a target was set up at the top of the north corner of the elevator window. This target was observed at each floor to provide the zenith angle measurement. Using trigonometric functions, the relative height value to the total station horizontal line was calculated for each floor (Isackson et al., 2008), see Figure 6.11. The corresponding vertical survey measurements and calculations are listed in Table 6.8.

The equipment cart was left stationary outside the ICT building for over 10 minutes before moving into the elevator. While ascending, the elevator was stopped at each floor for about 25-40 seconds for a ZUPT. After reaching the top, the cart followed a single descent to the bottom floor and was carried outside the building again. Another 10 minute static observations were recorded at the end of the survey (Isackson et al., 2008). The vertical test route, the height CUPT interpolation and GPS observations in the vertical direction are illustrated in Figure 6.12. The time interval and duration of the ZUPT corresponding to each floor are listed in Table 6.9.

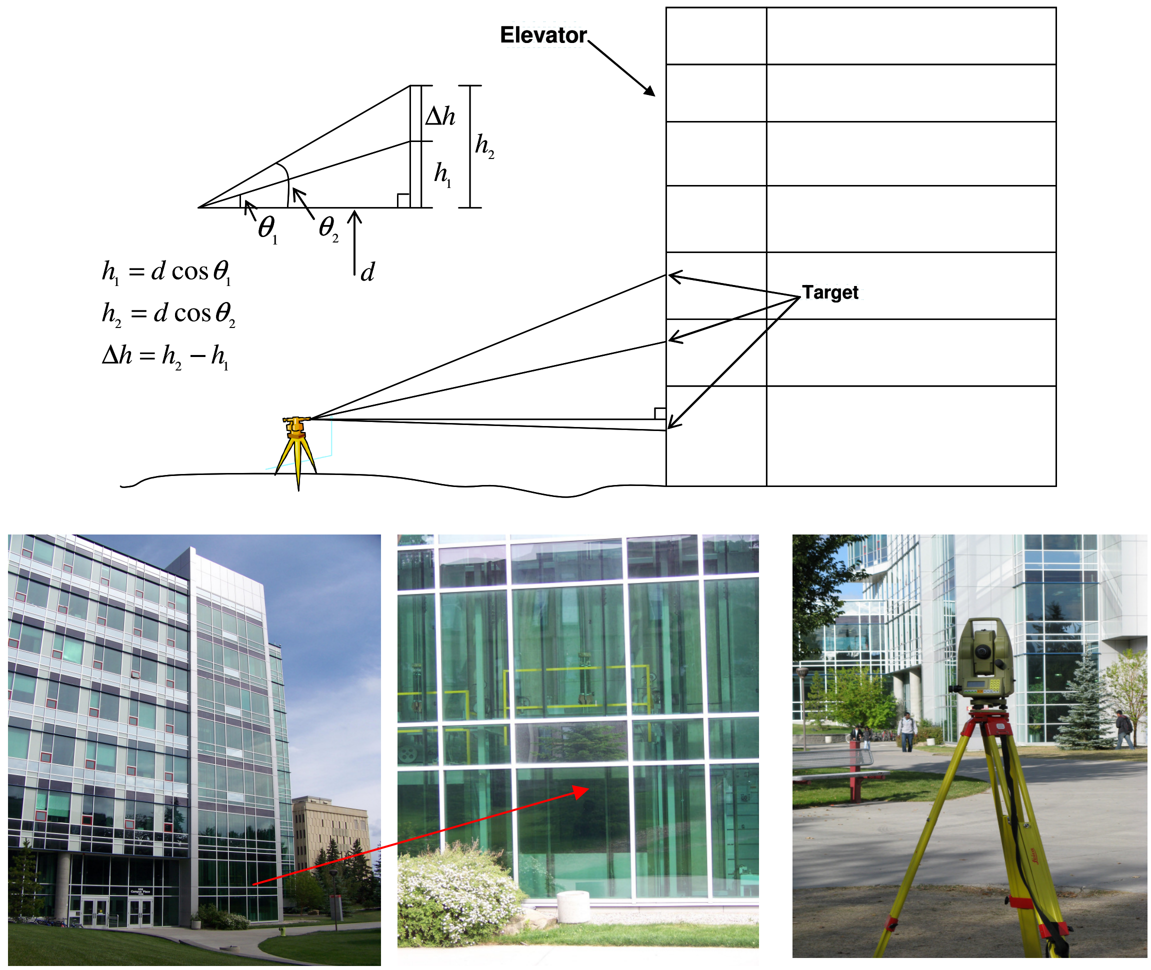

Figure 6.11 Vertical Height Survey Principle of the ICT Building at U of C (After Isackson et al., 2008)

Table 6.8 Vertical Survey Measurements and Calculations (After Isackson et al., 2008)

Floor #	Zenith Angle θ (degree)	Relative Height h (m)	Height Per Floor Δh (m)	Floor Height (m)
1	90.9892	-0.715	0.000	0.00
2	81.8842	5.6965	6.411	6.41
3	76.3083	9.7485	4.052	10.46
4	70.9178	13.8525	4.104	14.57
5	65.9486	17.879	4.027	18.59
6	61.2992	21.936	4.057	22.65
7	57.0303	25.951	4.015	26.67

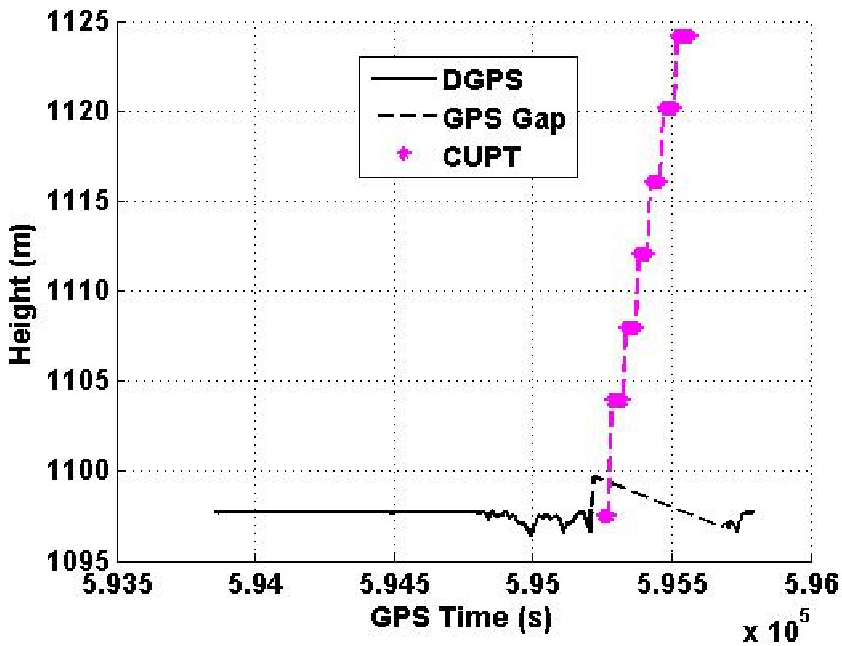

Figure 6.12 Vertical Testing Route (After Isackson et al., 2008)

Table 6.9 Vertical Testing ZUPTs (After Isackson et al., 2008)

Start Time (s)	Stop Time (s)	Duration (s)
1395.2	1419.6	24
1429.1	1472.0	43
1479.6	1518.6	39
1526.2	1561.4	35
1569.0	1608.9	40
1616.5	1657.0	41
1664.4	1717.6	53

6.3.2 Vertical Test Results

The straight vertical nature of the elevator ascending and descending route gains some special conditions for error propagation (Skaloud and Schwarz, 2000). The fixed heading maintains the balance between the accelerometer biases and the tilt errors after the levelling alignment. Moreover, the homogenous and benign acceleration profile along a straight trajectory moderates the cross correlations of position errors in the horizontal channels induced by the acceleration-dependent terms. This was analytically derived with respect to the azimuth misalignment and the gyro drift by Wong (1982). Finally, the hardly sensed translational displacement avoids the position errors induced by the azimuth uncertainty.

Considering the above factors, the remaining position errors by ZUPTs in a vertical surveying are mainly the results of accelerometer bias uncertainty, accelerometer scale factor, elevator vibration, cable torsion and so forth (Skaloud and Schwarz, 2000; Martell, 1991). Aiding from height coordinate updates and optimal smoothing will be implemented to restrict the uncompensated errors and to improve the estimation. Since the ascending time between neighbouring floors is normally 7-8 seconds (except for 10s to the 2nd floor), the accumulated vertical positioning error during that short time interval is roughly within decimetre level based on both the tactical-grade IMU (LN200) specification (See Appendix A) and the vertical surveying advantages. Therefore, the performance when using height CUPT aiding with INS will be similar to the case of INS/CUPT/ZUPT scheme. In this test, only the results of INS-Only, INS/ZUPT and

INS/CUPT/ZUPT will be analyzed and compared using filtering and smoothing algorithms.

INS-Only

The height estimation processed by INS-Only is shown in Figure 6.13. It indicates that the filtering results degrade downwards to an unacceptable level after entering the ICT building. Although the height error is restricted by smoothing, its accuracy cannot meet the requirement of indoor navigation.

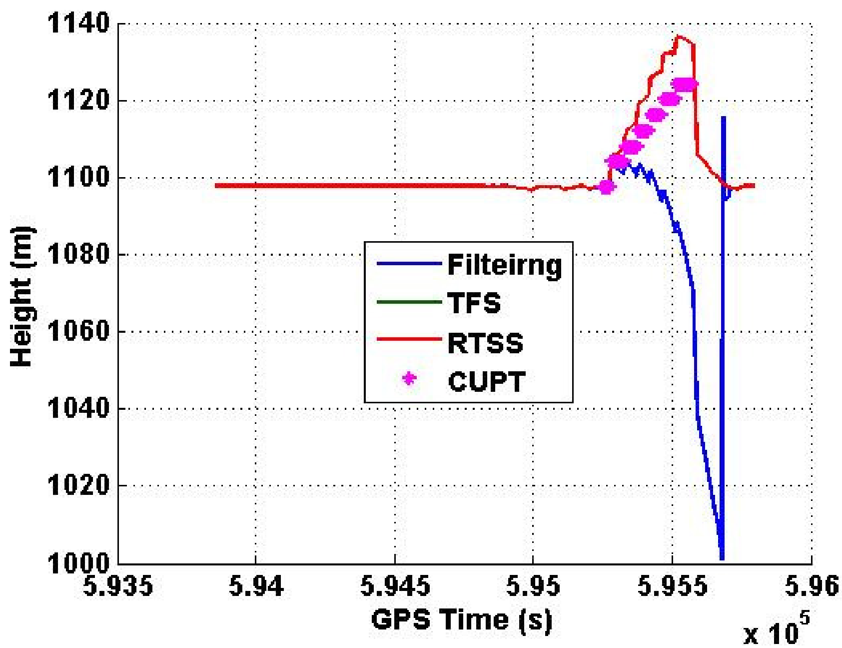

Figure 6.13 INS-Only Height Estimation

INS/ZUPT

The height estimations using INS/ZUPT integration are shown in Figure 6.14 and listed in Table 6.10, respectively. Note that the height errors are the averaged vertical displacements between the estimations and the corresponding vertical surveyed measurements. It suggests that the ZUPT aiding effectively prevents the filtering height estimation from diverging. However, decimetre level bias exists at each floor and increases along the ascending direction. Different from the conclusion obtained in the horizontal test, optimal smoothing significantly improves the height estimation by 71.8% for TFS and 69.2% for RTSS. This is probably granted by the advantages of the fixed-heading vertical survey stated earlier.

INS/CUPT/ZUPT

The height estimation results of INS/CUPT/ZUPT are shown in Figure 6.15 and given in Table 6.11 respectively. The vertical positioning displacements between the estimation results and the corresponding reference coordinate at each floor will be calculated in terms of the time one sample before (OSB) the height CUPTs. The figure shows that the vertical biases between filtering results and floor height measurements are constrained to centimetre level with the aiding from CUPTs. Furthermore, the filtering estimates are efficiently improved by backward smoothing. The enhancement level is 61.8% for both smoothers according to the OSB-CUPT height errors.

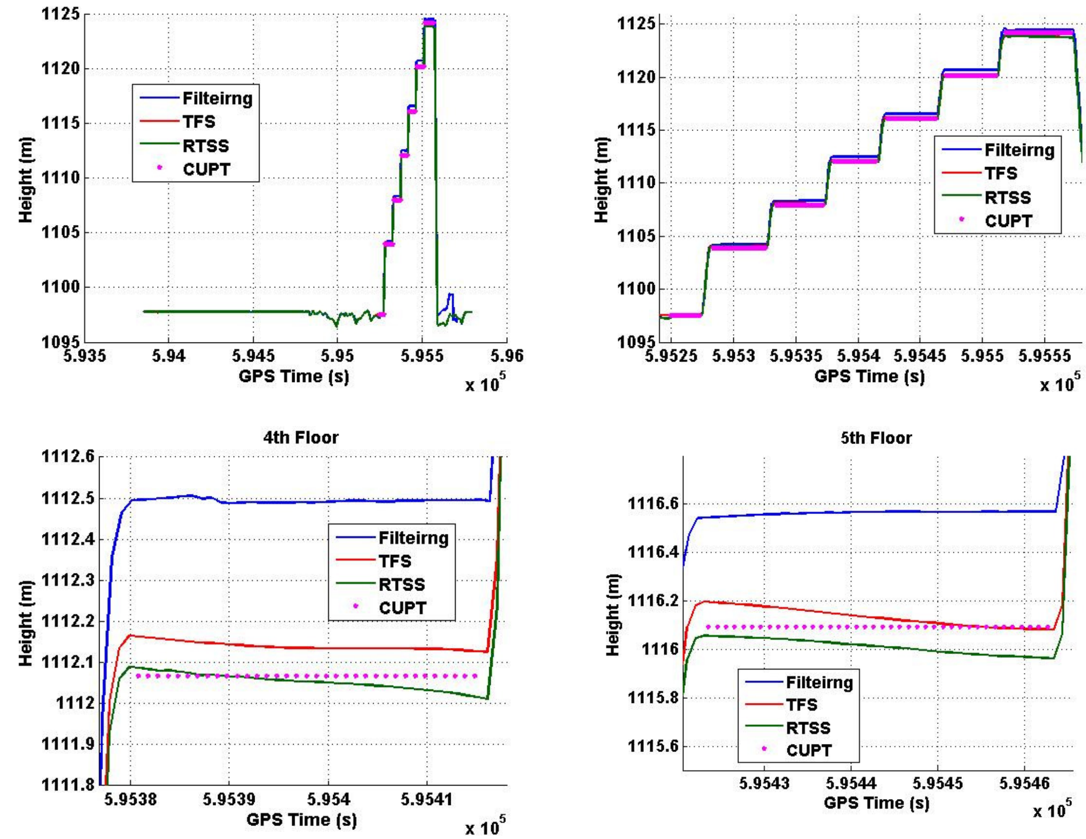

Figure 6.14 INS/ZUPT Height Estimation

Table 6.10 INS/ZUPT Height Errors at Each Floor

Floor	Height Error(m)		
	FKF	**TFS**	**RTSS**
#1	0.1001	0.0233	0.0838
#2	0.3206	0.1174	0.1588
#3	0.3726	0.0325	0.1148
#4	0.4268	-0.0119	0.0737
#5	0.4697	-0.0822	0.0401
#6	0.5472	-0.0963	-0.0410
#7	0.3026	-0.3507	-0.2688
Abs Mean	0.3628	0.1020	0.1116

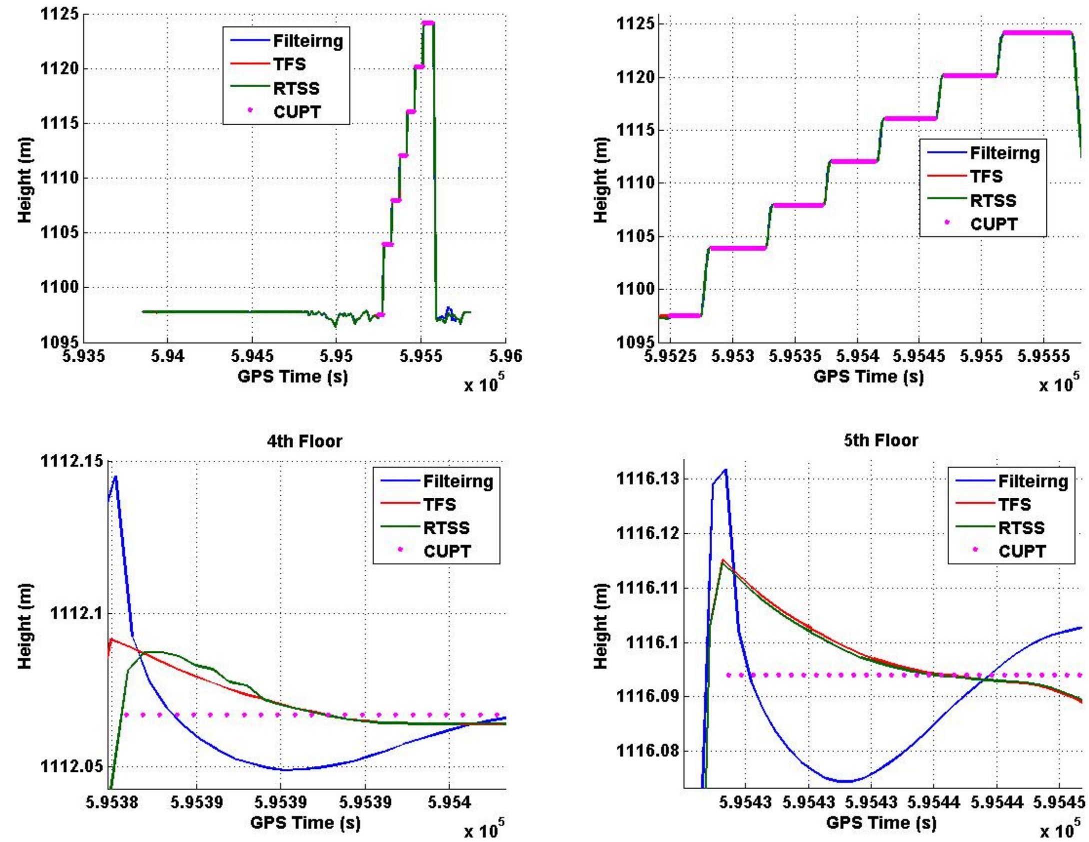

Figure 6.15 INS/CUPT/ZUPT Height Estimation

Table 6.11 INS/CUPT/ZUPT Height Errors at Each Floor

Floor	OSB-CUPT Height Error(m)		
	FKF	TFS	RTSS
#1	-0.2811	0.0075	0.0075
#2	0.1105	0.0327	0.0327
#3	0.0593	0.0112	0.0112
#4	0.0648	-0.0042	-0.0042
#5	0.0398	0.0089	0.0089
#6	0.0754	0.0110	0.0109
#7	-0.0963	-0.2027	-0.2027
Abs Mean	0.1039	0.0397	0.0397

The results demonstrate that the advantages of the vertical straightness nature and the low acceleration profile substantially suppress the height error accumulation. Moreover, the aiding from ZUPT and CUPT at each floor was successfully applied in this inertial survey with a tactical-grade IMU. However, rigorous vertical path or frequent ZUPT/CUPT might not be available in certain surveying environments like underground mining or high-rise building (Martell, 1991; Skaloud and Schwarz, 2000). Although the height accuracy in the presented test can hardly be achieved under these conditions, the integration strategies and the smoothing methodologies introduced in this Chapter provided their suitability and potentials in vertical positioning surveying applications.

Chapter Seven: CONCLUSIONS AND RECOMMENDATIONS

7.1 Summary

The main objective of this thesis was to evaluate the performance of filtering and optimal smoothing methodologies in different INS-based integrated system applications using different strategies, update navigation information and auxiliary sensors. The background of the inertial navigation concepts and the estimation/filtering/smoothing techniques were introduced and discussed in Chapters 2 and 3. The performance evaluations of Kalman Filter (KF) and optimal smoothing algorithms were presented in the Chapters 4, 5 and 6 for the following INS-based applications: Land-Vehicle Navigation (LVN), pipeline surveys, and horizontal/vertical building surveys, respectively.

For the work carried out herein, the major contributions of the thesis can be summarized as follows:

- Development and implementation of Kalman Filter (KF) algorithms and the corresponding RTSS schemes for INS/GPS, INS/ODOM/CUPT, and INS/ZUPT/CUPT integrated systems, respectively.
- Derivation, development and implementation of the Two Filter Smoother (TFS) algorithms for different INS-based applications including LVN, pipeline surveys, and horizontal/vertical building surveys using several integration strategies: INS/GPS, INS/ODOM/CUPT, and INS/ZUPT/CUPT systems, respectively.

- Performance evaluation and demonstration of the navigation estimation accuracy improvement using the developed smoothing techniques over the corresponding filtering algorithms for all INS-based applications and integration strategies mentioned above.
- Detailed analyses and comprehensive considerations for the smoothability, storage requirement, and measurement update gap filling while applying smoothing algorithms.
- Augmentation of the MMSS Research Group software: Aided Inertial Navigation System (AINS™) Toolbox, with the newly developed TFS and horizontal/vertical CUPT aiding modules.

7.2 Conclusions

For the results obtained throughout the thesis, the corresponding analyses lead to the following conclusions in terms of the used INS-based applications:

<u>A. Land-Vehicle Navigation (LVN)</u>

1. A tactical-grade IMU and a MEMS IMU were used in the INS/GPS field tests with several periods of GPS signal outages. For each IMU, the results showed that both the TFS and RTSS substantially improved the position estimation accuracy during these GPS outages. For the 60s outages for example, both smoothers improved the 3-D position errors by more than 95% in the case of each IMU.

2. The estimation efficiency and effectiveness of the developed TFS were comparable to the commonly used RTSS.
3. The efficiency of both smoothers is upgrading with the increasing length of GPS outages. The improvement levels in the first test (using the tactical-grade IMU) were 56.4%, 89.8%, 95.4% and 96.6% for 10s, 30s, 60s and 90s GPS outages, respectively. The corresponding improvement levels in the second test (using the MEMS IMU) were 34.6%, 86.8%, 95.7% and 96.4% respectively.

B. Pipeline Surveys

1. Odometer-derived velocities and non-holonomic constraints were used as auxiliary updates for the INS during navigation between control points. It was shown that those updates kept the filtering trajectory straight and effectively prevented the stand-alone INS error accumulation from growing rapidly with time. Then, using Coordinate Updates (CUPTs) as position updates when the INS passed by the fixed control points, the divergent position errors were effectively restricted.
2. The positioning errors obtained by filtering in either forward or backward directions were substantially reduced by the developed smoothing algorithms. The improvement level of TFS and RTSS was above 90.0% in terms of the 3-D OSB position errors; the corresponding improvement level was above 42% in terms of the 3-D OSA position errors.
3. The height errors are greater than those in horizontal directions, even if they are restricted by the CUPTs and further smoothed by the TFS or RTSS algorithms. It

was probably the consequence of the longer lever-arms in the vertical direction between the above ground markers and the passing PIG inside the underground pipeline. On the other hand, the sudden jumps, speed excursions and continuous trembling observed in the up velocity could also increase the height uncertainty and jeopardize its estimation accuracy.

C. Horizontal Building Surveys

1. The stand-alone INS results cannot meet the indoor navigation requirements.
2. Frequent ZUPTs help to control the horizontal drift of the filtering estimation within ten-meter level throughout the entire surveying process; however, metre-level translational displacements exist between the estimated trajectories and the control points.
3. Consequently, applying optimal smoothing algorithms using ZUPTs only did not provide significant improvement over filtering due to the lack of system controllability and observability.
4. INS/CUPT/ZUPT integration strategy benefits from the virtues of both the two aiding sources and achieves a superior performance compared to the other two integration schemes (i.e. INS/CUPT and INS/ZUPT). The results showed that the smoothing improved the filtering results by 66.4% in case of the TFS and by 55.7% in case of the RTSS, respectively.
5. The roll and pitch angles can accurately be estimated under each of the integration strategies. ZUPT aiding provided tilt angles high accuracy due to their tight coupling with horizontal velocities. On the other hand, the

estimation of heading error is not as accurate as the tilt angles because of its poor observability from occasional coordinate updates and frequent velocity updates. Meanwhile, the implementation of optimal smoothing improved the tilt error estimation accuracy but could hardly obtain notable enhancement of heading estimation over filtering.

D. Vertical Building Surveys

1. For height estimation in the elevator of multi-floor building using an INS-based system, the straight vertical nature of the elevator movement provides several special advantages to constrain the accumulation of systematic errors.
2. ZUPTs aiding effectively controlled the filtering height drift, but decimetre level bias existed at each floor and increased along the ascending direction. By the virtue of the fixed heading along the vertical direction, optimal smoothing significantly improved the height estimation by 71.8% using the TFS algorithm and by 69.2% using RTSS.
3. The filtering vertical errors were reduced to centimetre level under INS/CUPT/ZUPT integration strategy. Moreover, the filtering estimates were efficiently improved by both of the TFS and RTSS algorithms with enhancement levels of more than 61%.
4. The integration strategies and smoothing methodologies proposed in this application have promising potentials in other vertical positioning surveying applications.

7.3 Recommendations for Future Work

1. In the proposed TFS structure, the implementation of BKF without a backward INS mechanization relies on the stored FKF results. Conversely, a completely independent BKF is another choice for TFS, in which the backward INS mechanization is implemented to provide the INS solutions for both the backward nominal trajectory and the backward measurement updates.
2. The Adaptive Kalman Filter (AKF) aims to attain the optimal parameters in the process and measurement noise matrices. This objective has the potential to be fulfilled and researched using smoothing methodologies. The criterion to obtain the accurate a priori information by observing the smoothing results is recommended as a topic to be investigated.
3. The development and implementation of the RTSS and TFS in tightly-coupled and deeply-coupled INS/GPS integrated systems should be considered in future work.
4. Measurement-While-Drilling (MWD) and Wellbore-Mapping (WBM), for both vertical and horizontal boreholes, are potential navigation fields for INS and aiding sensors. Due to the operation environment, GPS is completely unavailable. With the emerging technology of MEMS inertial sensors, and other small-size aiding sensors, the design and implementation of the RTSS and TFS for these applications are recommended.

APPENDIX A

Summary of Litton LN-200 IMU Specifications (Source from www.littongcs.com)

Physical Characteristics:

- Weight: 1.54 pounds (700 grams)
- Size: 3.5 inches (8.9cm) diameter by 3.35 inches (8.5cm high)
- Power: 10 watts steady-state (nominal)
- Cooling: Conduction to mounting plate
- Mounting: 4 Mounting bolts - M4
- Activation Time: 0.8 sec (5 sec to full accuracy)

Performance-Gyroscope:

- Gyro Bias Repeatability: 1 to 10 $^{\circ}/hour$ (1 sigma)
- Random Walk: 0.04 to 0.1 $^{\circ}/\sqrt{hour}$ Power Spectral Density: (PSD) level
- Scale Factor Stability: 100 PPM (1sigma)
- Bias Variation: 0.35 $^{\circ}/hour$ (1 sigma) with 100 sec correlation time
- Non-orthogonality: 20 arcsec (1 sigma)
- Bandwith: >500 Hz

Performance-Accelerometer:

- Bias Repeatability: 200 micro-g to 1 milli-g (1 sigma)
- Scale Factor Stability: 300 PPM (1 sigma)
- Vibration Sensitivity: 50 micro-g/g^2 (1 sigma)
- Bias Variation: 50 micro-g (1 sigma) with 60 sec correlation time
- Non-orthogonality: 20 arcsec (1 sigma)
- White Noise: 50 micro-g/$\sqrt{Hz}$ PSD Level
- Bandwidth: 100 Hz

Operation-Range:

- Angular rate: ±1000 °/sec
- Angular Acceleration: ±100,000 °/sec/sec
- Acceleration: ±40 g
- Velocity Quantization: 0.00169 fps
- Angular Attitude: Unlimited
- Reliability (predicted): 32,995 hours MTBF

APPENDIX B

B.1 Figures in Section 4.3.3 (2nd dataset)

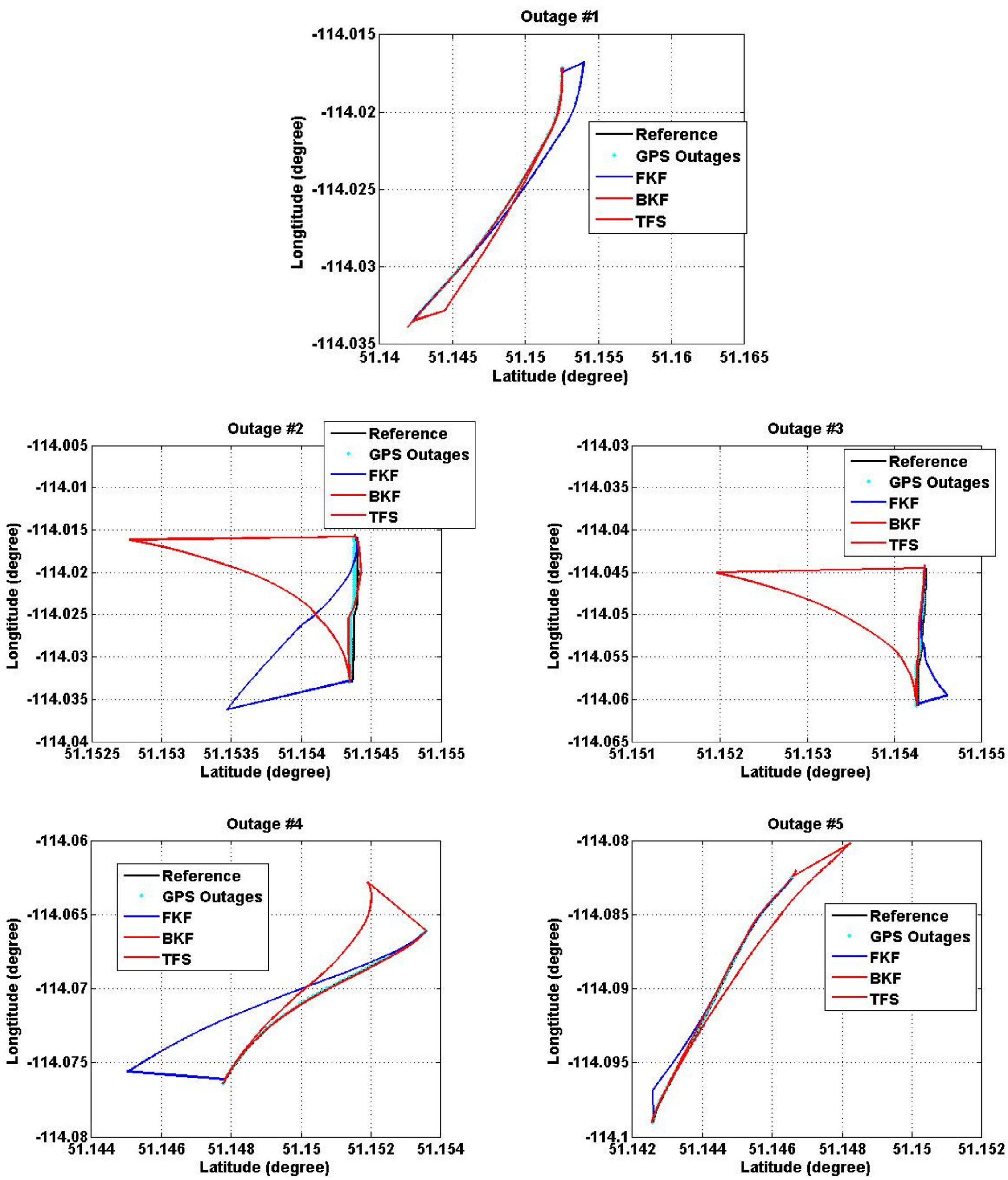

Figure B.1 Trajectories of FKF, BKF, and TFS in the 2nd Test

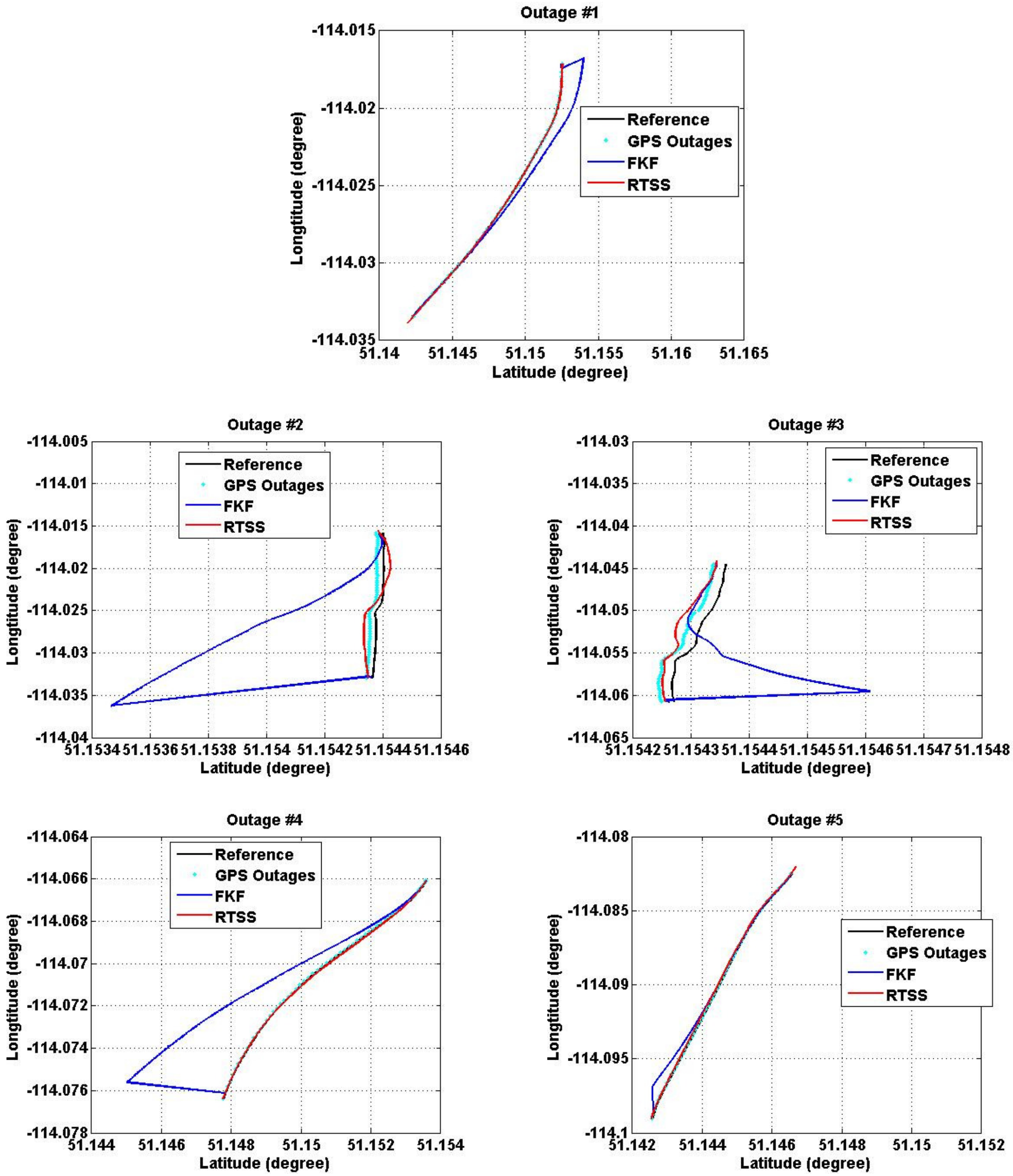

Figure B.2 Trajectories of FKF and RTSS in the 2nd Test

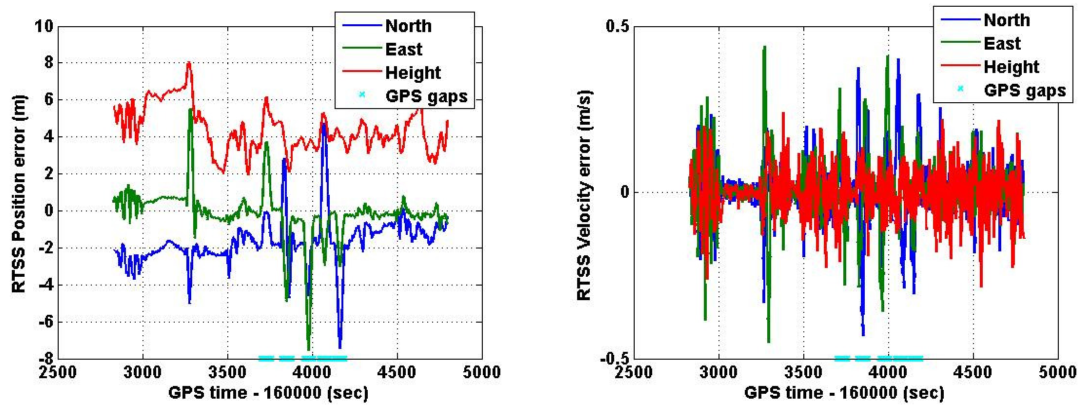

Figure B.3 MEMS RTSS Position and Velocity Errors

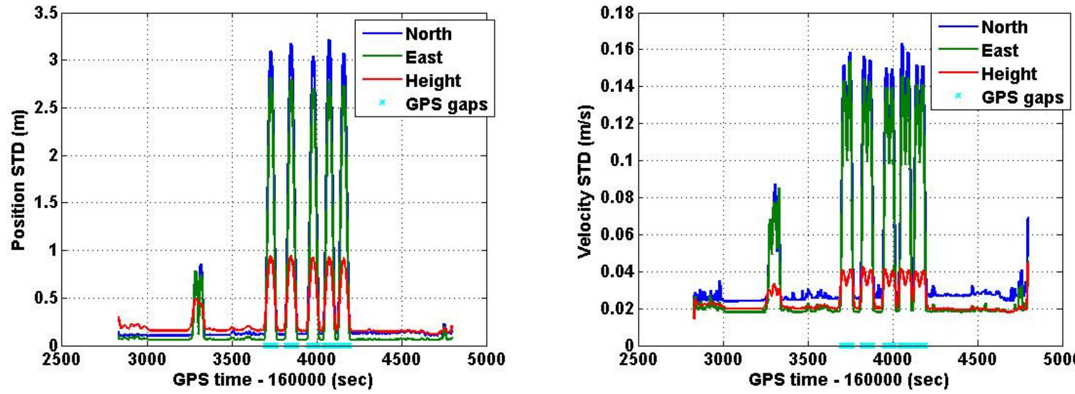

Figure B.4 MEMS RTSS Position and Velocity Error STDs

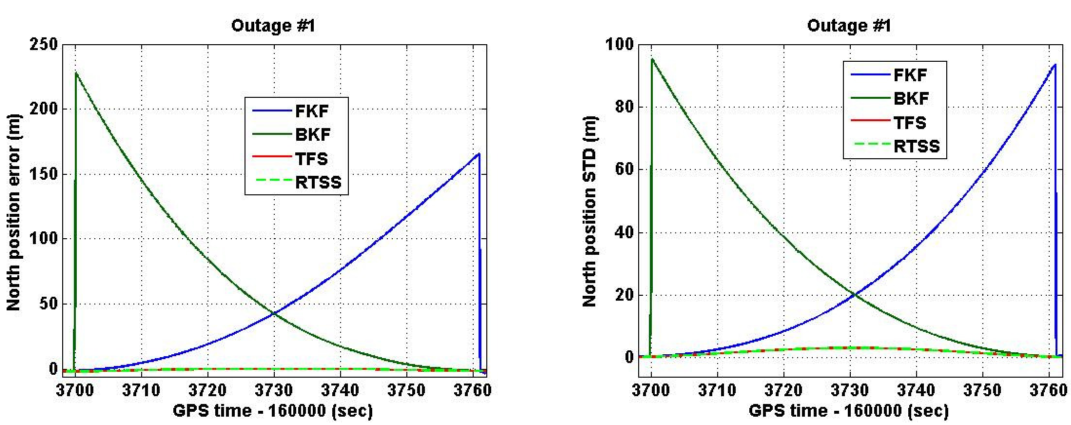

Figure B.5 MEMS North Position Error and STD Comparison in the 1st 60s outage

B.2 Figures in Section 4.3.4 (2^{nd} dataset)

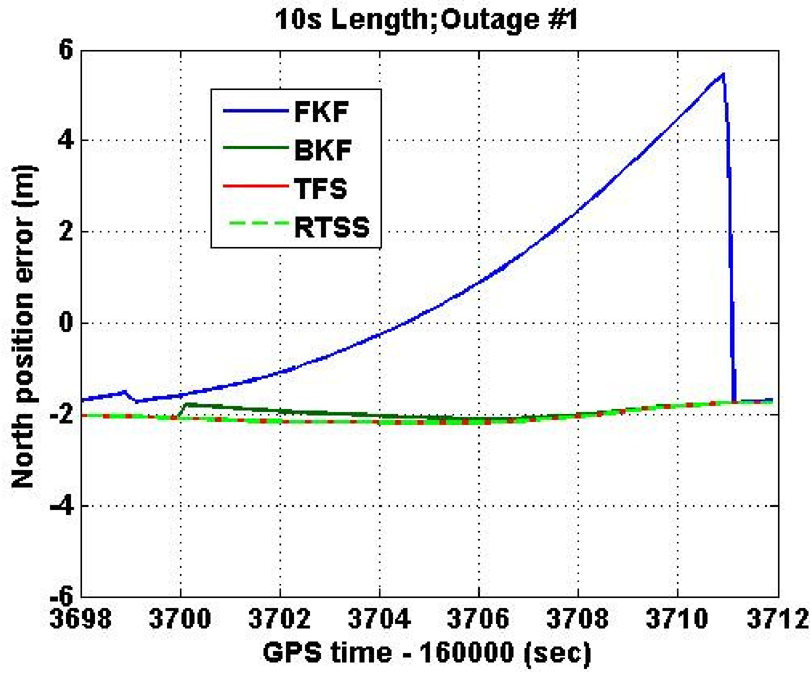

Figure B.6 MEMS North Position Errors Comparison with 10s outage length

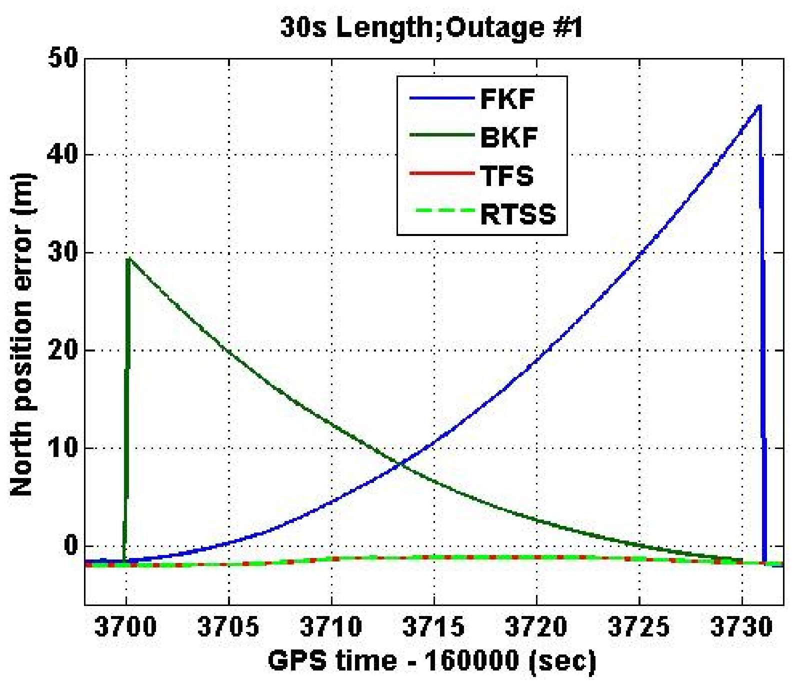

Figure B.7 MEMS North Position Errors Comparison with 30s outage length

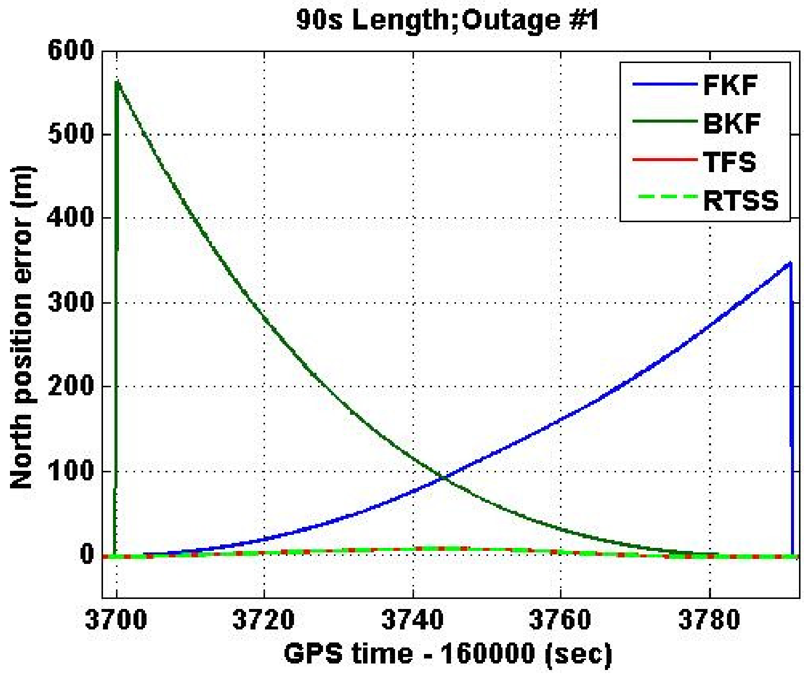

Figure B.8 MEMS North Position Errors Comparison with 90s outage length

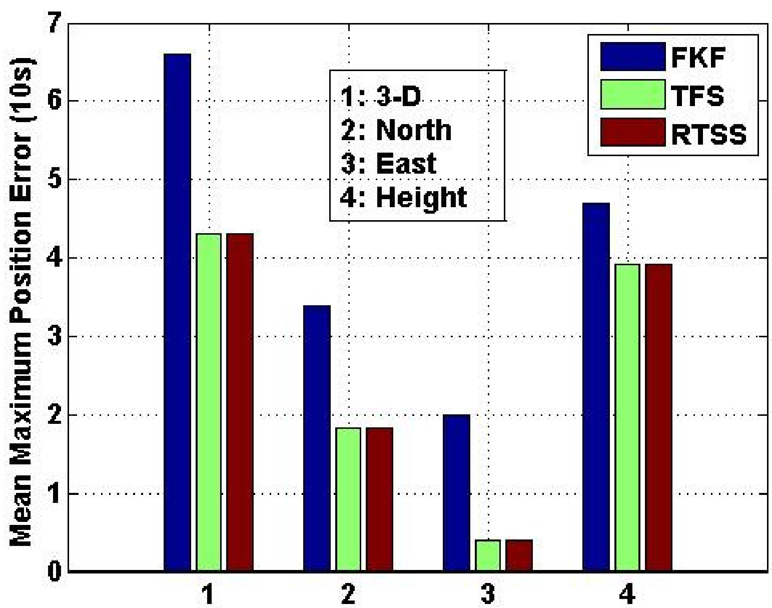

Figure B.9 Mean values of Maximum Position Errors across five 10s outages

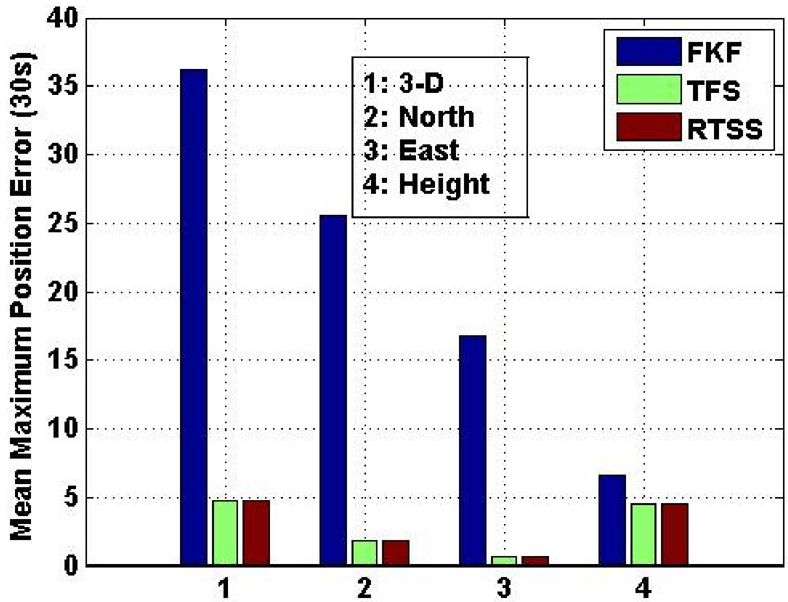

Figure B.10 Mean values of Maximum Position Errors across five 30s outages

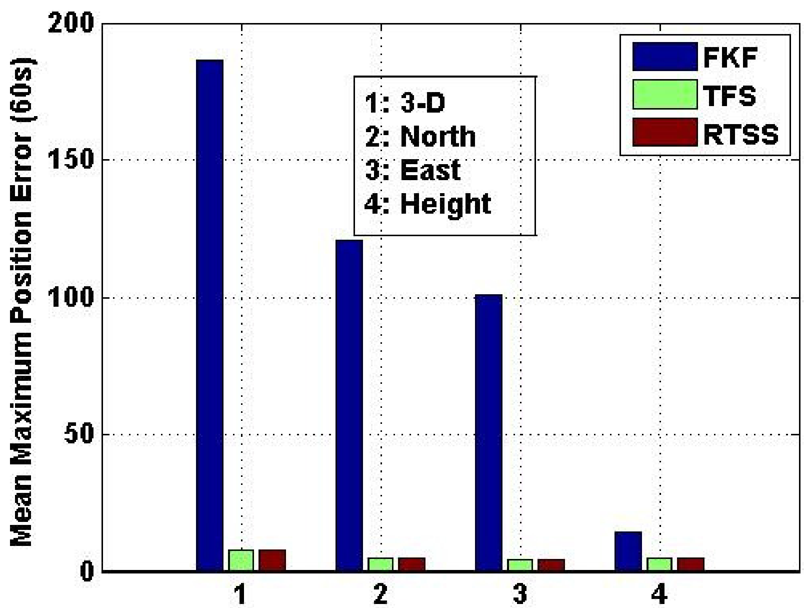

Figure B.11 Mean values of Maximum Position Errors across five 60s outages

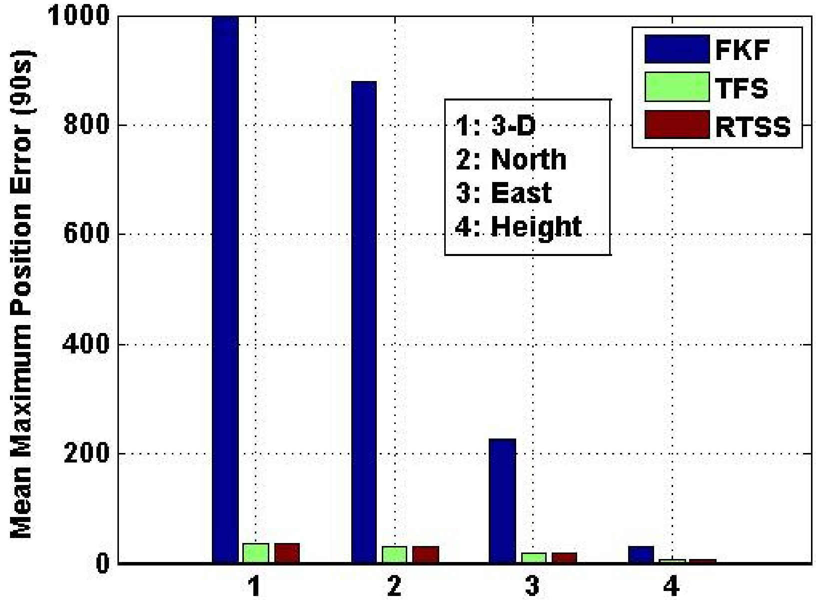

Figure B.12 Mean values of Maximum Position Errors across five 90s outages

References

Abdel-Hamid, W. (2005), "Accuracy Enhancement of Integrated MEMS-IMU/GPS Systems for Land Vehicular Navigation Applications", PhD thesis, UCGE Reports Number 20207, The University of Calgary, Calgary, Alberta, Canada.

Acharya, T. and Ray, A.K. (2005), "Image Processing: Principles and Applications", John Wiley & Sons.

Allan, G. and Hawes, J. (2005), "Scale Assessment Pigging of the Total Dunbar 16 Multi-Phase Pipeline", OPT Conference and Exhibition, Amsterdam, Holland.

Bar-Itzhack, I.Y. and Porat, B. (1980), "Azimuth Observability Enhancement during Inertial Navigation System In-Flight Alignment", Journal of Guidance, Control and Dynamics, Vol.3, NO.4, pp.337-343.

Bar-Itzhack, I.Y. and Berman, N. (1988), "Control Theoretic Approach to Inertial Navigation Systems", Journal of Guidance, Control and Dynamics, Vol.11, NO.3, pp.237-245.

Bierman, G.J. (1973), "Fixed Interval Smoothing with Discrete Measurements", International Journal of Control, Vol. 18, NO.1, pp.65-75.

Bortz, J.E. (1971), "A New Mathematical Formulation for Strapdown Inertial Navigation", IEEE Transactions on Aerospace and Electronic Systems, AES-7 (1):61-66.

Britting, K.R. (1971), "Inertial Navigation Systems Analysis", John Wiley & Sons, Inc.

Brown, R.G. and Hwang, P.Y.C. (1997), "Introduction to Random Signals and Applied Kalman Filtering", John Wiley & Sons Inc.

Bryson, A.E. and Frazier, M. (1962), "Smoothing for Linear and Nonlinear Dynamic Systems", Tech.Rep.TDR-63-119, Aeronautical System Division, Wright-Patterson Air Force Base, Ohio.

Crassidis, J.L. and Junkins, J.L. (2004), "Optimal Estimation of Dynamic Systems", Chapman & Hall/CRC.

El-Gizawy, M. L. (2009), "Continuous Measurement-While-Drilling Surveying System Utilizing MEMS Inertial Sensors", PhD thesis, UCGE Report 20284, The University of Calgary, Calgary, Alberta, Canada.

El-Sheimy, N. (2007), "Inertial Techniques and INS/GPS Integration", ENGO 623 Lecture Notes, Department of Geomatics Engineering, the University of Calgary, Canada.

Farrell, J.A. and Barth, M. (1998), "The Global Positioning System and Inertial Navigation", McGraw-Hill.

Fraser, D.C. (1967), "A New Technique for the Optimal Smoothing of Data", Ph.D. Dissertation, MIT, Cambridge, Massachusetts.

Fraser, D.C. and Potter, J.E. (1969), "The Optimum Linear Smoother as a Combination of Two Optimum Linear Filters", pp. 387-390, IEEE Transactions on Automatic Control.

Gao, Y. (2007), "Advanced Estimation Methods and Analysis", ENGO 629 Lecture Notes, Department of Geomatics Engineering, the University of Calgary, Canada.

Gelb, A. (1974), "Applied Optimal Estimation", The M.I.T. Press, Massachusetts Institute of Technology, Cambridge, Massachusetts, USA.

Godha, S. (2006), "Performance Evaluation of Low Cost MEMS-Based IMU Integrated with GPS for Land Vehicle Navigation Application", MSc thesis, UCGE Reports Number 20239, The University of Calgary, Calgary, Alberta, Canada.

Godha, S., Lachapelle, G. and Cannon M.E. (2006), "Integrated GPS/INS System for Pedestrian Navigation in a Signal Degraded Environment", ION GNSS 2006, Fort Worth TX, USA.

Goodall, C.L. (2009), "Improving Usability of Low-Cost INS/GPS Navigation Systems Using Intelligent Techniques", PhD thesis, UCGE Reports Number 20276, The University of Calgary, Calgary, Alberta, Canada.

Golub, G.H. and Van Loan (1996), C.F., "Matrix Computations", The Johns Hopkins University Press, Baltimore, MD.

Grewal, M.S. and Andrews, A.P. (2001), "Kalman Filtering: Theory and Practice.", Prentice-Hall, Inc.

Grejner-Brzezinska, D.A., Toth, C.K. and Yi, Y. (2001), "Bridging GPS Gaps in Urban Canynos: Can ZUPT Really Help?", Proceeding of ION GPS, Salt Lake City, UT, US.

Hanna, P.L. (1990), "Strapdown Inertial Systems for Pipeline Navigation", IEEE Colloquium on Inertial Navigation Sensor Development, London, UK.

Hou, H. (2004), "Modeling Inertial Sensor Errors Using Allan Variance", MSc thesis UCGE Reports Number 20201, The University of Calgary, Calgary, Alberta, Canada.

Huddle, J.R. (1998), "Trends in Inertial Systems Technology for High Accuracy AUV Navigation", Proceeding of Autonomous Underwater Vehicle Workshops at Draper Laboratory, Cambridge, Maine.

Isackson, I., Clipperton, B., Cairns, L. and Karbovnyk, P. (2008), "GPS/INS Integration for Indoor Navigation Appications", Final Report, ENGO 500 Geomatics Engineering Project, University of Calgary,

Jansson, P. (1998), "Precise Kinematic GPS Positioning with Kalman Filtering and Smoothing: Theory and Application", Doctoral Dissertation, Division of Geodesy Report NO. 1048, Department of Geodesy and Photogrammetry, Royal Institute of Technology, Stockholm, Sweden.

Jekeli, C. (2001), "Inertial Navigation Systems with Geodetic Applications", Walter de Gryter GmBH and Co.

Kaplan, E.D. and Hegarty, C.J. (2006), "Understanding GPS Principles and Applications", second edition, Artech house, Inc.

Kennedy, S. (2003), "Pipeline Pig Data", private communication, unpublished document, BJ Pipeline Inspection Services Calgary, Canada,

Kim, J. and Sukkarieh, S. (2002), "Flight Test Results of GPS/INS Navigation Loop for an Autonomous Unmanned Aerial Vehicle (UAV)", ION GPS 2002, Portland, OR, USA.

King, A.D. (1998), "Inertial Navigation-Forty Years of Evolution", V.13, N.3, pp. 140-149, GEC Review.

Liu, H., Nassar, S., and El-Sheimy, N. (2009), "Performance Evaluation of Different Optimal Smoothers for Land-Vehicle Navigation Using Integrated GPS/INS Systems", Proceeding of ENC-GNSS 2009, Naples, Italy.

MacGougan, G.D. (2003), "High Sensitivity GPS Performance Analysis in Degraded Signal Environments", MSc thesis, UCGE Reports Number 20175, The University of Calgary, Calgary, Alberta, Canada.

Martell, H.E. (1991), "Applications of Strapdown Inertial Systems in Curvature Detection Problems", MSc thesis, UCGE Reports Number 20043, The University of Calgary, Calgary, Alberta, Canada.

Maybeck, P.S. (1994), "Stochastic Optimal Linear Estimation and Control: V.2", Navtech Book & Software Store.

Mayne, D.Q. (1966), "A Solution to the Smoothing Problem for Linear Dynamic Systems", Automatica, Vol. 4, NO. 6, pp.73-92.

Meditch, J.S. (1969), "Stochastic Optimal Linear Estimation and Control", McGraw-Hill.

Nassar, S. (2003), "Improving the Inertial Navigation System (INS) Error Model for INS and INS/DGPS Applications", PhD thesis, UCGE Reports Number 20183, The University of Calgary, Calgary, Alberta, Canada.

Nassar, S., Noureldin, A. and El-Sheimy, N. (2004), "Improving Positioning Accuracy during Kinematic DGPS Outage Periods Using SINS/DGPS Integration and SINS Data De-noising", Survey Review, UK, V.37, N.292, pp. 426-438, April.

Nassar, S., Shin, E., Niu, X. and El-Sheimy, N. (2005), "Accurate INS/GPS Positioning with Different Inertial Systems Using Various Algorithms for Bridging GPS Outages", Proceeding of International Technical Meeting of ION-GNSS, Long Beach, CA, U.S.

Nassar, S., Syed, Z., Niu, X. and El-Sheimy, N. (2006), "Improving MEMS IMU/GPS Systems for Accurate Land-Based Navigation Applications", The Institute of Navigation National Technical Meeting (ION NTM 2006), Monterey, California, USA, pp. 523-529, January 18-20.

Niu, X. and El-Sheimy, N. (2005), "The Development of Low-Cost MEMS-Based IMU for Land Vehicle Navigation Applications Using Auxiliary Velocity Updates in the Body Frame", ION GNSS 2005, Long Beach, CA, USA.

Niu, X., Yang, Y. and Hassan, T. (2006), "Lab Testing and Calibration of MEMS IMUs", Moblie Multi-Sensor Systems (MMSS) Research Group, Department of Geomatics Engineering, the University of Calgary, Canada.

Niu, X., Nassar, S., Syed, Z., Goodall, C. and El-Sheimy, N. (2006), "The Development of A MEMS-Based Inertial/GPS System for Land-Vehicle Navigation Applications", The Institute of Navigation Satellite Division Technical Meeting (ION GNSS 2006), Fort Worth, Texas, USA, pp. 1516-1525, September 26-29

Noureldin, Aboelmagd (2002), "New Measurement While Drilling Surveying Technique Utilizing Sets of Fiber Optic Rotation Sensors", PhD thesis, UCGE Reports, The University of Calgary, Calgary, Alberta, Canada.

O'Keefe, K. (2008), "Wireless Location", ENGO 585 Lecture Notes, Department of Geomatics Engineering, the University of Calgary, Canada.

Petovello, M.G., (2003), "Real-Time Integration of a Tactical-Grade IMU and GPS for High-Accuracy Positioning and Navigation", PhD thesis, UCGE Reports Number 20173, The University of Calgary, Calgary, Alberta, Canada.

Porter, T.R., Knickmeyer, E.H. and Wade, R.L. (1990), "Pipeline Geometry Pigging: Application of Strapdown INS", Position Location and Navigation Symposium, IEEE, Las Vegas, NV, USA.

Rauch, H.E., Tung, F. and Striebel, C.T. (1965), "Maximum Likelihood Estimates of Linear Dynamic Systems", AIAA Journal, V.3, N.8.

Savage, P.G. (2004), "Strapdown Analytics, Part 1", Strapdown Associates, Inc., Maple Plain, Minnesota.

Scherzinger, B.M. (1996), "Inertial Navigator Error Models for Large Heading Uncertainty", IEEE Position Location and Navigation Symposium, pp. 477-484.

Schwarz, K.P. and Wei, M. (1999), "INS/GPS Integration for Geodetic Applications", ENGO 623 Lecture Notes, Department of Geomatics Engineering, the University of Calgary, Canada.

Shin, E. (2001), "Accuracy Improvement of Low Cost INS/GPS for Land Applications", MSc thesis, UCGE Reports Number 20156, The University of Calgary, Calgary, Alberta, Canada.

Shin, E. (2005), "Estimation Techniques for Low-Cost Inertial Navigation", PhD thesis, UCGE Reports Number 20219, The University of Calgary, Calgary, Alberta, Canada.

Shin, E-H. and El-Sheimy, N. (2002), "Optimizing Smoothing Computation for Near Real-Time GPS Measurement Gap Filling in INS/GPS Systems", Proceeding of ION GPS 2002, Portland, OR, USA.

Shin, E. and El-Sheimy, N. (2005), "Backward Smoothing for Pipeline Surveying Applications", Proceeding of ION NTM, San Diego, CA, U.S.

Shin, E. and El-Sheimy, N. (2005), "Navigation Kalman Filter Design for Pipeline Pigging", Journal of Navigation, Vol.58, pp.283-295.

Singh, S. (2006), "Comparison of Assisted GPS and High Sensitivity GPS in Weak Signal Conditions", MSc thesis, UCGE Reports Number 20247, The University of Calgary, Calgary, Alberta, Canada.

Skaloud, J. and Schwarz, K.P. (2000), "Application of Inertial Technology to Underground Positioning: The Soudan Mine Shaft Survey", Zeitschrift für Vermessungswesen (ZfV), Vol 8: pp. 292-299.

Stevenson, K.M., Estates, P.V., and Berg, R.L. (1970), "Inertial Navigation System", U.S. Patent, N.O. 3509765.

Sukkarieh, S. (2000), “Low Cost, High Integrity, Aided Inertial Navigation Systems for Autonomous Land Vehicles”, Ph.D Thesis, Australian Centre for Field Robotics, Dept. of Mechanical and Mechatronic Engineering, The University of Sydney, Sydney, Australia.

Syed, Z.F. (2009), “Design and Implementation Issues of a Portable Navigation System”, PhD thesis, UCGE Reports Number 20288, The University of Calgary, Calgary, Alberta, Canada.

Titterton, D.H. and Weston, J.L. (2004), “Strapdown Inertial Navigation Technology”, second edition, The Institution of Electrical Engineers.

Watson, J.R. (2005), “High-Sensitivity GPS L1 Signal Analysis for Indoor Channel Modeling”, UCGE Reports Number 20215, The University of Calgary, Calgary, Alberta, Canada.

Weinred, A. and Bar-Itzhack, I.Y. (1978), “The Psi-Angle Error Equation in Strapdown Inertial Navigation Systems”, IEEE Aerospace and Electronic Systems, AES-14, NO.3., pp.539-542.

Wiener, N. (1949), “Extrapolation, Interpolation, and Smoothing of Stationary Time Series”, New York, John Wiley & Sons.

Wong, R.V.C. (1982), “A Kalman Filter-Smoother for an Inertial Survey System of Local Level Type”, MSc thesis, Department of Civil Engineering, The University of Calgary, Calgary, Alberta, Canada.

Yang, Y (2008), “Tightly Coupled MEMS INS/GPS Integration with INS Aided Receiver Tracking Loops”, PhD thesis, UCGE Reports Number 20270, The University of Calgary, Calgary, Alberta, Canada.

Yuksel, Y. (2008), “Pipeline Data Processing Report”, Mobile Multi-Sensor Systems (MMSS) Group, Department of Geomatics Engineering, University of Calgary, Unpublished Document.

Yu, J., Lee, J. G., Park, C. G and Han, H. S. (2005), “An Off-Line Navigation of A Geometry PIG Using A Modified Nonlinear Fixed-Interval Smoothing Filter”, pp. 1403-1411, Control Engineering Practice.